

7-187
2187612
TR 3162

3162

TR3162

**Complex Magnetic
Phenomena
in
Rare Earth Intermetallic
Compounds**



**Complexe Magnetische Verschijnselen
in
Intermetallische Zeldzame Aard Verbindingen**

Cover: *Impression of Mössbauer spectroscopy (red gamma rays), neutron scattering (green neutrons) and muon spin rotation (orange muons) performed on a hexagonal compound (RNi_5) containing egg shaped purple 4f electronic shells.*

Art by **Marc Brinkman**

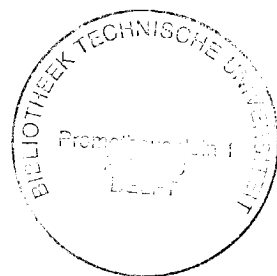


The research described in this thesis was performed in the Department of Radiation Physics of the Interfacultair Reactor Instituut, Delft University of Technology, Mekelweg 15, 2629 JB Delft, The Netherlands.

We gratefully acknowledge the financial support from the Netherlands Organisation for Scientific Research (NWO) and the European Commission under the Human Capital and Mobility Programme (HCM), Access to large-scale facilities.

Complex Magnetic Phenomena in Rare Earth Intermetallic Compounds

PROEFSCHRIFT



ter verkrijging van de graad van doctor
aan de Technische Universiteit Delft,
op gezag van de Rector Magnificus prof. ir. K. F. Wakker,
in het openbaar te verdedigen ten overstaan van een commissie,
door het College voor Promoties aangewezen,
op donderdag 18 juni 1998 te 10.30 uur
door

Anna Maria MULDER

technisch natuurkundig ingenieur (hbo)
geboren te Maasland

Dit proefschrift is goedgekeurd door de promotoren:

Prof. dr. K.H.J. Buschow

Prof. dr. H. Postma

Samenstelling promotiecommissie:

Rector Magnificus, voorzitter

Prof. dr. K.H.J. Buschow, Universiteit van Amsterdam, promotor

Prof. dr. H. Postma, Technische Universiteit Delft, promotor

Prof. dr. J.J.M. Franse, Universiteit van Amsterdam

Prof. dr. ir. F. Tuinstra, Technische Universiteit Delft

Dr. ir. A.M. van der Kraan, Technische Universiteit Delft

Dr. P. Dalmas de Réotier, CEA, Grenoble, France

Dr. P.C.M. Gubbens, Technische Universiteit Delft

Prof. dr. ir. C.W.E. van Eijk, Technische Universiteit Delft, reservelid

Dr. P.C.M. Gubbens heeft als begeleider in belangrijke mate aan het totstandkomen van dit proefschrift bijgedragen.

Published and distributed by:

Delft University Press

Mekelweg 4

2628 CD Delft

The Netherlands

Telephone: +31 15 2783254

Fax: +31 15 2781661

E-mail: dup@dup.tudelft.nl

Mulders, Anna Maria

ISBN 90-407-1696-x / CIP

NUGI: 812

Subject headings: rare earth magnetism/Mössbauer spectroscopy/muon spin rotation/
neutron scattering.

Copyright ©1998 by Annemieke Mulders.

All rights reserved. No part of the material protected by this copyright notice may be reproduced or utilized in any form or by any means, electronic or mechanical, including photocopying, recording or by any information storage and retrieval system, without permission from the publisher.

Printed in the Netherlands.

*.....to myself, I seem to have been only
like a boy playing on the sea-shore.....*

Isaac Newton

Contents

About this thesis	1
1 Rare earth intermetallics	3
1.1 Introduction	4
1.2 The magnetic moment of the rare earth atom	5
1.3 Magnetic interactions	7
1.4 Crystal field theory	9
1.5 About magnetic phase transitions	11
2 Experimental principles	13
2.1 Introduction	14
2.2 Mössbauer spectroscopy	14
2.2.1 Isomer shift	15
2.2.2 Quadrupole splitting	15
2.2.3 Magnetic hyperfine field	17
2.2.4 Nuclear transitions	18
2.3 μ^+ SR Spectroscopy	18
2.4 Neutron techniques	22
2.4.1 Neutron Depolarization	22
2.4.2 Inelastic Neutron Scattering	23
2.4.3 Neutron Diffraction	24
2.5 Macroscopic techniques	25
2.5.1 Magnetization	25
2.5.2 Specific heat	25
3 Magnetic nanodomains in TmFeAl	27
3.1 Introduction	28
3.2 Theoretical aspects	29
3.3 Experimental	30
3.4 Results	32
3.4.1 Mössbauer spectroscopy	32
TmFeAl	32
YFeAl, ErFeAl, DyFeAl and GdFeAl	36
3.4.2 Magnetization	37

3.4.3	Neutron Depolarization	39
3.4.4	Neutron Diffraction	41
3.5	Discussion	42
3.6	Conclusion	46
4	Two types of magnetism in the magnetic superconductor $\text{TmNi}_2\text{B}_2\text{C}$ related to the degree of carbon site occupancy	47
4.1	Introduction	48
4.2	Theoretical aspects	49
4.3	Experimental details	50
4.4	Results	50
4.4.1	$\text{TmNi}_2\text{B}_2\text{C}$, sample A	50
4.4.2	$\text{TmNi}_2\text{B}_2\text{C}$, sample B	53
4.5	Discussion	57
4.6	Conclusion	59
5	PrRu_2Si_2: a giant anisotropic induced magnet with a singlet crystal field ground state	61
5.1	Introduction	62
5.2	Experimental results	62
5.2.1	Specific heat	62
5.2.2	Single crystal magnetization	64
5.2.3	^{141}Pr Mössbauer spectroscopy	64
5.2.4	Muon spectroscopy	65
5.2.5	Neutron powder diffraction	66
5.2.6	Inelastic neutron scattering	68
5.3	Analysis of the experimental results	71
5.3.1	Hamiltonian	71
5.3.2	Crystal field determination	71
5.3.3	Analysis of the data in the molecular field approximation	73
5.3.4	Analysis of the magnetic properties in the random phase approximation	75
5.4	Discussion and conclusion	75
5.A	Eigenvalues and eigenstates of the CEF hamiltonian	77
6	Muon site and muon dynamics in GdNi_5	79
6.1	Introduction	80
6.2	The muon Knight shift	81
6.3	Experimental procedure	82
6.4	Results	85
6.4.1	Determination of the muon sites	85
6.4.2	Muon hopping from the $6m$ to the $3f$ site	93
6.4.3	Analysis of muon hopping	95
6.5	Discussion	97
6.5.1	Muon dynamics in GdNi_5	97

6.5.2	Interaction of the muon with its host	97
6.5.3	Comparison with other RNi_5	100
6.6	Conclusions	101
Bibliography		103
Summary		109
Samenvatting		111
Dankwoord & Thanks		113
Curriculum Vitae		115
List of Publications		115
Index		117

About this thesis

Rare earth intermetallics are of interest because they exhibit specific and unique magnetic properties. In modern technology some of them are used to manufacture excellent permanent magnets which are for example used in motors (to convert electric power into mechanical energy or vice versa) and other mechanical devices. The most important property for this application is their strong magnetic anisotropy, i.e. the magnetic moments of the rare earth atoms can show a strong preferential orientation in the material. In combination with the high magnetic ordering temperature of the transition metals (Fe, Co etc.) excellent magnets such as SmCo_5 and $\text{Nd}_2\text{Fe}_{14}\text{B}$ are realized which show a high magnetic remanence and coercive field.

LaNi_5 forms the basis for rechargeable batteries where it is applied as one of the electrodes. This compound absorbs large quantities of hydrogen and its hydrogen content is denser than liquid hydrogen itself. It is therefore also used as a hydrogen gas storage medium and replaces high pressure gas cylinders by powdered material. Basic properties of the rare earth ions (series from La to Lu in the periodic table) and the origin of their magnetic moments are discussed in chapter 1.

The characteristics of rare earth intermetallics are determined by the electronic structure of the individual constituents, the crystal structure and its symmetry. Large diversities in material properties are realized due to differences in electronic structure, such as superconductivity, antiferromagnetism, Kondo and heavy fermion behaviour. By element substitution the influence of the individual elements are studied and nowadays the complexities of the different types of compounds are reasonably well understood.

The research presented in this thesis deepens the knowledge and understanding of rare earth intermetallics. Results are obtained from four different compounds, TmFeAl , $\text{TmNi}_2\text{B}_2\text{C}$, PrRu_2Si_2 and GdNi_5 (chapter 3, 4, 5 and 6). Each of these compounds shows its own magnetic behaviour and peculiarities. Results obtained on TmFeAl show that this compound forms magnetic nanodomains, a property which has never been observed before. Results on $\text{TmNi}_2\text{B}_2\text{C}$ show the influence of carbon vacancies in this compound and an explanation is given for a puzzling discrepancy in Tm magnetic moment size reported in literature. Results on PrRu_2Si_2 explain the large magnetic anisotropy observed in this compound in terms of crystal field effects and dispersion of the lowest crystal field levels. Results

on GdNi_5 show novel muon dynamics which gives new insights in muon localization properties in intermetallics. The scientific relevance of these four intermetallics are discussed in the introduction of the individual chapters. The experimental techniques used to obtain these results, such as neutron scattering, muon and Mössbauer spectroscopy, are discussed in chapter 2.

★ ★ ★
★

Rare earth intermetallics

Abstract

The basic principles concerning rare earth magnetism are discussed such as the origin of the rare earth magnetic moment, the magnetic interaction between the atomic moments and crystal field theory.

1.1 Introduction

The rare earth (R) atoms are characterized by a partially filled electronic $4f$ shell. They form the series of atoms from La to Lu in the periodic table and following this series from the left to the right, each time an extra electron is added to the $4f$ shell. The $4f$ electronic shell is located inside the electron cloud of its host atom. This is illustrated in Fig. 1.1 where Hartree-Fock calculations are shown of some electronic shells of gadolinium [1]. When located in a solid, only the

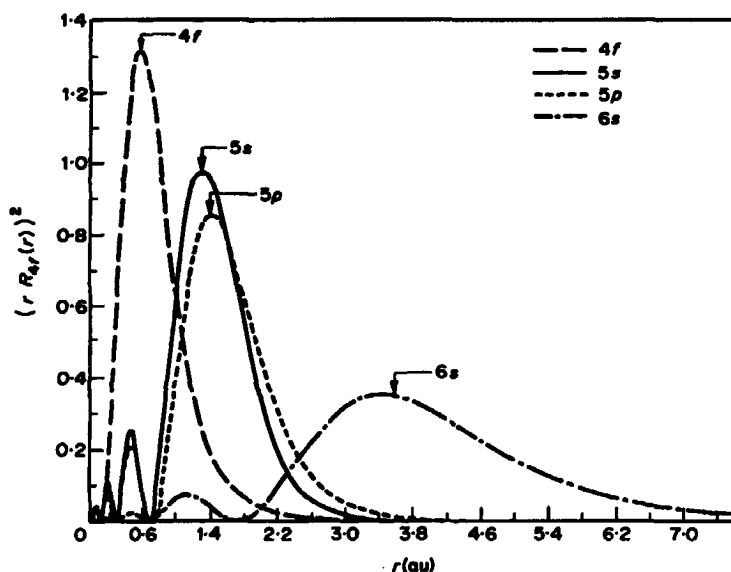


Figure 1.1: The Hartree-Fock radial densities for the $4f$, $5s$, $5d$ and $6s$ electrons of Gd^{3+} [1].

valence electrons ($5d$, $6s$) contribute to the metallic bond and therefore the $4f$ shell remains partially filled by electrons. As a consequence, rare earth atoms show substantial magnetic moments. In addition to this, the majority of $4f$ shells show a strong preferential orientation in a crystal lattice because of its aspherical electronic density. This R magnetic anisotropy is nowadays used to manufacture strong permanent magnets.

As the nuclear charge increases throughout the R series the potential seen by the $4f$ electrons deepens and their orbitals show a systematic contraction in radius, the lanthanide contraction. This effect is shown in table 1.1 where $\sqrt{\langle r^2 \rangle}$ is a measure of the $4f$ electron cloud radius. Because of the only modest variation in atomic radius of the R atoms, series of R compounds can often be realized with the same crystallographic structure, for example the series from LaNi_5 to LuNi_5 . This opens the opportunity for investigations of the magnetic rare earth properties on series of isotypic compounds.

In contrast to the localized magnetism of the rare earth atoms, the $3d$ transition metals (TM) show a delocalized, or itinerant, magnetism. The $3d$ electrons, which are the origin of the magnetic moment, are located at the outside of the electron cloud of the transition metal atom. Therefore contact between the $3d$ shells is realized and it is more appropriate to speak of band magnetism. The magnetic interaction between the transition metal atoms is therefore strong, and spontaneous macroscopic magnetism often exists at room temperature (an example is iron).

In this thesis the magnetic properties of different intermetallic compounds are studied. One of them, $R\text{FeAl}$, combines the magnetic properties of localized as well as itinerant magnetism, the others are fully described by the R magnetism. In this chapter a short introduction in (R) magnetism is given.

1.2 The magnetic moment of the rare earth atom

Each electron which is located in an electron cloud possesses a spin angular momentum \mathbf{s} and an orbital magnetic moment \mathbf{l} . The total spin and orbital magnetic moment of filled electron shells equals zero, but for partially filled electron shells this is not the case. If the spin orbit interaction of the individual electrons is small (coupling of \mathbf{l} and \mathbf{s}), the sum of the spins and the orbital magnetic moments of the individual electrons gives rise to a total spin angular momentum \mathbf{S} and total orbital angular momentum \mathbf{L} of the atom. The Russel-Saunders coupling between \mathbf{L} and \mathbf{S} gives rise to a total magnetic moment \mathbf{J} of the R atom. Hund's rules [2, 3] tell how to calculate S, L and J for the R series. First maximize S taking into account the Pauli principle, then maximize L and finally $J = |L - S|$ or $|L + S|$ for the first and second halves of the $4f$ shell (see table 1.1).

The orbit of the electron in its shell can be considered as a circular current and therefore a magnetic moment is associated with the orbital motion [4]. This magnetic moment equals $\mu_l = -\mu_B \mathbf{l}$ where μ_B is the Bohr magneton, a unit of atomic magnetism ($1 \mu_B = e\hbar/(2m_e) = 9.274 \cdot 10^{-24} \text{ J/T} (= \text{Am}^2)$). The magnetic moment associated with the spin angular momentum equals $\mu_s = -g_e \mu_B \mathbf{s}$ where g_e is the g -factor of the electron ($g_e = 2.002319304368(20)$ [5]). In contrast with μ_l , the origin of the magnetic moment of the electron is quantum mechanical. In fact, the precise experimental determination of the magnetic moment of the electron is a test for Quantum Electro Dynamics (QED) [5, 6].

The spin orbit interaction between \mathbf{S} and \mathbf{L} causes the latter two, and also μ_L and μ_S , to precess around \mathbf{J} . $\mu_T = \mu_L + \mu_S$ but because of the factor g_e the total magnetic moment μ_T makes an angle θ with \mathbf{J} . Therefore μ_T also precesses around \mathbf{J} and since its frequency is usually quite high only the component of μ_t along \mathbf{J} is observed. We obtain

$$\mu = \mu_T \cos \theta = -g_J \mu_B \mathbf{J} \quad (1.1)$$

where g_J is the Landé splitting factor which is determined by the atoms quantum numbers: $g_J = \frac{3J(J+1) + S(S+1) - L(L+1)}{2J(J+1)}$. The direction of \mathbf{J} is quantized and the projection of \mathbf{J} along a certain arbitrary quantization axis (usually called the z

Table 1.1: Some selected ionic properties of the rare earth elements and their electronic configuration.

<i>R</i> ion	$\sqrt{\langle r^2 \rangle_{4f}}$	$\alpha_J \cdot 10^2$	<i>S</i>	<i>L</i>	<i>J</i>	g_J	$g_J J$	$g_J \sqrt{J(J+1)}$
La ³⁺	4 <i>f</i> ⁰	0.610	0	0	0	-	0	0
Ce ³⁺	4 <i>f</i> ¹	0.578	-5.714	1/2	3	5/2	6/7	2.14
Pr ³⁺	4 <i>f</i> ²	0.550	-2.101	1	5	4	4/5	3.20
Nd ³⁺	4 <i>f</i> ³	0.528	-0.643	3/2	6	9/2	8/11	3.28
Pm ³⁺	4 <i>f</i> ⁴	0.511	+0.771	2	6	4	3/5	2.4
Sm ³⁺	4 <i>f</i> ⁵	0.496	+4.127	5/2	5	5/2	2/7	0.72
Eu ³⁺	4 <i>f</i> ⁶	0.480	0	3	3	0	0	0
Gd ³⁺	4 <i>f</i> ⁷	0.468	0	7/2	0	7/2	2	7
Tb ³⁺	4 <i>f</i> ⁸	0.458	-1.010	3	3	6	3/2	9
Dy ³⁺	4 <i>f</i> ⁹	0.450	-0.635	5/2	5	15/2	4/3	10
Ho ³⁺	4 <i>f</i> ¹⁰	0.440	-0.222	2	6	8	5/4	10
Er ³⁺	4 <i>f</i> ¹¹	0.431	+0.254	3/2	6	15/2	6/5	9
Tm ³⁺	4 <i>f</i> ¹²	0.421	+1.010	1	5	6	7/6	7
Yb ³⁺	4 <i>f</i> ¹³	0.413	+3.175	1/2	3	7/2	8/7	4
Lu ³⁺	4 <i>f</i> ¹⁴	0.405	0	0	0	-	0	0

axis), m_J , can only take integer or half integer values: $m_J = -J, -J + 1, \dots, J - 1, J$. In the presence of an external field, the field direction determines the direction of quantization for a free particle and J_z is observed as the moment of the magnetic atom. J_z and J^2 are used to characterize the moment of the atom because they commute (J and J_z don't):

$$J^2 = \mathbf{J} \cdot \mathbf{J} = J(J+1) \quad (1.2)$$

As a result the magnetic moment and its z component equal:

$$\mu = g_J \mu_B \sqrt{J(J+1)} \quad (1.3)$$

$$\mu_z = -g_J \mu_B m_J \quad (1.4)$$

μ_z is always smaller than μ and if the atomic moment has a certain preferential direction it will never show its maximum value. For an ensemble of atoms without a preferential orientation however, the $2J + 1$ manifold of quantization directions are all statistically occupied and $\mu \propto \sqrt{J(J+1)}$ is observed. This is the case in for example the paramagnetic state of a magnet (eq. (1.6))

For a free ion the $2J + 1$ manifold is degenerate, but a magnetic or electric field can lift this degeneracy. The first situation can be realized by an external magnetic field and the second situation occurs when the ion is incorporated into a crystalline lattice.

1.3 Magnetic interactions

Rare earth intermetallics can be regarded as a system consisting of an assembly of many magnetic moments located at the R atoms. If these magnetic moments are non interacting, the macroscopic magnetic properties of the compound can be described by m_J , J and the number of R atoms N . In this paramagnetic state the $2J+1$ manifold is degenerate, but this degeneracy is lifted in an external magnetic field B_{ext} :

$$E_B = -\boldsymbol{\mu} \cdot \mathbf{B}_{\text{ext}} = -\mu_z B_{\text{ext}} = g_J m_J \mu_B B_{\text{ext}} \quad (1.5)$$

The magnetic energy E_B is proportional to m_J which results in equidistant energy levels. The thermal population of these energy levels governs the total magnetization, $M = N\langle\mu_z\rangle$, of the compound. The magnetic susceptibility is defined as $\chi = M/B_{\text{ext}}$ and it can be shown that (Curie law):

$$\chi = \frac{Ng_J^2\mu_B^2 J(J+1)}{3kT} = \frac{C}{T} \quad (1.6)$$

where T is the temperature and C the Curie constant.

Often interactions between the atomic magnetic moments cannot be neglected. The Heisenberg exchange interaction between neighbouring spins equals:

$$\mathcal{H}_{ex} = -2\mathcal{J}\mathbf{S}_i \cdot \mathbf{S}_j \quad (1.7)$$

where \mathcal{J} is the exchange constant. This interaction is a result of the Pauli principle which modifies the charge distribution according to the spin orientation (see for example [7]). In general \mathcal{H}_{ex} is assumed zero for next-nearest-neighbours. For a positive \mathcal{J} a parallel alignment of the spin is preferred and ferromagnetic correlations are promoted. Long range ferromagnetic order exists below the Curie temperature, T_C (see Fig. 1.2). For a negative \mathcal{J} an antiparallel alignment is energetically more favourable and antiferromagnetism is observed below the Néel temperature T_N (see Fig. 1.2). Because spontaneous magnetization occurs below T_C , χ diverges towards infinity at this temperature. The paramagnetism ($T > T_{C,N}$) is in both cases described by the Curie-Weiss law:

$$\chi = \frac{C}{T - \theta} \quad (1.8)$$

where θ equals T_C for ferromagnets while θ can adopt negative values for antiferromagnets and an $1/\chi$ versus T plot shows a linear relation between $1/\chi$ and T and the intersection with $1/\chi = 0$ determines θ .

For TM metals the exchange interaction is substantial because the $3d$ electronic shells overlap each other and realize a direct contact. This is not the case for the R metals because the $4f$ shells are more localized inside the electron cloud. There is no direct exchange interaction possible and the magnetic interaction is mediated via the polarization of the conduction electrons (primarily $5d$). This RKKY

(Ruderman-Kittel-Kasuya-Yosida) interaction has a long range oscillatory nature falling off as $\cos(2k_f r)/r^3$, with k_f the wave vector of electrons at the Fermi surface and r the distance from the $4f$ magnetic moment. Because of the oscillatory nature, ferro- and antiferromagnetic interactions are possible, depending on the arrangement of the magnetic atoms in the lattice. The RKKY interaction is of relatively long range because the conduction electrons form a continuum throughout the lattice. Therefore also distant neighbour interactions have to be considered between the R moments. This possibly results in complex magnetic structures as is observed in the R metals (see Fig. 1.2).

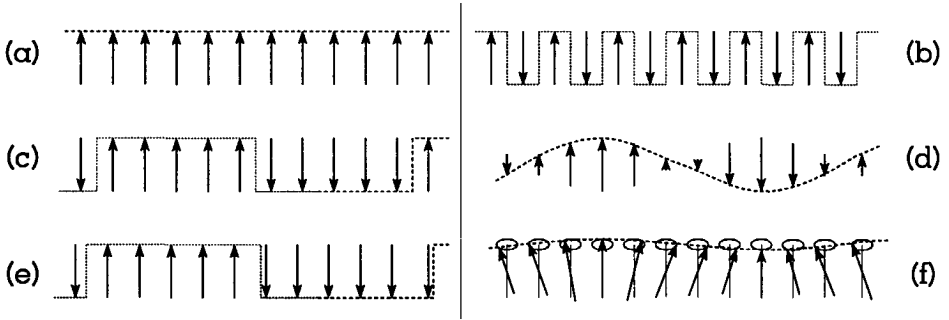


Figure 1.2: Possible arrangements of magnetic moments in the ordered state. The length of the arrows is related to the size of the magnetic moment and the center of the atomic host is located in the middle of the arrows. The dotted line indicates the wave of the modulation (see also sec. 2.4.3). The magnetic structure is called commensurate if its periodicity contains an integer number of crystallographic unit cells and if the magnetic periodicity does not match the periodicity of the crystal, it is called incommensurate. (a) ferromagnet, (b) antiferromagnet, (c) long range commensurate antiferromagnet, (d) sine modulated spin density wave, (e) long range incommensurate (note that period of the wave modulation does not match the periodicity of the lattice), (f) helical structure (moment size is equal at all atomic positions but rotates from site to site).

In general, a magnetic moment generates magnetic field lines leaving from the top of the magnetic moment, also called the north pole, and arriving at the south pole. The dipolar field due to a single magnetic moment \mathbf{M} at a distance \mathbf{r} from this moment equals:

$$\mathbf{B}_{\text{dip}}(\mathbf{r}) = \frac{-\mathbf{M}}{r^3} + \frac{3(\mathbf{M} \cdot \mathbf{r})\mathbf{r}}{r^5} \quad (1.9)$$

The dipolar field lines are drawn in Fig. 1.3 and a magnetic moment located in the neighbourhood of \mathbf{M} will orient itself along the direction of these field lines. Because of the $1/r^3$ dependence the dipolar interaction is often not important when considering the magnetic interactions between atomic moments in the solid state. The direct and indirect exchange interactions dominate in general.

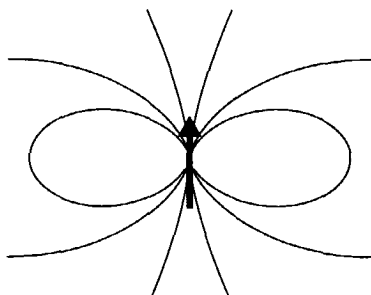


Figure 1.3: Dipolar field generated by a single magnetic moment. The tangent of the field lines indicates the direction of the dipolar field $\mathbf{B}_{\text{dip}}(\mathbf{r})$ as expressed by eq. (1.9) at this point.

The dipolar interaction is of importance in $\mu^+\text{SR}$, where muons are implanted interstitially in the lattice (see sec. 2.3). The strong angular dependence of \mathbf{B}_{dip} causes the dipolar field to be a muon site characteristic. This property is used in $\mu^+\text{SR}$ Knight shift measurements (see sec. 6.2).

1.4 Crystal field theory

In intermetallics the R atom is often located at well defined positions in the crystal lattice. The local environment is then identical for R atoms located at identical lattice sites. For the majority of R atoms, the $4f$ shell is non spherical (see Fig. 1.4) and the electronic $4f$ shell shows a preferential orientation in the lattice in order to minimize the Coulomb interaction with the surrounding charges. The electrostatic potential due to the surrounding ions in the approximation of point charges equals:

$$V(r, \theta, \phi) = \sum_j \frac{Z_j}{|R_j - r|} \quad (1.10)$$

where Z_j and R_j are the charge and position of the ligands and r is the position vector of the $4f$ electron. The magnetic ion has electronic charges q_i located at (r_i, θ_i, ϕ_i) and the summation over all n_{4f} electrons in the unfilled electron shell gives:

$$\mathcal{H}_{cf} = \sum_{i=0}^{n_{4f}} q_i V_i = -|e| \sum_i V_i(r_i) \quad (1.11)$$

with \mathcal{H}_{cf} the crystal field hamiltonian and e the electronic charge. Since the charge in the crystal lattice is located outside the unpaired electron shell \mathcal{H}_{cf} can

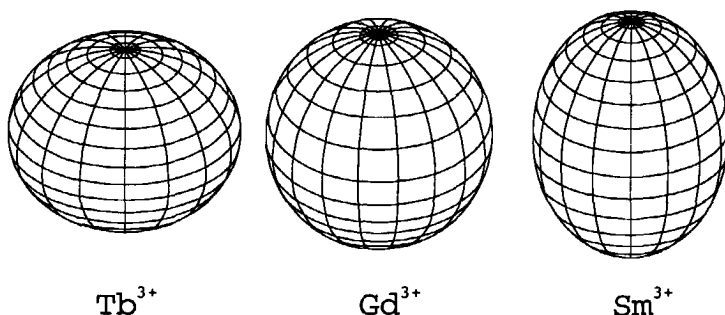


Figure 1.4: Electron density surface of three $4f$ shells selected from the R series. The cigar and discus shaped electron clouds show opposite preferential directions in the crystalline electric field.

be expanded in spherical harmonics:

$$\mathcal{H}_{cf} = \sum_{n=0}^{\infty} \sum_{m=-n}^n A_n^m \sum_{k=1}^{n_{4f}} r_k^n Y_n^m(\theta_k, \phi_k) \quad (1.12)$$

Here A_n^m are the coefficients of this expansion and their value is determined by the symmetry and structure of the lattice. In a method developed by Stevens [8], the cartesian coordinates (x, y, z) are replaced by the operator equivalents J_x , J_y and J_z to give O_n^m :

$$\mathcal{H}_{cf} = \sum_{n=0}^{\infty} \sum_{m=-n}^n \theta_n \langle r^n \rangle A_n^m O_n^m = \sum_{n=0}^{\infty} \sum_{m=-n}^n B_n^m O_n^m \quad (1.13)$$

The operator equivalents O_n^m are listed in ref. [8, 9] and are fully determined by the quantum numbers J, J_x, J_y and J_z of the magnetic ion. $\langle r^n \rangle$ is the n -th power of the radial extent of the $4f$ electrons, θ_n are constants for a certain R atom (listed in [1]) and A_n^m (or B_n^m) are called crystal field parameters (CFP). For an oblate, discus like $4f$ shell, $\theta_2 = \alpha_J < 0$ and for an prolate, cigar shaped shell $\alpha_J > 0$ (see table 1.1). For $4f$ electrons n (eq. (1.13)) cannot exceed 6 and must be even because of the inversion symmetry of the crystalline electric field. The local symmetry of the crystal lattice at the R site determines the number of B_n^m parameters necessary to describe the crystal field. Examples of \mathcal{H}_{cf} for different space groups are given in eq. (3.1) and eq. (4.1).

\mathcal{H}_{cf} describes the splitting of the $2J + 1$ manifold of the $4f$ shell. Being a free ion, the $2J + 1$ manifold would be completely degenerate but because of the interaction of the crystal field with the non spherical $4f$ shell the degeneracy is lifted. The B_n^m parameters govern this splitting and determine the ground state crystal field level. The wavefunctions Γ_i of the crystal field split $2J+1$ manifold

are linear combinations of the free ion states:

$$\Gamma_i = \sum_{m_J} c_{m_J} |J, m_J\rangle \quad (1.14)$$

There are two theorems which influence the crystal field level scheme. Firstly the **Kramers theorem**. In the absence of an applied field the levels of an ion with an odd number of $4f$ electrons (half integral J) can at most be split into levels which are doubly degenerate. Secondly, the **Jahn-Teller effect**. The symmetry of the environment of an ion with a degenerate ground state, Kramers' doublets excepted, is lowered to remove the degeneracy. In effect, the non-Kramers ion is slightly displaced from its original site. The elastic energy increases but the energy of the crystal field ground state is reduced. This rule does not apply to excited states.

At zero Kelvin all the atoms occupy the crystal field ground state. The thermal population of the crystal field levels governs the temperature dependence of the R magnetism.

The magnetocrystalline anisotropy energy, E_A , equals in uniaxial symmetric materials:

$$E_A = K_1 \sin^2 \theta + K_2 \sin^4 \theta \quad (1.15)$$

where $K_{1,2}$ are anisotropy constants and θ is the angle between the easy magnetization direction and the c axis. The single rare earth ion contribution to the magnetic anisotropy is directly related to the crystalline electric field via:

$$K_1 = -\frac{2}{3} B_2^0 \langle O_2^0 \rangle - 5 B_4^0 \langle O_4^0 \rangle \quad (1.16)$$

$$K_2 = \frac{35}{8} B_4^0 \langle O_4^0 \rangle \quad (1.17)$$

1.5 About magnetic phase transitions

The transition from the paramagnetic to the magnetically ordered state occurs because below $T_{C,N}$ the Gibbs free energy G of the ordered phase is lower than G of the disordered phase. In general, the transition mechanism can be divided in two types, first and second order phase transitions [2, 3, 10, 11].

For a first order transition $\frac{\partial G}{\partial T}$ of the system is discontinuous because G of the two phases cross each other at the transition temperature. Since the entropy $S = -(\frac{\partial G}{\partial T})_P$ and $G = H - TS$ with H the enthalpy of the system, the discontinuous change in H gives rise to latent heat. The specific heat ($c_p = (\frac{\partial H}{\partial T})_P$), see sec. 2.5.2) becomes infinite at the transition temperature because the addition of heat converts the system from one phase to the other without changing the temperature. Examples are the transition from liquid water to vapour and crystallographic transitions. Another example of a first order transition is between two phases with different magnetic structures. If the transition from the paramagnetic to the magnetically ordered state is first order, this is characterized by the

coexistence of both phases at the transition temperature, temperature hysteresis and a discontinuity in the spontaneous magnetization.

However, most transitions from the paramagnetic to the magnetically ordered phase are second order. Second order phase transitions are characterized by branching of G below the transition temperature. Often the internal symmetry of the system is altered, such as from disorder to order. $\frac{\partial G}{\partial T}$ is continuous and no latent heat is involved at the transition temperature. The spontaneous magnetic moments grows gradually below the ordering temperature and there is no hysteresis nor the coexistence of both phases. The specific heat shows a λ type anomaly (looks like a λ) at the transition temperature.

Spontaneous magnetic order characterizes the transition from the paramagnetic to the magnetically ordered state. This spontaneous magnetic order gives rise to an internal magnetic field. In the molecular field approximation the magnetic interaction is described by an effective average field, the so called molecular or Weiss field \mathbf{B}_M . This field is obtained by the nearest neighbour sum of the exchange interaction of eq. (1.7). The hamiltonian equals:

$$\begin{aligned}\mathcal{H}_M &= -\sum_{nn} 2J_{ij} \mathbf{S}_i \cdot \mathbf{S}_j = -2Z J_{nn} \mathbf{S} \cdot \langle \mathbf{S} \rangle = -2Z J_{nn} (g_J - 1)^2 \mathbf{J} \cdot \langle \mathbf{J} \rangle \\ &= -g_J \mu_B \mathbf{J} \cdot \mathbf{B}_M\end{aligned}\quad (1.18)$$

where Z is the number of nearest neighbour (nn) magnetic moments and $\mathbf{B}_M = 2Z J_{nn} \langle \mu \rangle (g_J - 1)^2 / g_J^2 \mu_B^2$. This molecular field hamiltonian lifts the degeneracy of the $4f$ crystal field levels and generates a magnetic moment in the crystal field ground state. This magnetic moment enlarges the molecular field which in turn enlarges the magnetic moment of the $4f$ shell until an equilibrium is achieved. For this process to occur, the $4f$ shell needs a doublet as crystal field ground state. However, for singlet crystal field ground states, the magnetic moment can be induced if the molecular field is of comparable size as the distance between the singlet ground state and the higher crystal field levels. This type of magnetic order is realized in PrRu_2Si_2 and discussed in chapter 5.

Hybridization effects between the $4f$ and conduction electrons can cause a substantial dispersion of the (lowest) crystal field levels. This dispersion is not taken into account by crystal field theory (sec. 1.4) and the molecular field approximation. Often this dispersion is small compared with the distance between the crystal field levels and can be ignored. However, in some special situations it can cause a profound change in the magnetic behaviour of the compound (see the random phase approximation in sec. 5.3.4).

Experimental principles

Abstract

The basic principles of the experimental techniques used in this thesis are discussed. The specific experimental conditions are described in the individual chapters.

2.1 Introduction

For the studies described in this thesis various experimental techniques were used to characterize the samples and to understand the physical behaviour of the subject under study. The experimental details are described in the individual chapters. Here the general principles of Mössbauer spectroscopy as well as the Muon Spin Rotation and Relaxation technique are described. Both techniques were used intensively during the studies of this thesis and deserve some attention. The essentials of further complementary techniques are described in the last sections of this chapter.

2.2 Mössbauer spectroscopy

In 1957 R.L. Mössbauer discovered that nuclei imbedded in solids can show recoilless absorption and emission of radiation [12, 13]. The bond of the nuclei with the solid results in quantization of the recoil energy and therefore a part of the nuclei, the recoilless fraction f , shows a zero recoil energy. This phenomenon made resonant absorption of nuclear radiation possible and small variations in the nuclear energy levels could now be studied. In general, a source is used for which the nuclear properties are well known. The parent isotope is unstable and decays to the Mössbauer nucleus via β^+ -decay. The Mössbauer nucleus, which is formed in an excited state, emits a γ ray to achieve its ground state. With the use of a drive unit the source is given a velocity and the emitted gamma ray energy is modified by the doppler shift. The absorber, the sample under study, absorbs this energy if the gamma ray energy matches the energy difference between the ground and excited nucleus. Of course, this generated excited nucleus emits also a γ quantum, but since this emission takes place into all directions, these γ rays are lost for detection.

The variation in doppler velocity creates a spectrum of gamma energies and some of them are absorbed by the absorber. This principle is drawn in Fig. 2.1. The recorded Mössbauer spectrum shows a number of absorption lines of which the specific energies are characteristics of the environment of the Mössbauer nuclei in the absorber. A nice example of a ^{169}Tm Mössbauer spectrum is presented in the top of Fig. 3.2. From the number and positions of the lines the electronic charge density, the electric field gradient as well as the magnetic field at the nuclear site can be deduced. These features are described in section 2.2.1, 2.2.2 and 2.2.3.

For a nucleus to be a Mössbauer nucleus it needs a substantial recoil free fraction recoilless fraction f :

$$f = \exp(-k^2 \langle x^2 \rangle) \quad (2.1)$$

where k is the wavevector of the emitted or absorbed gamma ray and $\langle x^2 \rangle$ the temperature average square displacement of the nucleus from its mean position. For the Mössbauer effect to be visible, a non zero f is necessary for the source as well as the absorber.

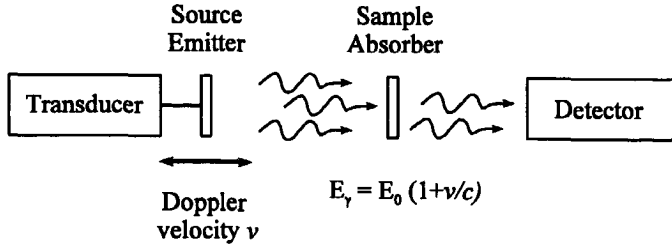


Figure 2.1: Principle of Mössbauer spectroscopy. A simplified set-up.

2.2.1 Isomer shift

The Coulomb interaction between the nucleus and the penetrating electronic charge results in a shift of the nuclear energy. A simple expression for the energy shift of a nuclear level, δE , due to the non zero s electron density at the nucleus, equals [14]:

$$\delta E = \frac{2\pi}{5} Z e^2 |\Psi(0)|^2 R^2 \quad (2.2)$$

with Z the nuclear charge, $|\Psi(0)|^2$ the electron density at the nucleus and R the nuclear radius. Notice that if $R = 0$ (point charge approximation), $\delta E = 0$. Due to a difference in radius between the ground state and excited (isomeric) nucleus there is a difference $(\delta E_{\text{ex}} - \delta E_{\text{gd}})$ between the energy shift in ground (gd) and excited (ex) state. Consequently, the energy of the emitting or absorbing gamma ray of this nucleus is shifted with $(\delta E_{\text{ex}} - \delta E_{\text{gd}})$. The resonant energy between the source and absorber is called the isomer shift (IS) and equals:

$$\text{IS} = (\delta E_{\text{ex}} - \delta E_{\text{gd}})_{\text{abs}} - (\delta E_{\text{ex}} - \delta E_{\text{gd}})_{\text{source}} \quad (2.3)$$

$$= \frac{2\pi Z e^2}{5} (R_{\text{ex}}^2 - R_{\text{gd}}^2) (|\Psi(0)|_{\text{abs}}^2 - |\Psi(0)|_{\text{source}}^2) \quad (2.4)$$

IS is sensitive to changes in the s electron density and probes for example the valency of an atom.

2.2.2 Quadrupole splitting

The quadrupole moment of the nucleus interacts with the electric field gradient at the nuclear site via the quadrupolar interaction. This results in a splitting of the nuclear energy levels with different $\pm m_I$. A discus like nucleus has a negative quadrupole moment and a cigar shaped nucleus a positive quadrupole moment Q . Nuclei with a spin $I = 0$ or $I = \frac{1}{2}$ are spherically symmetric and show for this reason no quadrupole splitting. The shift in nuclear energy due to this quadrupole interaction equals:

$$E_Q(m_I) = \frac{V_{zz}Q}{4I(2I-1)} |3m_I^2 - I(I+1)| \sqrt{1 + \frac{1}{3}\eta^2} \quad (2.5)$$

Table 2.1: Some properties of a few Mössbauer nuclei. E_γ is the energy of the Mössbauer ground state γ ray transition, I the spin and π the parity, Q the quadrupole moment and μ the magnetic moment of the excited nucleus (ex) and its ground state (gd).

Property	^{57}Fe	^{141}Pr	^{166}Er	^{169}Tm
E_γ (keV)	14.4	145.4	80.56	8.40
$I_{\text{ex}}, I_{\text{gd}}$	$\frac{3}{2}^-, \frac{1}{2}^-$	$\frac{7}{2}^+, \frac{5}{2}^+$	$2^+, 0^+$	$\frac{3}{2}^+, \frac{1}{2}^+$
Q_{ex} (barn)	0.29	0.28	-1.59	-1.20
Q_{gd} (barn)	0	-0.059	0	0
$\mu_{\text{ex}} (\mu_N)$	-0.153	2.80	0.63	-0.23
$\mu_{\text{gd}} (\mu_N)$	0.093	4.28	0	0.10
Line width (mm/s)	0.33	1.02	1.89	8.33
Parent isotope	^{57}Co	^{141}Ce	^{166}Ho	^{169}Er
Source material	Rh: ^{57}Co	$^{141}\text{CeF}_3$	$^{166}\text{HoPd}_3$	$^{169}\text{ErAl}_3\text{-Al}$
Source half life	271.3d	32.5d	27h	9.4d
Source at 4.2 K	no	yes	yes	no
Application	IS, QS, HF	IS, HF	QS, HF	QS, HF

where $\eta = (V_{xx} - V_{yy})/V_{zz}$ and V_{ii} is an abbreviation of $\partial^2 V / \partial i^2$, an axial component of the diagonalized electric field gradient tensor. For the Tm and Fe nuclei $I_{\text{gd}} = \frac{1}{2}$ and $I_{\text{ex}} = \frac{3}{2}$. In these cases, the nuclear ground states do not show quadrupole splitting but the excited states have energy splittings $\Delta E_Q = \frac{1}{2} V_{zz} Q$ and this splitting (QS) is observed in the Mössbauer spectrum (see for example Fig. 4.2).

For rare earth atoms, QS is due to the electrostatic interaction between the quadrupole moment of the nucleus and the electric field gradient caused by the asymmetric $4f$ shell and the crystal field of the lattice. Therefore QS can be decomposed into two components, QS^{4f} and QS^{latt} :

$$QS(T) = QS^{4f}(0) \langle 3J_z^2 - J(J+1) \rangle_{4f}^T + QS^{\text{latt}} \quad (2.6)$$

with $QS^{4f}(0)$ corresponding to the free ion value of the $4f$ contribution, $\langle \rangle_{4f}^T$ indicating the thermal average over the $4f$ crystal field levels and J, J_z , the total angular momentum and its z component. QS^{latt} is temperature independent and determined by the crystal field of the electric charges surrounding the $4f$ shell. The first term is the contribution from the $4f$ shell which is strongly temperature dependent and is determined by the crystal field. It becomes negligible at high

temperature because $\langle 3J_z^2 - J(J+1) \rangle_{4f}^{T \rightarrow \infty} = 0$. QS^{latt} is related to V_{zz}^{latt} by:

$$QS^{\text{latt}} = \frac{1}{2} |e| V_{zz}^{\text{latt}} Q \quad (2.7)$$

where e is the electronic charge. Since the thermal population of the different crystal field levels of the $2J+1$ multiplet determines $\langle 3J_z^2 - J(J+1) \rangle_{4f}$ and therefore $QS(T)$, possible sets of CFP can be deduced from the Mössbauer data.

Although V_{zz}^{latt} is measured at the nucleus and the crystal field parameter B_2^0 is related to the electric field gradient experienced by the $4f$ shell, there is an empirical relation between the two. This relationship equals:

$$V_{zz}^{\text{latt}} = -4 c B_2^0 / \alpha_J \langle r^2 \rangle \quad (2.8)$$

with c a constant which equals 185 for Tm [15], α_J the second order Stevens parameter and $\langle r^2 \rangle$ the radial integral of the $4f$ electron cloud.

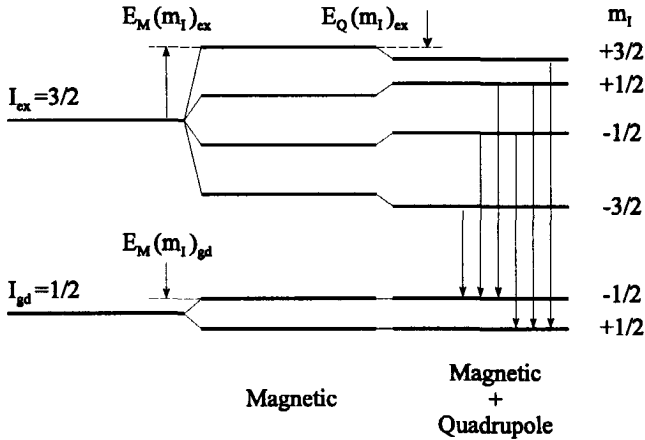


Figure 2.2: Hyperfine structure in the nuclear energy levels of the ^{169}Tm isotope and the γ transitions (not on scale).

2.2.3 Magnetic hyperfine field

Another contribution to the hyperfine structure of the nuclear energy levels is realised by the magnetic interaction between the nuclear magnetic dipole moment and the magnetic field generated by its own electrons. The magnetic field generated by a magnetic electronic shell at the nuclear site is large and the shift of the nuclear energy level equals:

$$E_M(m_I) = -g_N \mu_N m_I B \quad (2.9)$$

where g_N is the nuclear gyromagnetic ratio which is related to the composition of the nucleus (i.e. how the nucleons are organized) and $\mu_N = e\hbar/2m_p$ the nuclear

magneton (m_p is the mass of the proton). This results in $2I_{gd}+1$ or $2I_{ex}+1$ equidistant energy levels for the nuclear ground or excited state, respectively. The maximum energy difference between the γ -transitions is related to the hyperfine field. By comparison of the measured hyperfine field with the free ion value (maximum moment size), the magnetic moment of the electronic shell can be deduced (For Tm: $7\mu_B \equiv 720$ T).

2.2.4 Nuclear transitions

A gamma transition between the ground and excited nuclear level must conserve the z -component of angular momentum and as a result the angular momentum L carried off by the gamma ray must satisfy [14]:

$$|I_{ex} - I_{gd}| \leq L \leq |I_{ex} + I_{gd}| \quad (2.10)$$

$$L \neq 0 \quad (2.11)$$

Transitions between the nuclear sublevels are limited by $|\Delta m| \leq L$. The level scheme of the ^{169}Tm Mössbauer nucleus is drawn in Fig. 2.2. For the other isotopes it can be deduced from table 2.1 and the equations presented in secs. 2.2.1, 2.2.2, 2.2.3.

2.3 μ^+ SR Spectroscopy

In the same year that Mössbauer founded the basis for Mössbauer spectroscopy, the possibility of using muons as a probe for condensed matter was suggested [16, 17]. But it wasn't until the seventies that attempts were made to develop such a technique. Nowadays μ^+ SR (Muon Spin Rotation or Relaxation) is commonly used at some large facilities to study condensed matter.

Table 2.2: Some selected properties of the muon μ^+ [5, 16, 18].

Property	Value
Mass	$m_\mu = 105.6595 \text{ MeV} / c^2$ $= 0.1126096 \times m_p$ $= 206.76835(11) \times m_e$
Charge	$+e$
Spin	$S_\mu = \frac{1}{2}$
g-factor	$g_\mu = 2.002331846(16)$
Magnetic moment	$\mu_\mu = g_\mu e\hbar / (2m_\mu) = 4.8410^{-3} \mu_B = 3.18 \mu_N$
Gyromagnetic ratio	$\gamma_\mu = 2\pi \times 135.539 \text{ MHz T}^{-1}$
Lifetime	$\tau_\mu = 2.1914 \mu s$

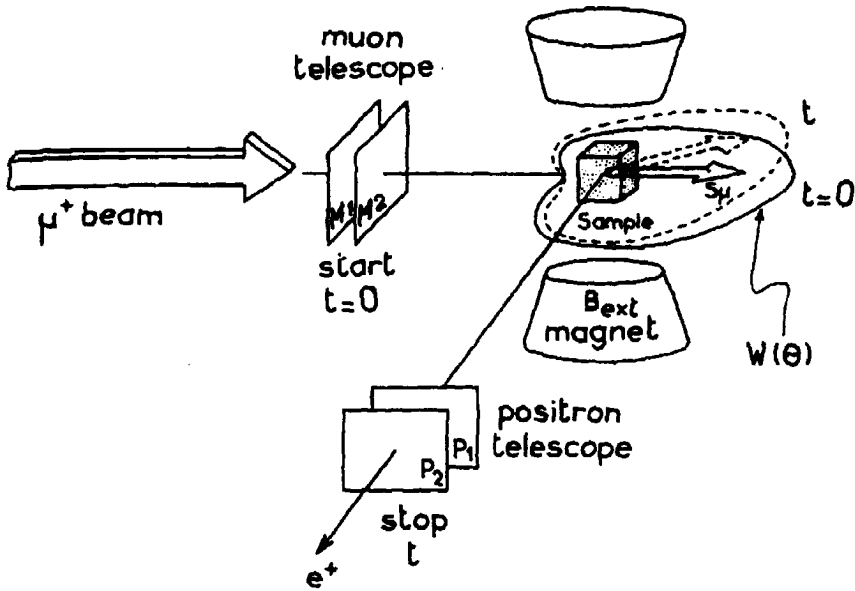


Figure 2.3: Principle of the μ^+ SR technique. The naturally polarized muons are implanted into the sample where they decay into a positron and two neutrinos ($\tau_\mu = 2.2\mu s$). The positron is emitted preferentially along the muon spin direction ($W(\theta)$, eq. (2.16)) and is energetical enough to leave the sample and to be detected. By detecting the number of positrons along two different directions with respect to the muon beam polarization, the depolarization of the muon ensemble can be observed as function of time.

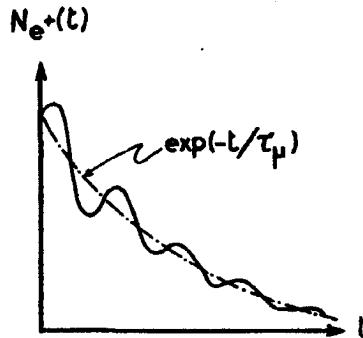


Figure 2.4: Example of the number of positrons detected in a single detector N_{e^+} . The modulation results from the precession of the muon spin.

The muon, μ^+ , is an elementary antiparticle of which the fundamental properties are listed in table 2.2. It is produced via colliding high energy protons (energy $\simeq 600$ MeV - 1 GeV) with a light target (C or Be) [18] :

$$p + p \rightarrow \pi^+ + p + n \quad (2.12)$$

$$p + n \rightarrow \pi^+ + n + n \quad (2.13)$$

Pions (π^+) are formed with a lifetime of 26 ns which decay into a muon and a neutrino:

$$\pi^+ \rightarrow \mu^+ + \nu_\mu \quad (2.14)$$

The pion is a spin zero particle but μ^+ as well as ν_μ show $s = \frac{1}{2}$. Because the neutrino is massless or almost massless and travels at the speed of light or almost at the speed of light, its spin can only be oriented along its direction of motion since its perpendicular dimensions diminish according to Einstein's theory of relativity. The weak interaction which is responsible for the pion decay, violates parity conservation and therefore ν_μ has a negative helicity and its spin is always oriented antiparallel to its momentum [19]. As a consequence the muon also shows a spin direction antiparallel to its velocity and the produced muon beam is polarized [18] or almost polarized if the pions are not decaying at rest. As described later, this is one of the properties of the muon beam necessary to perform μ^+ SR.

The muon beam (50-100 MeV) is directed onto the sample and the muons are implanted in the material. There they thermalize and come to rest after $\sim 10^{-9}$ s. Apart from ionizing the atoms of its host, it also produces vacancies during the first part of its path through the sample. This has no consequence for the experimental results since the area where the muon finally localizes is unaffected.

In a crystallographic environment, the muon localizes interstitially. In insulators and semiconductors the muon forms a bound state with an electron of its host, muonium (μ^+e^-), a light version of the hydrogen atom. In metals however the charge of the muon is screened by an electron cloud formed by the host's conduction band.

After localization the muon spin interacts with the surrounding matter before it decays to a positron and two neutrinos:

$$\mu^+ \rightarrow e^+ + \nu_e + \bar{\nu}_\mu \quad (2.15)$$

The positron has enough energy to leave the sample and can be detected. Moreover, the positron is emitted preferentially along the spin direction of the muon as a consequence of parity violation in the weak interaction. The angular distribution of the probability of positron emission, $W(\theta)$, is given by (see also Fig. 2.3):

$$W(\theta) = 1 + A_0 \cos \theta \quad (2.16)$$

where A_0 determines the initial asymmetry and depends on the energy selection of the positrons. θ is the angle between the direction of the emitted positron and

the muon spin. The above mentioned properties make it possible to determine the muon spin direction by detecting the positrons at two different directions with respect to the sample. A schematic setup is drawn in Fig. 2.3. A pulse of muons is implanted into the sample and the number of positrons are detected as function of time in different detectors.

Because of the limited life time of the muons, τ_μ , the number of detected positrons N_{e+} equals:

$$N_{e+}(t) = N_{e+}(0) \exp\left(\frac{-t}{\tau_\mu}\right) \quad (2.17)$$

Introducing the asymmetry of the number of positrons in the forward (F) and backward (B) direction we obtain:

$$N_F(t) = N_{e+}(t)(1 + A(t) \cos \theta_F) \quad (2.18)$$

$$N_B(t) = N_{e+}(t)(1 + A(t) \cos \theta_B) \quad (2.19)$$

The $\cos \theta_{F,B}$ values are setup characteristics and are determined independently. From eqs.(2.18) and (2.19), $A(t)$ can be deduced with $A(t) = R(N_F - N_B)/(N_F + N_B)$ where R is a setup constant. $A(t)$ contains interesting information about the sample and equals in general (see also Fig. 2.4):

$$A(t) = A(0) G(t) \cos(\omega_\mu t) \quad (2.20)$$

The local magnetic field experienced by the muon, B_μ , causes the muon spin to precess with a frequency $\omega_\mu = \gamma_\mu B_\mu$, where γ_μ is the gyromagnetic ratio of the muon (see table 2.2). Because of eq. (2.16) this frequency is directly observed in the μ^+ SR spectrum (Fig. 2.4). Of course, when no magnetic field is present or when $B_\mu \parallel S_\mu$ no precession frequency is observed but just $G(t)$. $G(t)$ is the depolarization function which reflects the depolarization of the polarized muon ensemble due to the interaction with its host. $G(t)$ can show different time structures depending on the origin of the depolarization, i.e. whether it is static or dynamic, due to a magnetic field distribution or due to for example phonons. For a detailed description we refer to refs. [16, 18, 20]. Here a few basic examples will be given necessary to understand the experiments presented in this thesis. If the depolarization is a result from a continuous and isotropic gaussian distribution (width Δ) of static fields we obtain for example:

$$G(t) = \exp\left(-\frac{1}{2}\Delta^2 t^2\right) \quad (2.21)$$

In the case of fast fluctuating fields with a correlation time τ_c , $G(t)$ equals:

$$G(t) = \exp(-\lambda t) = \exp(-\Delta^2 \tau_c t) \quad (2.22)$$

where λ is the damping rate. This latter expression is often used to describe the muon signal in the paramagnetic state of its host (see Fig. 5.5). λ diverges when the critical magnetic fluctuations are slowing down.

In chapter 6 μ^+ SR Knight shift measurements are described. This technique is commonly used to determine the muon location site in its host. For a detailed description of this technique we refer to section 6.2.

2.4 Neutron techniques

The neutron is a useful tool for the study of condensed matter because its wavelength as well as its energy can be of comparable size as crystallographic dimensions and thermal vibrations. Because it has no electric charge, it only interacts with the nuclei of the material under study. The magnetic moment of the neutron, $\mu_n = g_n \mu_N = 5.4 \cdot 10^{-4} \mu_B$ with $g_n = -1.91$ the gyromagnetic ratio of the neutron, interacts with electronic magnetic moments of the material. The neutrons penetration depth is large and elastic and inelastic scattering of the neutrons reveal information about the nuclei and the magnetic moment of the electronic shells. The neutron cross section at thermal energy shows a irregular behaviour throughout the periodic table. Some nuclei even show negative cross sections (for example hydrogen and ^{62}Ni) and therefore neutron diffraction can be a welcome addition to X-ray diffraction. In this section a brief description is given; for a thorough inspection of neutron scattering we refer to refs. [21, 22, 23].

The energy of the neutron, $E_n = \frac{1}{2} m_n v^2$, is in general between 2 meV (cold neutrons) and 200 meV (hot neutrons). Interatomic distances and thermal excitations are comparable in size with the neutron wavelength and energy and are therefore comfortably observed. The neutron has a De Broglie wavelength $\lambda_n = h/m_n v$ and its wavevector equals $k = 2\pi/\lambda_n$.

Neutrons can be produced via two principles. In a nuclear reactor the neutrons originate from nuclear fission of uranium. Whereas for energy production the energy of the fission is valuable, physicists prefer the neutrons produced in the chain reaction. Neutrons produced this way are moderated in the reactor core (institutes as IRI (Delft, the Netherlands), HMI (Berlin, Germany) and ILL (Grenoble, France)). In a spallation source, protons bombard a target (often uranium or tantalum) and pulses of neutrons are generated (institutes such as ISIS (Didcot, United Kingdom)). These pulses are moderated to obtain the desired neutron energy.

Because magnetic scattering of the neutrons depends on their spin orientation, a polarized neutron beam can be produced via constructive interference of magnetic and nuclear scattering; one spin state is transmitted whereas the opposite spin state is scattered.

2.4.1 Neutron Depolarization

The neutron depolarization technique finds its origin in 1941 [24] and it measures the depolarization of a polarized neutron beam after it has been transmitted through a sample. This technique is purely based on the magnetic interaction between the neutron spin and the magnetization \mathbf{B} in the sample which causes the neutron spin to precess:

$$\frac{d\mu_n}{dt} = g_n \mu_N (\mu_n \times \mathbf{B}) \quad (2.23)$$

When the neutron experiences different orientations of \mathbf{B} , its Larmor precession (eq. (2.23)) is changed accordingly and the direction of μ_n is altered when the

neutron leaves the sample. Because the neutron beam is wider than the microscopic dimensions of the sample, individual neutrons experience a different row of consecutive orientations of \mathbf{B} . As a consequence the neutron beam loses its initial polarization $\mathbf{P}_0 = \sum_{\mu_n \uparrow + \mu_n \downarrow} \frac{\mu_n \uparrow - \mu_n \downarrow}{\mu_n \uparrow + \mu_n \downarrow}$ and the depolarization D equals [25]:

$$D = \frac{P}{P_0} = \exp(-c_d \lambda_n^2 \delta d B^2 (1 - \cos^2 \alpha)) \quad (2.24)$$

where the constant $c_d = 2.18 \cdot 10^{29} (1/T^2)$, λ_n the wavelength of the neutrons, d the sample thickness, δ the average magnetic domain size or correlation length and α the angle between \mathbf{P}_0 and \mathbf{B} . Only $B^2(1 - \cos^2 \alpha)$, the square of the component of the magnetization perpendicular to the neutron polarization, contributes to the depolarization. When the experiment is performed on a sample with randomly oriented domains, $\cos^2 \alpha$ equals zero.

2.4.2 Inelastic Neutron Scattering

Inelastic neutron scattering (INS) is characterized by energy transfer between the sample and the neutrons. The neutrons create or annihilate excitations such as phonons or magnons or change their momentum. The characteristic energy gain or energy loss of the neutrons, $\hbar\omega$, is measured. Conservation of momentum and energy dictate that:

$$\hbar\mathbf{q} = \hbar\mathbf{k}' - \hbar\mathbf{k} \quad (2.25)$$

$$\hbar\omega = \frac{\hbar^2}{2m_n} (k^2 - k'^2) \quad (2.26)$$

where $\hbar\mathbf{q}$ and $\hbar\omega$ are the momentum and energy transfer to the sample and \mathbf{k}, \mathbf{k}' are the wavevectors of the incoming and diffracted neutrons. The scattered neutron intensity is related to the response function $S(\mathbf{q}, \omega)$ of the sample [22]:

$$\frac{d^2\sigma}{d\Omega dE'} = \left(\frac{g_n e^2}{m_e c^2}\right)^2 \frac{k'}{k} S(\mathbf{q}, \omega) \quad (2.27)$$

where $\frac{d^2\sigma}{d\Omega dE'}$ is the differential cross section for scattering of neutrons in solid angle $d\Omega$ with energy $E' = (\hbar k')^2 / 2m_n$. For magnetic scattering $S(\mathbf{q}, \omega)$ equals:

$$S(\mathbf{q}, \omega) = \sum_{\Gamma, \Gamma'} p_{\Gamma} \langle \Gamma | \hat{\mathbf{Q}}_{\perp}^+ | \Gamma' \rangle \langle \Gamma' | \hat{\mathbf{Q}}_{\perp} | \Gamma \rangle \delta(\hbar\omega + E_{\Gamma} - E_{\Gamma'}) \quad (2.28)$$

where $\hat{\mathbf{Q}}_{\perp} = \mathbf{q} \times (\hat{\mathbf{Q}} \times \mathbf{q})$ is the magnetic interaction operator and \hat{Q}^+, \hat{Q} resemble creation and annihilation operators. Γ and Γ' are the initial and final state of the sample and p_{Γ} is the probability distribution for initial states. For the study of excitations of the 4f shell these states are determined by the crystal field hamiltonian (eq. (1.13)).

The amplitude of the magnetic scattering by an ion with both spin and orbital angular momentum is proportional to the Fourier transform of its magnetization

density, the formfactor $F(\mathbf{q})$, and for rare earth ions with total angular momentum J , $\hat{\mathbf{Q}} = \frac{1}{2}g_J F(\mathbf{q})\hat{\mathbf{J}}$. The orientation of \mathbf{J} with respect to the scattering vector \mathbf{q} determines how the components of the operator $\hat{\mathbf{J}}$, i.e. J_z, J^+ and J^- , describe the crystal field transitions induced by the neutrons (see eq. (5.4)).

To observe an INS spectrum as simple as possible and to minimize the number of phonons, the lowest temperature in agreement with no spontaneous magnetic order, should be chosen. The reduction of the temperature minimizes the number of occupied initial states (p_r in eq. (2.28)) but magnetic order just increases the number of crystal field levels. If the compound under study shows a relatively high magnetic ordering temperature, a diluted compound is often chosen to suppress the magnetic order. A part of the rare earth atoms then are replaced by the non magnetic Y or La. The symmetry at the R site and the local charge distribution at the $4f$ shell remain unaffected and therefore B_n^m (eq. (1.13)) is believed to be similar in size for the compound and its diluted version.

2.4.3 Neutron Diffraction

Neutron diffraction is a widely used technique to measure magnetic structures since antiferromagnetism was observed in MnO in 1951 [26]. The elastic scattering (only momentum transfer between neutrons and the material under study) of the neutrons measures the structural parameters of the compound. In addition, the magnetic structure is visualized due to the magnetic interaction between the neutron spin and the electronic magnetic moments. Constructive interference of the neutrons by the crystal requires the condition:

$$\Delta \mathbf{k} = \mathbf{k} - \mathbf{k}' = \mathbf{G}_{hkl} \quad (2.29)$$

where \mathbf{G}_{hkl} is a reciprocal lattice vector which is to be associated with a particular set of crystal planes (hkl) in the direct lattice. If 2θ is the angle separating the incident and reflected beam, this equation results in Bragg's law:

$$\lambda_n = 2d_{hkl} \sin \theta \quad (2.30)$$

with d_{hkl} is the distance between the (hkl) planes. Powder samples show all reflections as function of 2θ because of the random orientation of the (hkl) planes. Single crystals allow to measure a map of reciprocal space. Of course this is more time consuming since the sample has to be aligned along its different crystallographic axes and to be rotated to observe a plane in reciprocal space.

For long range periodic magnetic structures (see Fig. 1.2) the magnetic unit cell contains multiple crystallographic unit cells. Such long range magnetic structures are conveniently identified by neutron diffraction because of additional magnetic reflections at low Bragg angle. For example a ferromagnetic arrangement of moments in the hexagonal or tetragonal plane and an antiferromagnetic stacking along the c axis can give an $(0,0,\frac{1}{2})$ reflection.

2.5 Macroscopic techniques

2.5.1 Magnetization

The magnetic moment of the RE 4*f* shell is often anisotropic due to the crystalline electric field (see secs.1.1 and 1.4). The magnetization measured on a single crystal, along different crystallographic directions, will show this anisotropy since the 4*f* shell in the lattice cannot reorient itself as a free ion can. In the presence of \mathbf{B}_{ext} the 4*f* wavefunctions are determined by:

$$\mathcal{H} = \mathcal{H}_{cf} - g_J \mu_B \mathbf{J} \cdot \mathbf{B}_{ext} \quad (2.31)$$

The angle between the quantization axis of the 4*f* shell and \mathbf{B}_{ext} determines which component of \mathbf{J} governs the Zeeman shift δE [1] and lifts the degeneracy of states with $\pm m_J$:

$$\delta E_i = g_J \mu_B \langle \Gamma_i | \mathbf{J} \cdot \mathbf{B}_{ext} | \Gamma_i \rangle \quad (2.32)$$

where Γ_i is the wave function of crystal field level *i*. Bearing in mind that $\Gamma_i = \sum_{m_J} c_{m_J} |J, m_J\rangle$ (see eq. (1.14)), the macroscopic magnetic moment due to rare earth atoms equals:

$$M_{4f} = g_J \mu_B \frac{\sum_{i=1}^{2J+1} \exp(-E_i/k_B T) c_{m_J}^2 \langle J, m_J | \mathbf{J} \cdot \mathbf{B}_{ext} | J, m_J \rangle}{\sum_{i=1}^{2J+1} \exp(-E_i/k_B T)} \quad (2.33)$$

If transition metals are present in the compound they also contribute to the magnetization. The 4*s* electrons of the TM atom are lost due to the metallic bond in the lattice and the magnetic 3*d* shell is located at the outside of the electron cloud. It shows a strong interaction with the crystalline electric field and as a consequence the orbital momentum \mathbf{L} appears to be fixed. The Russel-Saunders coupling scheme cannot be applied and the orbital momentum is generally found to be quenched, i.e. $\langle L_z \rangle = 0$. The magnetic response is mainly determined by the electron spins. This magnetism is most conveniently described by band magnetism, where the magnetic moment is a result of an unequal population of the spin \uparrow and spin \downarrow sub-bands [27].

2.5.2 Specific heat

Under normal experimental conditions, there are three main contributions to the specific heat of rare earth intermetallics. They originate from electrons, magnetic moments and phonons in the lattice. The specific heat of the phonons in a lattice is conveniently described by the model of Debye (1912) and show a T^3 temperature dependence at low temperature [10]. For the electronic contribution the specific heat is proportional to T . The magnetic contribution, c_m , is due to the repopulation of the crystal field levels and is called the Schottky anomaly. It shows a maximum when the temperature is of comparable size as the splitting of the crystal field levels. A convenient trick to separate the magnetic from the

electronic and phonon contributions is to subtract the specific heat of an isotypic stoichiometric compound with a non magnetic rare earth as La, Y or Lu.

If an ion has n energy levels E_i which have degeneracies w_i its internal energy E equals:

$$E = \sum_{i=1}^n \frac{w_i E_i \exp(-E_i/k_B T)}{Z} \quad (2.34)$$

$$Z = \sum_{i=1}^n w_i \exp(-E_i/k_B T) \quad (2.35)$$

where Z is the partition function. In general [11], the specific heat is defined as $c_p = (\frac{\partial H}{\partial T})_P$ with H the enthalpy of the system. For ions located in a solid, this reduces to $c_m = \frac{\partial E}{\partial T}$:

$$c_m = RT \frac{\partial^2}{\partial T^2} (T \ln Z) \quad (2.36)$$

where $R = k_B N_A$ is the gas constant (N_A = Avogadro's number). The repopulation of the energy levels when the temperature increases accounts for a change in entropy $S = k_B \ln(\sum_i (\frac{w_i}{w_0})^{N_A}) = R \ln(\sum_i \frac{w_i}{w_0})$. Note that $\sum_i (\frac{w_i}{w_0})^{N_A}$ is the number of ways the levels of the N_A atoms can be populated [1]. Assuming the entropy is zero at $T = 0$ K, the entropy can be obtained from c_m via:

$$S = \int_0^T \frac{c_m}{T} dT \quad (2.37)$$

For two singlet levels the maximum change in entropy is for example $S = R \ln 2$ and in general the change in entropy is related to the number of crystal field levels and their degeneracy. In addition, the shape of the Schottky anomaly (eq. (2.36)) is a welcome assistance for determining the crystal field level scheme.

* * *

Magnetic nanodomains in TmFeAl[†]

Abstract

The magnetic properties of TmFeAl have been studied using ^{57}Fe and ^{169}Tm Mössbauer spectroscopy, magnetic measurements, neutron depolarization (ND) and neutron diffraction. This compound exhibits a complex magnetic behaviour and its ordered state consists of magnetic nanodomains. At 4 K it contains a Tm moment of $7 \mu_B$ and a distribution of Fe moments with an average of $0.5 \mu_B$. Between 10 and 60 K a distribution in magnetic ordering temperatures is observed. ND displays the growth of small magnetic domains when the temperature decreases towards 4 K. The average domain size is about 2.5 nm at this temperature and the existence of magnetic nanodomains is confirmed by neutron diffraction experiments. The structural disorder of the Fe atoms in the lattice combined with the competing exchange interactions between the different types of atoms and the high anisotropy of the Tm moment gives rise to the observed magnetic behaviour.

[†]Parts of this chapter are published in a modified form in Hyp. Int. 97/98 (1996) 109.

3.1 Introduction

Rare earth (R) transition metal (TM) compounds combine the magnetic properties of two types of atoms which possess magnetic moments of an entirely different nature. Transition metals show itinerant, or delocalized, magnetism, whereas in R atoms the moments are localized. The $4f$ shell, which is the origin of the R magnetism, is non-spherical for the majority of R atoms. As a consequence the R magnetic moment has a preferential orientation which is determined by the crystalline electric field. Therefore, the R compounds show a substantial magnetic anisotropy (sec. 1.4).

The TM compounds on the other hand, show high magnetic ordering temperatures due to the strong exchange interactions caused by the extended TM $3d$ shells. When a TM is combined with a non-magnetic metallic atom such as Al, strong hybridization between the Al valence electrons and the $3d$ electrons occurs which lowers the TM moment.

In a spin glass (SG) frustration of the magnetic moments due to structural disorder and competing positive and negative exchange interactions causes a disordered freezing of the magnetic moments at the spin glass temperature. A classic example is CuMn, where magnetic Mn impurities are randomly imbedded in a non-magnetic matrix of Cu atoms [29].

In this chapter the complex magnetic properties of TmFeAl are presented, which combined both R -TM magnetism with SG-like behaviour. The crystallographic and magnetic properties of TmFeAl were reported earlier by Oesterreicher [30, 31]. The relatively low magnetization values were explained by a partly randomized magnetic moment structure of the rare earth atoms [31]. Furthermore, the high magnetic anisotropy connected with the partially disordered canting of the magnetic moments in TmFeAl is believed to explain the observed intrinsic magnetic hardness [31]. A high anisotropy combined with this magnetic scatter order is assumed to develop extraordinarily thin domain walls. These domain walls are easily pinned at obstacles of atomic dimensions and give rise to an intrinsic hardness.

This study shows that TmFeAl forms extremely small magnetic domains, on average a few nanometres large, in which the Tm moments are aligned ferromagnetically along the c axis. In order to understand the formation of such small magnetic domains also the following compounds were investigated:

1. YFeAl, because Y is a rare earth element with an empty $4f$ shell and has therefore no magnetic moment. As a consequence the magnetism in this compound is purely determined by the Fe atoms.
2. GdFeAl, because the Gd half full $4f$ shell is spherical and therefore it has no preferential orientation in the crystalline electric field of the lattice. This eliminates the influence of the magnetic anisotropy of the R atom due to the crystal field.
3. ErFeAl because the Er $4f$ shell has a similar cigar shape as the Tm $4f$ shell

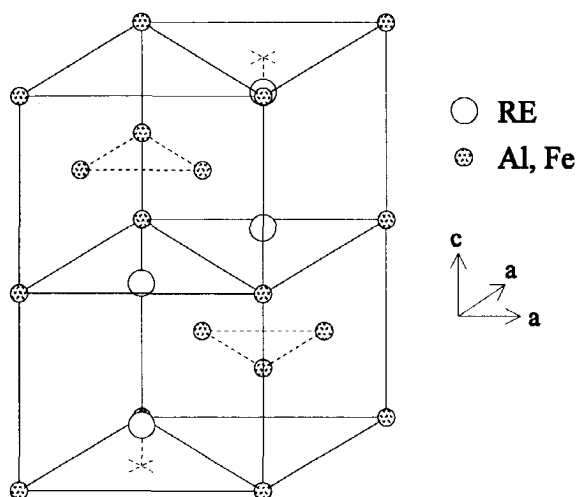


Figure 3.1: The $C14$ hexagonal Laves phase crystal structure of $TmFeAl$. The Tm atoms occupy the RE ($4f$) site and the Fe and Al atoms are randomly distributed over the $2a$ and $6h$ sites.

and therefore it has the same preferential orientation in the crystal field. The strength of the anisotropy, however, is less and this allows us to study the importance of a strong magnetic anisotropy. In general the magnetic anisotropy is related to the second order crystal field term B_2^0 , which is about four times smaller for Er compared to Tm in the same stoichiometric compound.

4. $DyFeAl$, because the Dy $4f$ shell has a discus shape and its preferential magnetic orientation is dissimilar from that of Er and Tm .

3.2 Theoretical aspects

In $RFeAl$, the crystal field at the Tm $4f$ shell (hexagonal point symmetry, see Fig. 3.1) can be described by the hamiltonian (sec. 1.4):

$$\mathcal{H}_{cf} = B_2^0 O_2^0 + B_4^0 O_4^0 + B_6^0 O_6^0 + B_6^8 O_6^8 \quad (3.1)$$

where B_l^m are the crystal field parameters and O_l^m represent Stevens operators. In the magnetically ordered state we include the interaction of the Tm moment with the molecular field H_M and obtain when the Tm moments are aligned along the c axis:

$$\mathcal{H} = \mathcal{H}_{cf} - g_J \mu_B H_M \cdot \langle J_z \rangle \quad (3.2)$$

where g_J is the Landé splitting factor and $\langle J_z \rangle$ the thermal average of the total angular momentum along the direction of H_M .

With Mössbauer spectroscopy the hyperfine field and the quadrupole splitting (QS) are measured at the nuclear site. The hyperfine field is determined by the magnetic moment of the electrons surrounding the nucleus, $gJ\mu_B\langle J_z \rangle$, and the QS is due to the electrostatic interaction between the $4f$ shell and the crystal field (sec. 2.2.2).

3.3 Experimental

The samples YFeAl, TmFeAl, ErFeAl, DyFeAl and GdFeAl were prepared for this study in Amsterdam. These compounds crystallize in the MgZn_2 (C14, hexagonal laves phase) structure and the atoms occupy three non-equivalent sites (Fig. 3.1). The R atoms occupy the $4f$ site and the Al and Fe atoms are randomly distributed over the $2a$ and $6h$ sites [30]. The samples were prepared by arc melting from starting materials of at least 99.9% purity. Afterwards they were vacuum annealed for 7 weeks at 800°C . X-ray diffraction showed that the C14 phase had formed along with a small amount (about 5%) of an impurity phase of unknown origin in the Er- and TmFeAl samples.

Neutron activation analysis was used to check the composition of the Er and Tm samples. $\text{Er}_1\text{Fe}_{0.98}\text{Al}_{0.96}$ was found for the Er sample and a Fe:Al ratio of 1:1.02 was found for TmFeAl. The quantity of Tm could not be measured because of self absorption of its low energy gamma rays (8.4 keV). In addition to this, transmission electron microscopy pictures were taken of the TmFeAl and ErFeAl samples to determine the microstructure. Whereas in ErFeAl the microstructure showed no peculiarities, the TmFeAl pictures showed a Moiré pattern. These patterns consists of dark light contrast with a period of 1-3 nm. They possibly indicate anti-phase boundaries. The sample consists of grains ranging from 200 nm to $4\text{ }\mu\text{m}$ and also subgrains were found (200-1000 nm) separated by low angle boundaries. Composition differences were found between small and large grains, either due to a secondary phase or due to deviations from the nominal composition.

The ^{57}Fe Mössbauer spectra were measured at various temperatures by means of a constant-acceleration-type spectrometer using an ^{57}Co source in a rhodium foil. The ^{169}Tm Mössbauer spectra were obtained at various temperatures using a acceleration-type spectrometer in sinusoidal mode, the measured spectra being plotted on a linear scale. An absolute velocity calibration was obtained with a laser Michelson interferometer. The ^{169}Tm Mössbauer effect was measured using 8.4 keV gamma rays emitted by ^{169}Er obtained after neutron irradiation of $^{168}\text{ErAl}_3$. The principles of Mössbauer spectroscopy are discussed in sec. 2.2.

The neutron depolarization measurements have been performed at the IRI at the SP beamline and the neutron diffraction measurements have been performed at the HMI institute (Berlin) at the E6 beamline. For more details about these techniques see secs. 2.4.1 and 2.4.3. All the measurements presented in this chapter were performed on powder samples.

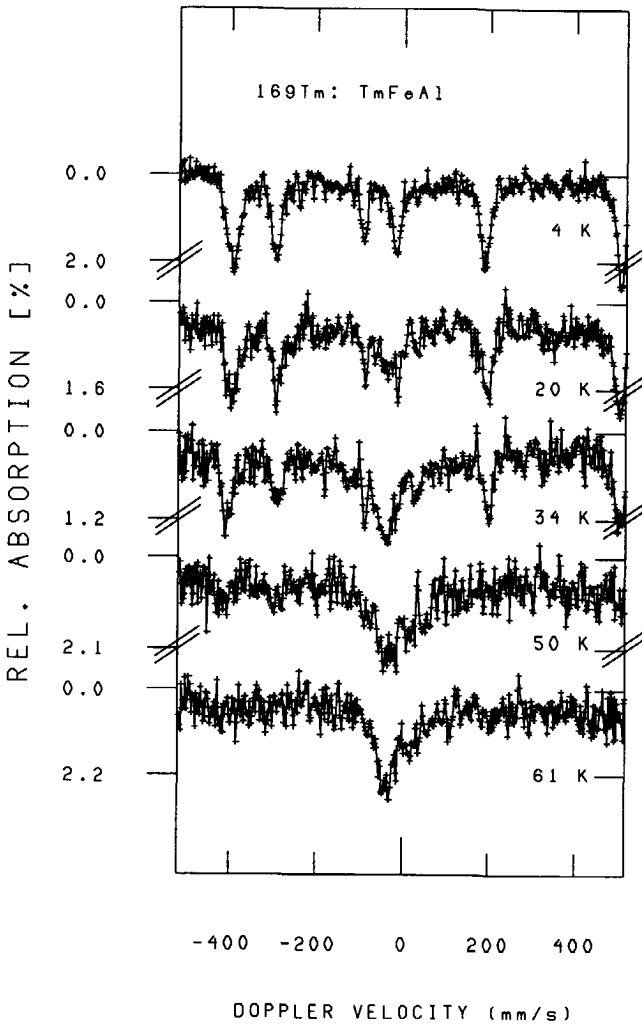


Figure 3.2: Some ^{169}Tm Mössbauer spectra of TmFeAl at various temperatures showing a mixed phase of magnetically ordered and paramagnetic regions. Note that the Tm magnetic moment remains the same during the transition from full magnetic order (4 K) towards full paramagnetism (61 K).

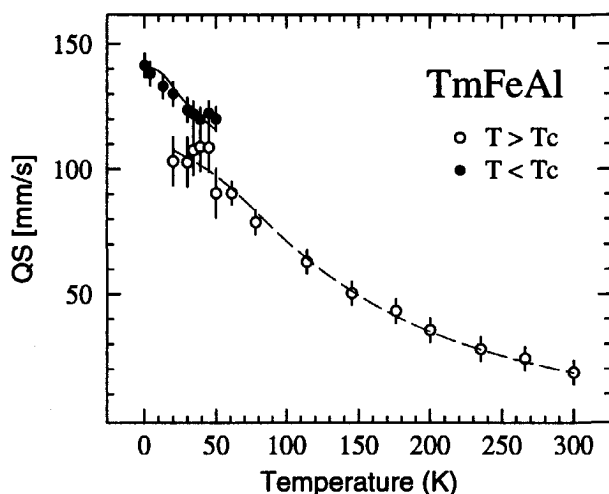


Figure 3.3: Quadrupole splitting QS as observed by ^{169}Tm Mössbauer spectroscopy as a function of temperature. The filled circles correspond to the QS of the sextuplet and the empty circles to the QS of the doublet. The solid and dotted line correspond to a fit with eq. (2.6) of which the first includes the molecular field. This fit gives as possible set of crystal field parameters: $B_2^0 = -3.1$ K, $B_4^0 = 5 \cdot 10^{-3}$ K, $B_6^0 = 8 \cdot 10^{-5}$ K, $B_6^6 = 2 \cdot 10^{-4}$ K, $QS^{\text{latt}} = -16.7$ mm/s and $H_M = 37$ T. These deduced parameters are not unique but the large negative value of B_2^0 and QS^{latt} is strong evidence of a large magnetic anisotropy.

3.4 Results

3.4.1 Mössbauer spectroscopy

TmFeAl

Some of the measured ^{169}Tm Mössbauer spectra are shown in Fig. 3.2. Below ~ 10 K the spectrum shows a sextuplet, characteristic of a magnetically ordered Tm sublattice. The energy splitting between the two outer Mössbauer absorption peaks measures a hyperfine field at the nucleus of 710(10) T. The free ion value, which would originate from a Tm moment of $7 \mu_B$ equals 720 T. Hence, the Tm moment in TmFeAl equals $7 \mu_B$ within the experimental limit.

Above ~ 60 K the ^{169}Tm Mössbauer spectra show an asymmetric doublet, indicating that the Tm sublattice is paramagnetic. The asymmetry is due to relaxation of the Tm magnetic moments.

In the temperature region from ~ 10 to ~ 60 K the spectra show both a sextuplet as well as a doublet. This indicates a phase mixture of ordered magnetism and paramagnetism in the compound. The magnetically ordered portion of the Tm sublattice, which is related to the absorption area of the sextuplet, decreases with increasing temperature, while the paramagnetic portion, the relative absorp-

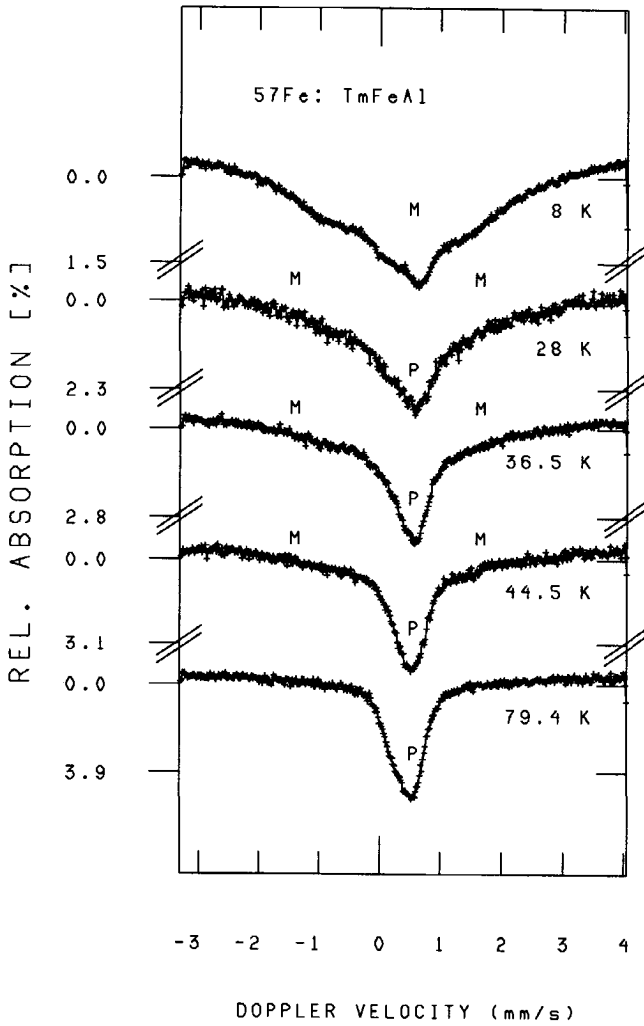


Figure 3.4: ^{57}Fe Mössbauer spectra of TmFeAl at various temperatures showing an Fe moment distribution and the occurrence of ordered magnetism (M) and paramagnetism (P).

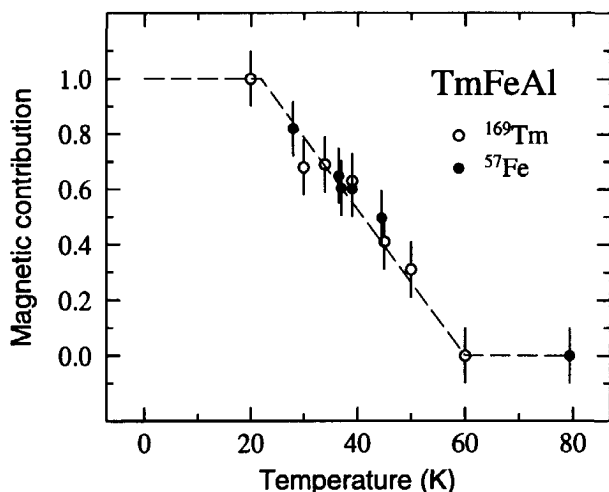


Figure 3.5: Magnetic portion of the Tm (empty circles) and Fe (filled circles) sublattices in TmFeAl as a function of temperature as determined by Mössbauer spectroscopy. The dashed line is a guide to the eye.

tion area of the doublet, increases. The magnitude of the hyperfine field remains constant up to 60 K. Also the width of the absorption peaks remains unbroadened which indicates that no magnetic relaxation is present. This suggests a crystal field ground level of which the magnetic moment equals the saturation value and of which the relaxation trajectory via excited crystal field levels is not accessible at 60 K and below.

The quadrupole splitting deduced from the sextuplet as well as from the doublet are plotted in Fig. 3.3. The solid and dotted line in Fig. 3.3 are the result of a fit with eq. (2.6) where eq. (3.2) has been used to calculate the crystal field levels of the Tm $4f$ electrons. The crystal field parameters are listed in the caption of Fig. 3.3 and, although this set of parameters is not unique, it shows a large negative value of B_2^0 which corresponds to a substantial magnetic c axis anisotropy. Therefore the Tm moments are aligned either parallel or antiparallel to the c axis. This is confirmed by the sharp ^{169}Tm Mössbauer lines that indicate that all the Tm moments have the same orientation with respect to the main axis of the electric field gradient, which is determined by the crystal symmetry.

Some of the measured ^{57}Fe Mössbauer spectra are shown in Fig. 3.4. At low temperature the spectra reveal a distribution of Fe moments with an average hyperfine field of 7.7 T. Using the ratio between hyperfine field and corresponding magnetic moment of $14.8 \text{ T}/\mu_B$ for Fe compounds [32] an average moment size of $0.52 \mu_B$ has been calculated. Above $\sim 60 \text{ K}$ a quadrupole doublet is observed. In the temperature region in between, the spectra show a mixture of magnetically ordered (M) and paramagnetic (P) moments, just as observed in the ^{169}Tm Mössbauer spectra.

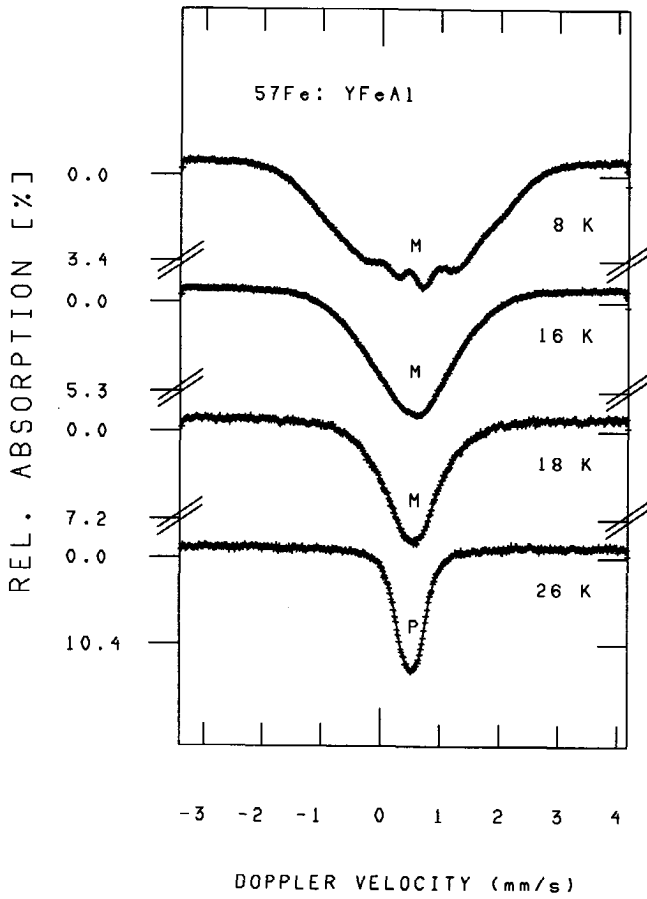


Figure 3.6: ^{57}Fe Mössbauer spectra of YFeAl at various temperatures indicating Fe moment distribution and a second order phase transition at 23(2) K.

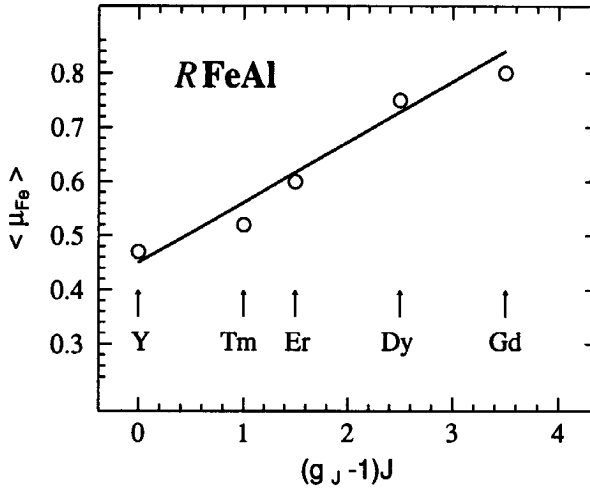


Figure 3.7: De Gennes scaling observed in the average magnetic moment of iron in $RFeAl$. The exchange interaction between the rare earth atom and the iron is proportional to $(g_J - 1)J$.

The magnetically ordered portions of the Tm and Fe sublattices as determined from the relative magnetic absorption area, are plotted in Fig. 3.5. The percentage of magnetic order is identical in both sublattices. We have assumed that below 10 K all Fe moments are magnetically ordered but since the absorption is strong at the centre in this spectrum, the possibility of paramagnetic Fe moments at 10 K cannot be excluded. On the other hand, because of the broad distribution in magnetic Fe moment size, the central intensity may be caused by small Fe moments ($\sim 0.1\mu_B$).

The explicit coexistence of magnetism and paramagnetism during such an extended temperature region is remarkable. It indicates a first order magnetic ordering process (sec. 1.5) as observed in for example $ErCo_2$ [33] combined with an elongation of the ordering trajectory due to structural disorder of the Fe and Al atoms in the lattice.

YFeAl, ErFeAl, DyFeAl and GdFeAl

Some ^{57}Fe Mössbauer spectra of YFeAl are shown in Fig. 3.6. At 8 K a distribution of hyperfine fields is observed with an average of 6.9 T, which corresponds to an Fe moment of $0.47\mu_B$ [32]. In contrast with the ^{57}Fe Mössbauer spectra of TmFeAl, the average moment decreases when the ordering temperature of 23(2) K is approached from below. This is characteristic of a second order transition.

^{57}Fe Mössbauer measurements of GdFeAl show also a second order magnetic transition with $T_C = 268(2)$ K. At low temperature a magnetic hyperfine field distribution is observed with an average of 11.9 T which corresponds to an average Fe moment size of $0.80\mu_B$. The Fe moment as well as T_C are enhanced compared to TmFeAl and YFeAl because of the stronger 3d-4f exchange interaction. Also

ErFeAl and DyFeAl show a distribution in hyperfine fields at the Fe nuclei at 8 K with an average of 8.8 and 11.1 T which corresponds to 0.60 and 0.75 μ_B . An overview of the magnetic properties of the RFeAl series is given in table 3.1.

Table 3.1: Parameters deduced from Mössbauer and magnetization experiments combined with the theoretical values $\mu_R^{\text{eff}} = g_J(J(J+1))^{\frac{1}{2}}$ and $\mu_R = g_J J$.

	Experimental					Theory	
	T_C (K)	$\langle\mu_{\text{Fe}}\rangle$	μ_R	$M(T=5 \text{ K})$ ($\mu_B/f.u.$)	μ^{eff}	μ_R^{eff}	μ_R
YFeAl	23(3)	0.47	-	-	-	0	0
TmFeAl	distr.	0.52	7	1.75	7.2	7.57	7
ErFeAl	55(2)	0.60	-	4.5	10.2	9.59	9
DyFeAl	151(2)	0.75	-	6.1	10.1	10.6	10
GdFeAl	268(2)	0.80	-	-	-	7.94	7

3.4.2 Magnetization

Fig. 3.8 shows the magnetization of TmFeAl measured with a SQUID magnetometer. First the sample was cooled in zero field followed by a measurement of the magnetization in an applied field of 0.05 T (curve 1). Secondly, the sample was cooled in the field of 0.05 T (curve 2) and warmed again (curve 3). The bump observed in curve 1 around 20 K is reminiscent of a spin glass like freezing temperature. The monotonous increase in the magnetization when the temperature is lowered (curve 2) corresponds to the monotonous increase in the magnetic portion of TmFeAl as observed with Mössbauer spectroscopy (Fig. 3.5). Curve 1 and 3 coincide above ~ 65 K, thereby confirming the onset of complete paramagnetism in the compound as determined with Mössbauer spectroscopy.

High field magnetization measurements were performed in Amsterdam on a fixed as well as a free TmFeAl powder sample and on free powders of YFeAl and GdFeAl. With an optical microscope the powder particle size is estimated 1-2 μm , thus no magnetic domain walls are expected inside a powder particle. The free powder particle will align themselves in a external magnetic field and produce a maximum magnetization whereas the fixed powder particles, frozen in alcohol at 4 K, will behave like a polycrystalline material. The results of this study are shown in Fig. 3.9.

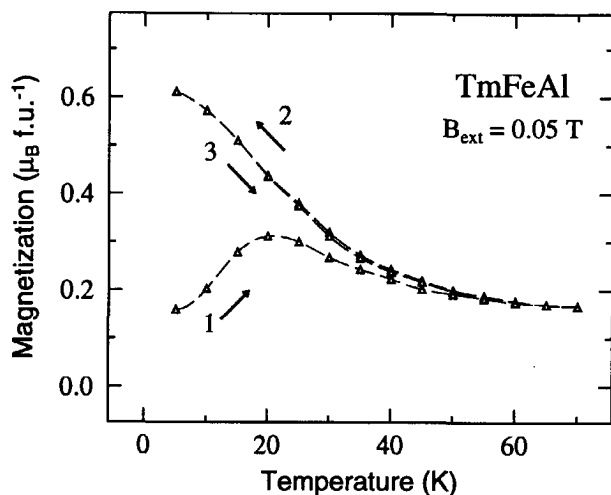


Figure 3.8: Magnetization of TmFeAl as a function of temperature measured after ZFC (curve 1) and FC (curve 2 and 3). The monotonous increase of curve 2 and the maximum at 20 K of curve 1 are characteristics of the complex behaviour of TmFeAl (see text).

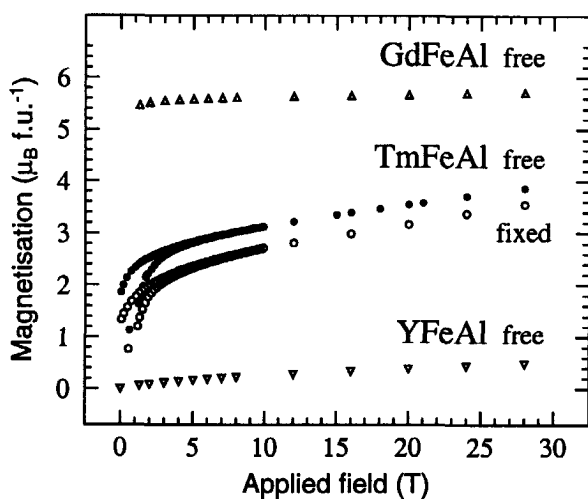


Figure 3.9: Field dependence of the magnetization of YFeAl, GdFeAl (both free powders) and TmFeAl (fixed and free powder). Note the square root like dependence of YFeAl and the small difference between the fixed and free TmFeAl powder. For details see text.

GdFeAl shows a saturation moment of $5.8 \mu_B$. Since the Gd moment is not influenced by the crystal field a Gd moment of $7 \mu_B$ is expected. The antiferromagnetic coupling between the Gd and the Fe sublattice reduces the total moment per unit cell and $\langle \mu_{Fe} \rangle = 1.2 \mu_B$ is estimated. This value is larger than the average moment measured with ^{57}Fe Mössbauer spectroscopy.

The magnetization curve of YFeAl resembles a square root like function. The magnetization continues to increase up to a field of 28 T and the slope of the curve continues to decrease. Such a magnetization curve is characteristic of spin glass behaviour. It shows that magnetic frustration is present in the Fe sublattice. The magnetization curve of the free as well as the fixed TmFeAl powder shows a linear increase between 10 and 30 T. This feature is characteristic of TmFeAl and will be discussed in sec. 3.5.

In addition to these high field experiments, the magnetization of RFeAl ($R = \text{Tm, Er and Dy}$) was measured in applied fields up to 2 T. For the latter two compounds a tendency towards saturation was observed and the deduced magnetization at zero field is listed in table 3.1. The measurements on TmFeAl confirmed the magnetization curve of Fig. 3.9. The susceptibilities deduced from these measurements are analysed with eq. (1.8) and the results (T_C and the effective moment) are listed in table 3.1. The susceptibility of DyFeAl follows the Curie-Weiss law but the magnetization of TmFeAl as well as ErFeAl is larger than expected near T_C .

3.4.3 Neutron Depolarization

Neutron depolarization provides the opportunity to study the nucleation and growth of magnetic domains. ND measurements were performed on TmFeAl as well as ErFeAl in zero field and with an applied field of 0.05 T parallel to the polarization vector of the neutron beam. In Fig. 3.10 and 3.11 the quantity $\Sigma = -\ln D/(c \cdot d) = B_s^2(1 - m^2)f_M\delta$ is plotted (see eq. (2.24)). Σ is related to the magnetic domain size δ , the percentage magnetically ordered material f_M and the magnetization B_s . The open dots in Fig. 3.10 are measured in zero field (ZFC(cooling) + ZFW(warming)) on a powder of TmFeAl. An increase in Σ is observed when the temperature decreases until saturation was obtained below ~ 8 K. The difference between the cooling curve ZFC and warming curve ZFW clearly indicates hysteresis in the domain formation. We checked that thermal equilibrium of the sample was obtained during the measurements. The black dots measured with applied field (FC + FW) show a similar behaviour as the zero field curve, but the Σ values are much larger.

The ND measurements were performed on a powder with random crystallographic and magnetic orientations and therefore $\cos^2 \alpha$ equals zero in the ZF measurement. At 4 K TmFeAl is fully magnetically ordered and $f_M = 1$. Assuming ferromagnetic order of the Tm moments we derive an average magnetic cluster size of about 2.5 nm, which is much smaller than the crystalline dimensions.

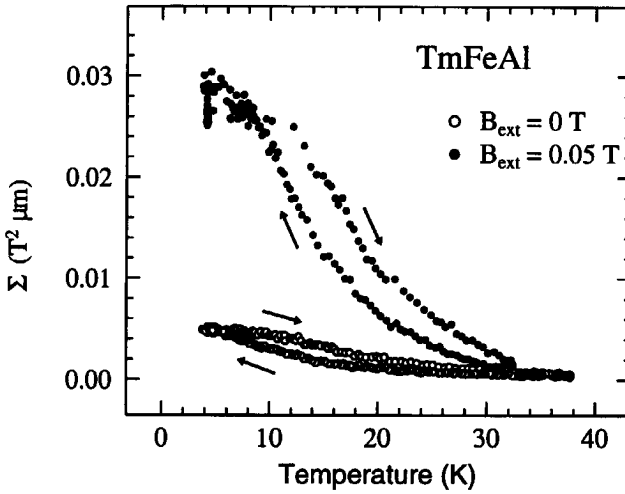


Figure 3.10: Σ of TmFeAl as deduced from neutron depolarization experiments in an external field (F) and in zero field (ZF). Σ is proportional to B_s^2 , the magnetic domain size δ and the magnetic fraction f_M of the material. From the ZF measurement at 4 K an average magnetic domain size of about 2.5 nm is deduced.

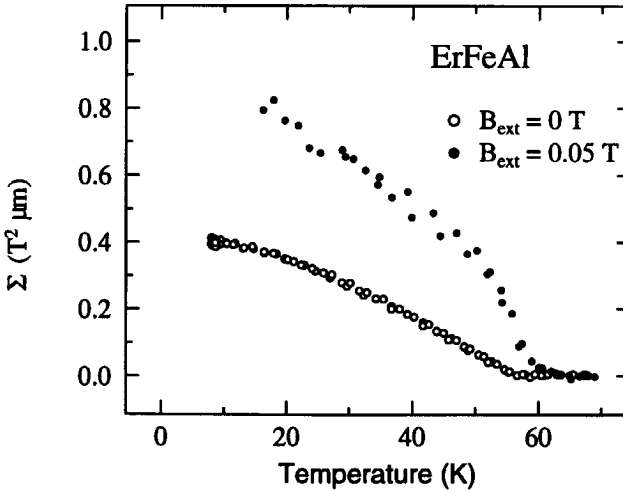


Figure 3.11: $\Sigma = B_s^2(1 - \cos^2 \alpha)f_M \delta$ as deduced from neutron depolarization experiments on ErFeAl. The cooling and warming curves coincide and show that no magnetic hysteresis is present.

Table 3.2: Calculated diffraction angle 2θ and relative intensity I of the diffraction peaks due to a ferromagnetic alignment of the Tm magnetic moments in TmFeAl. Lattice parameters $a = 5.339 \text{ \AA}$ and $c = 8.636 \text{ \AA}$ and the Tm coordinates $(\frac{1}{3}, \frac{2}{3}, 0.053)$ are deduced from the nuclear Bragg peaks at 100 K and used in the calculation. $\lambda_n = 2.426 \text{ \AA}$.

hkl	2θ (°)	I (a.u.)	hkl	2θ (°)	I (a.u.)	hkl	2θ (°)	I (a.u.)
1 0 0	30.418	11.1	0 0 3	49.843	0.0	2 0 0	63.294	2.1
0 0 2	32.630	0.0	1 1 0	54.052	12.0	1 1 2	64.582	7.0
1 0 1	34.624	4.2	1 1 1	56.798	0.0	2 0 1	65.798	1.1
1 0 2	45.209	2.6	1 0 3	59.520	2.9			

In Fig. 3.11 the result of ND measurements on a ErFeAl powder are plotted. Comparison of Fig. 3.10 and Fig. 3.11 clearly shows a difference in the formation of magnetic order. ErFeAl shows a clear onset of magnetic order at the ordering temperature and the growth in Σ resembles the increase in magnetic domain size combined with the increase in magnetic moment size. The influence of the applied magnetic field is small if compared with TmFeAl. Assuming ferromagnetic order of the Er moments we calculate a magnetic domain size at 4 K in zero field of $\sim 0.4 \mu\text{m}$.

3.4.4 Neutron Diffraction

A neutron diffraction study is performed at the HMI on a TmFeAl and an ErFeAl powder. It allows us to determine the magnetic structure and orientation of the Tm and Er moments. The results are shown in Figs. 3.12 and 3.13. The spectra were obtained at various temperatures and a spectrum measured in the paramagnetic state was subtracted in order to see the magnetic reflections. Because of the small Fe moments we cannot observe any magnetic Fe reflections and only observe the reflections due to the magnetic Tm and Er sublattice.

First we will discuss the TmFeAl results. Comparison of the magnetic diffraction spectrum measured at 1.6 K with the calculated values listed in table 3.2 shows that the magnetic order corresponds to a ferromagnetic sublattice with the Tm moments aligned along the positive c direction. The diffraction peaks are indexed in Fig. 3.12.

At low angle ($2\theta < 20^\circ$) a magnetic oscillation is observed, indicative of short range ferromagnetic order [34]. This is consistent with the small average domain size observed with neutron depolarization. The magnetic Bragg peak indicated by ? appears at a diffraction angle lower than the (100) reflection and, if not related to magnetic ordering of a secondary phase in the sample, should be of anti-ferromagnetic origin. It corresponds to a distance of 5.73 \AA in the crystal lattice

and could possibly be related to a superstructure of the magnetic nanodomains. Note that the magnetic Bragg peaks are strongly broadened due to the small magnetic domain size.

In ErFeAl also a ferromagnetic arrangement of the Er moments along the positive c axis is observed (Fig. 3.13). The intensity of the magnetic Bragg peaks follows a Brillouin curve as a function of temperature. These reflections disappear above ~ 55 K indicating the magnetic ordering temperature. In contrast to TmFeAl, no short range order is observed in this compound.

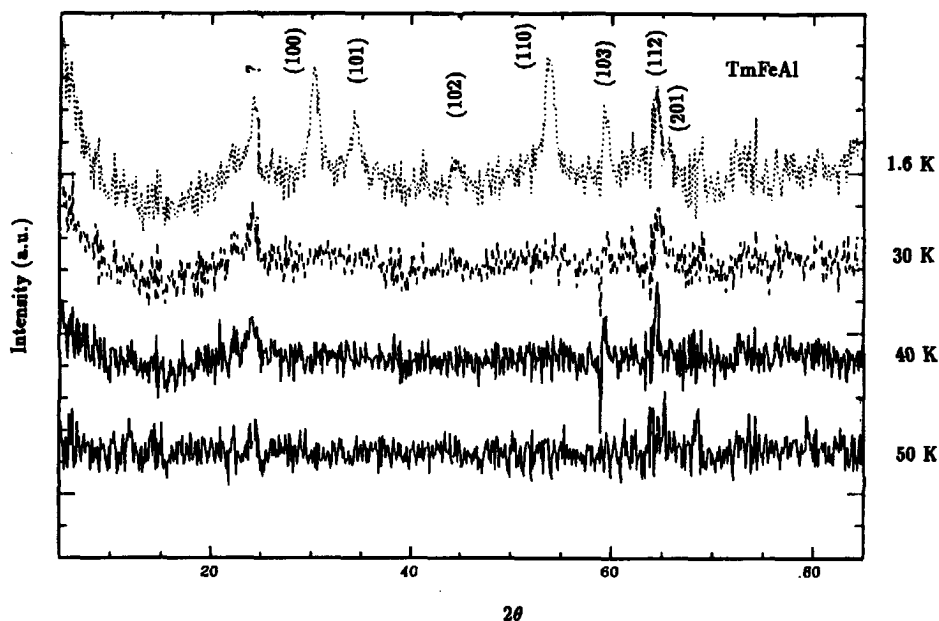


Figure 3.12: Four neutron diffraction spectra of TmFeAl recorded at various temperatures. The Bragg reflections due to the crystal structure (spectrum at 100 K) were subtracted so only the magnetic reflections are shown. The spectrum at 1.6 K corresponds to a ferromagnetic alignment of the Tm moments along the c axis. The magnetic oscillation at low angle is indicative of short range magnetic order.

3.5 Discussion

The Mössbauer measurements on TmFeAl show a mixed phase with a distribution of ordering temperatures. Such a behaviour was reported before in the concentrated spin glass $\text{Co}_{60}\text{Ga}_{40}$ [35]. It is shown that this spin glass has a different freezing behaviour compared to the more diluted spin glass systems as CuMn . A continuous spectrum of freezing temperatures is observed in contrast with one

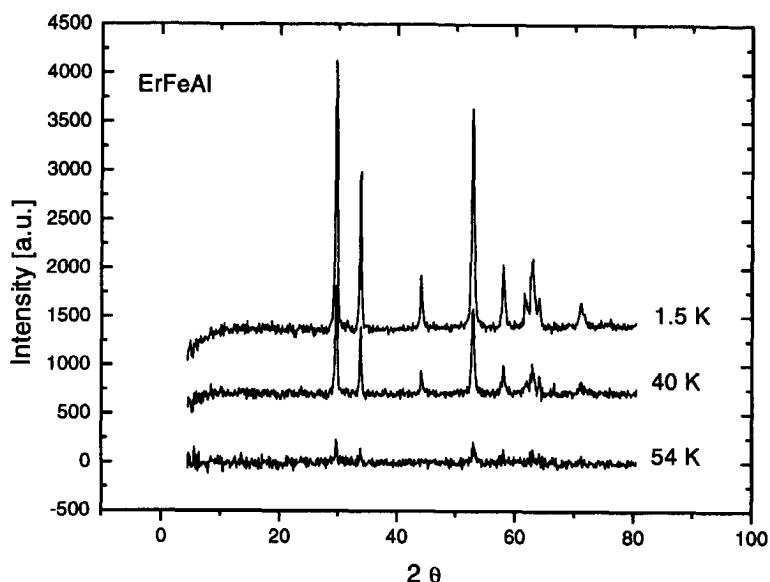


Figure 3.13: Magnetic diffraction peaks measured on *ErFeAl*. The Bragg reflections correspond to a ferromagnetic alignment of the *Er* magnetic moments (compare table. 3.2). The magnetic ordering temperature is determined at $T_C = 55$ K.

freezing temperature as observed in systems as *CuMn*. In *Co₆₀Ga₄₀* the excess of Co atoms, that are statistically distributed on Ga sites in the Pauli paramagnetic CoGa system, are responsible for the spin glass behaviour [35]. *TmFeAl* resembles an even more concentrated spin glass like system, since the concentration of magnetic moments is much higher. The magnetization curve of *TmFeAl* measured after zero field cooling (see Fig. 3.8) indicates a spin glass like temperature around 20 K. In addition ^{57}Fe Mössbauer spectroscopy shows that at 4 K the Fe moments are frozen with a distribution in moment sizes. These aspects are all characteristic for a spin glass like behaviour of the Fe sublattice.

The statistical occupation of the Fe and Al atoms over the two available crystallographic sites implies the occurrence of concentration fluctuations so that it is more appropriate to consider *TmFeAl* as a cluster glass rather than a spin glass. Inspection of the magnetic ordering temperatures of *RAI₂* compounds listed in ref. [36] shows that these are fairly low (e.g. 4.2 K for *TmAl₂* [37]) suggesting that magnetic ordering in *TmFeAl* is mainly due to Fe rich regions. Upon cooling these comparatively Fe-rich clusters will give rise to magnetic ordering, but do so at different temperatures and with different Fe moments, depending of the Fe concentration. No magnetic order is present in the matrix material surrounding the clusters, although this matrix material will gradually be consumed by growth of the magnetic clusters and formation of new magnetic clusters when the temperature is decreased. This behaviour is in agreement with the observations

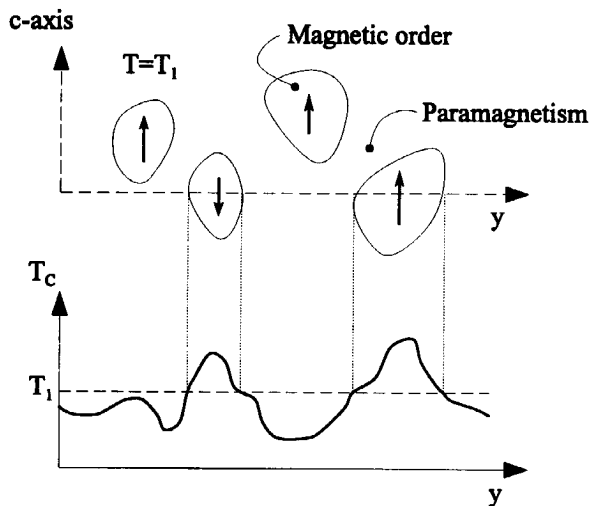


Figure 3.14: Illustration of magnetic nanodomains (top) and their relation to the distribution in magnetic ordering temperature T_C (bottom). The y axis represents an arbitrary direction in the basal plane of the TmFeAl crystal lattice.

made by Mössbauer spectroscopy. It accounts for the observation of a distribution of Fe hyperfine fields and it also accounts for the presence of a magnetic and non-magnetic component in the spectra, the latter gradually disappearing with decreasing temperature.

From the ^{169}Tm Mössbauer spectra combined with the neutron diffraction spectra it was derived that the ordered Tm moments are of equal size and are ferromagnetically oriented along the crystallographic c direction. Because the magnetic clusters are more or less magnetically decoupled, there will be a statistical distribution of the Tm moment directions in the different clusters in either the positive or negative c direction upon magnetic ordering. Therefore there will be no Tm contribution to the magnetization when the sample is cooled without the presence of an external field. If the Tm-Fe moment coupling is strictly ferrimagnetic within each cluster one would expect that there is also no net contribution of the Fe moments to the magnetization.

It can be derived from the field dependence of the magnetization of TmFeAl shown in Fig. 3.9 that the anisotropy field is larger than the highest field considered in this investigation, because no tendency towards saturation is reached. This is confirmed by the estimated value of the crystal field parameter $B_2^0 \sim -3.1$ K which corresponds to an anisotropy field of about 100 T. From the discussion given above it follows that the cluster moment directions will be, even in small single crystals, equally distributed in the positive and negative c direction. This may explain the relatively low difference in magnetic behaviour observed between the fixed and free powder particles in Fig. 3.9. At the same time it may explain why

the moment observed in the highest field strength is substantially lower than the moment expected on basis of the Mössbauer data ($7 \mu_B - 0.5 \mu_B$).

The formation and growth of the magnetic clusters in TmFeAl is also in line with the neutron depolarization experiments. The observed increase in Σ (Fig. 3.10) is much stronger than expected from the increase of f_M only, therefore confirming an increase in the average cluster size when the temperature decreases. A cluster size in the order of 2.5 nm has been derived from the ND data at the lowest temperature. Therefore it is appropriate to speak of a nanodomain structure (see also Fig. 3.14). Furthermore, short range magnetic order is observed in the neutron diffraction spectra, thereby confirming the presence of magnetic nanodomains.

The small dimensions of the up and down clusters possibly resemble long range antiferromagnetic order if the clusters are of equal size. Although we were not able to identify the magnetic Bragg peak observed at low angle (Fig. 3.12), it could be related to such a superstructure of the nanodomains. Transmission electron microscopy pictures have revealed a Moiré pattern in TmFeAl. This possibly indicates the existence of anti-phase boundaries in the crystals of the material, which can be a source of small magnetic domains. This is confirmed by the period of the diffuse scattering at low 2θ [34] which suggests domains in the order of 10 Å.

Fig. 3.10 shows that an external field gives rise to an increase in the cluster size. Upon cooling, the clusters freeze with their Tm moment in the most favourable c direction as determined by the field they experience. Due to demagnetisation fields of the early clusters, this field is not always parallel to the applied field. Therefore clusters with opposite magnetization directions are still formed. More than half of cluster moments however favour the c direction as determined by the external field. Consequently there will be a substantial net contribution to the magnetization, explaining the difference between the curves 1 and 2 in Fig. 3.8.

YFeAl, ErFeAl, DyFeAl and GdFeAl all show a broad distribution in Fe magnetic moment. This random Fe moment size is related to the statistical occupation of Fe atoms in the crystal lattice. The average size of the Fe moments in this series of compounds is determined by the Fe exchange interaction as well as the Fe- R exchange which is proportional to $J(g_J - 1)$ of the R 4 f shell [38]. The latter interaction causes $\langle \mu_{Fe} \rangle$ to increase going from YFeAl to GdFeAl (table 3.1 and Fig. 3.7).

The magnetization curve of YFeAl (Fig. 3.9) is reminiscent of spin glass behaviour, confirming the frustration of the Fe moments. In GdFeAl and DyFeAl, the strong exchange interaction between the rare earth atoms (for example $T_C^{GdAl_2} = 175$ K and $T_C^{DyAl_2} = 65$ K) overcomes the frustration of the Fe sublattice and no signatures of spin glass behaviour are observed in the magnetization data (Fig. 3.9). Neutron diffraction and depolarization measurements on ErFeAl also show no signatures of magnetic frustration. The contrast with the TmFeAl results clearly indicate that the magnetic nanodomain structure is not present in ErFeAl. Apparently its rare earth exchange interaction is high enough ($T_C^{ErAl_2} \sim 18$ K) and its anisotropy low enough to prevent the formation of small magnetic domains.

The small dimensions of the magnetic domains observed in TmFeAl imply the existence of narrow Bloch walls. The width of magnetic domain walls between the clusters is a result of a competition between the Tm exchange strength and the magnetic anisotropy. With the use of the estimated anisotropy (sec. 3.4.1) a Tm exchange strength J_{TmTm} of a few K is deduced [39] which is not unrealistic if compared with $T_C^{\text{TmAl}_2} = 4.2$ K. In this estimation a moment rotation of 180° between neighbouring atoms is assumed and therefore the formation of magnetic nanodomains is realistic if we consider the magnetic boundary formation.

3.6 Conclusion

In this chapter the formation of magnetic nanodomains in TmFeAl is presented. This unique behaviour originates from the following characteristics of the compound. The structural disorder of the Al and Fe atoms in the lattice causes the Fe sublattice to behave like a spin glass. The exchange interactions between the different types of magnetic atoms are influenced by the structural disorder of the Fe sublattice, leading to a distribution in magnetic ordering temperatures for clusters of different Fe concentration in TmFeAl. The high magnetic anisotropy contributes to the magnetic behaviour by forcing the Tm moments along their preferential direction in the crystalline electric field. Magnetic clusters with the Tm moments aligned along the positive or negative c directions form and grow in the crystallites of TmFeAl when the temperature decreases from 60 to 10 K. Due to the high magnetic anisotropy of these clusters then remain aligned along their initial orientation. The size of these magnetic nanodomains on average about 2.5 nm at 4 K.

* *
* *

Two types of magnetism in the magnetic superconductor $\text{TmNi}_2\text{B}_2\text{C}$ related to the degree of carbon site occupancy[†]

Abstract

A combined ^{169}Tm Mössbauer spectroscopy and $\mu^+\text{SR}$ study is presented on two polycrystalline samples of $\text{TmNi}_2\text{B}_2\text{C}$. The first experimental technique shows the coexistence of two types of Tm $4f$ magnetism at 0.3 K, one related to a magnetic Tm moment of $4.3(1) \mu_B$ and the other to a small Tm moment of $\sim 0.1 \mu_B$. This second type of magnetism is suggested to be caused by carbon vacancies present in $\text{TmNi}_2\text{B}_2\text{C}$. These C vacancies locally modify the crystalline electric field and therefore the Tm $4f$ magnetism. Since these vacancies are ideal cavities in which muons can reside, it is suggested that $\mu^+\text{SR}$ only probes this $\sim 0.1 \mu_B$ magnetism.

[†] Published in a modified form in Phys. Rev. B 54 (1996) 14963,
Phys. Rev. B 57 (1998) 10320 and J. Magn. Magn. Mat. 177-181 (1998) 555.

4.1 Introduction

The discovery of the quaternary rare earth nickel boron carbides $R\text{Ni}_2\text{B}_2\text{C}$ in 1993 started an intensive study of their combined magnetic and superconducting properties. In some of these compounds ($R = \text{Tm}, \text{Er}, \text{Ho}$ and Dy) these studies reveal the coexistence of superconductivity and magnetism. As the strength of the exchange interaction between R atoms increases (De Gennes scaling) the transition to the superconducting state occurs at lower temperatures, due to the increase of Cooper pair breaking [40]. Because of this variation in magnetic strength, the boron carbides are an ideal system to study the interplay between magnetism and superconductivity and they are therefore the subject of continuing scientific interest.

The magnetically ordered state of $R\text{Ni}_2\text{B}_2\text{C}$ shows a variety of magnetic structures [41]. The non-superconducting compounds $\text{PrNi}_2\text{B}_2\text{C}$ and $\text{NdNi}_2\text{B}_2\text{C}$ show a commensurate antiferromagnetic structure with an in plane easy magnetization axis whereas $\text{GdNi}_2\text{B}_2\text{C}$ and $\text{TbNi}_2\text{B}_2\text{C}$ show a sine modulated incommensurate antiferromagnetic structure with propagation vector $\delta \sim (0.55, 0, 0)$. Similar magnetic structures are observed in the superconducting rare earth boroncarbides. $\text{DyNi}_2\text{B}_2\text{C}$ ($T_N \sim 10.6$ K; $T_C \sim 6$ K) and the low temperature phase of $\text{HoNi}_2\text{B}_2\text{C}$ ($T \leq 5$ K) show a commensurate antiferromagnetic structure, but $\text{ErNi}_2\text{B}_2\text{C}$ and the reentrant phase of $\text{HoNi}_2\text{B}_2\text{C}$ ($5 \leq T \leq 6.3$ K) show a sine modulated structure with δ similar to $\text{GdNi}_2\text{B}_2\text{C}$.

In contrast to all these planar magnets, an easy c -axis is observed in $\text{TmNi}_2\text{B}_2\text{C}$. For this compound it is shown that $T_N = 1.52(2)$ K [42] and $T_C = 10.8$ K [43]. Recent neutron diffraction studies revealed an incommensurate antiferromagnetic structure with $\delta = (0.093, 0.093, 0)$ i.e. a modulation in the $[110]$ direction with a clear onset at 1.5 K [41, 44]. The sine modulated magnetic moments with a maximum of $3.78 \mu_B$ are pointing along the c -axis and the modulation becomes square shaped at lower temperature.

$\mu^+\text{SR}$ on $\text{HoNi}_2\text{B}_2\text{C}$ and $\text{ErNi}_2\text{B}_2\text{C}$ [45] shows a muon precession frequency of the size expected for the magnetic Ho and Er moments ($\sim 10.4 \mu_B$ [46] and $8.4 \mu_B$ [47]) and confirms the magnetic ordering temperatures of ~ 8 K and 6.8 K, respectively. Surprisingly, $\mu^+\text{SR}$ measurements on $\text{TmNi}_2\text{B}_2\text{C}$ [45, 48, 49] contradict the magnetic behaviour of the Tm atoms as measured by neutron techniques. They reveal that a spontaneous internal field is present up to ~ 30 K which is far above T_N . This spontaneous field saturates below ~ 2.5 K and shows an inexplicable $1/T$ dependence above this temperature. If this internal field is caused by only the Tm moments, the saturation value corresponds to a Tm moment of $\sim 0.1 \mu_B$ (the muon precession frequency equals about 1.8 MHz). Different studies [41, 50] exclude the possibility of small Ni moments in $R\text{Ni}_2\text{B}_2\text{C}$ so it is believed that the magnetism observed by $\mu^+\text{SR}$ is caused by the rare earth atoms only.

Because of the very large difference in magnetic Tm moment between the different experimental techniques, we performed a ^{169}Tm Mössbauer study [51] of two samples. The first sample was prepared in Amsterdam and the results of this Mössbauer study are published in ref. [51]. The second sample of $\text{TmNi}_2\text{B}_2\text{C}$

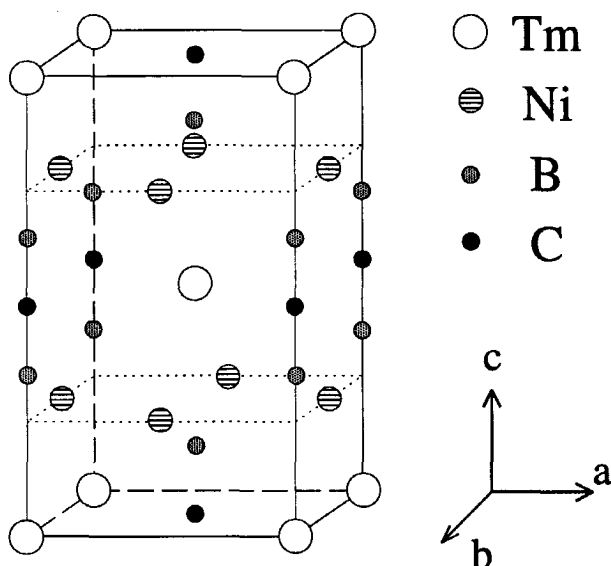


Figure 4.1: Crystal structure of $\text{TmNi}_2\text{B}_2\text{C}$. Note that each Tm atom is surrounded by four carbon atoms in the ab plane.

was used for inelastic neutron scattering (INS) measurements by Gasser [52] and prepared at PSI. From these INS measurements crystal field parameters (CFP) were deduced which describe not only the INS data but also magnetization [43], specific heat [42] and neutron diffraction data [41, 44]. These CFP predicted a Tm $4f$ magnetic moment of $\sim 4.3 \mu_B$ in the magnetically ordered state.

In this chapter we report on the differences between the two samples and on the implications of these differences on the Tm $4f$ magnetism. Also an explanation will be given for the large discrepancy between the results obtained by neutron techniques and $\mu^+\text{SR}$.

4.2 Theoretical aspects

$\text{RNi}_2\text{B}_2\text{C}$ crystallizes in a body-centered tetragonal structure that consists of R -C planes separated by Ni_2B_2 layers stacked along the c -axis (Fig. 4.1). While the magnetism is caused by the R atoms, the superconductivity is believed to be concentrated in the Ni_2B_2 layers [53]. The behaviour of the asymmetric $4f$ shell of the R atoms in these compounds is strongly influenced by crystal field effects [54]. The crystal field Hamiltonian \mathcal{H}_{cf} for the tetragonal point symmetry ($I4/mmm$)

of the R $4f$ shell can be written as:

$$\mathcal{H}_{cf} = B_2^0 O_2^0 + B_4^0 O_4^0 + B_4^4 O_4^4 + B_6^0 O_6^0 + B_6^4 O_6^4 \quad (4.1)$$

where B_l^m are the crystal field parameters and O_l^m represent Stevens operators. This Hamiltonian describes the splitting of the rare earth ground multiplet J and therefore the magnetism of the $4f$ shell.

^{169}Tm Mössbauer spectroscopy uses the ^{169}Tm nucleus as a probe and its quadrupole splitting QS is very sensitive to the behaviour of the electronic $4f$ shell of the Tm atom (sec. 2.2.2). Since the properties of the conduction electrons are screened by the core electrons, ^{169}Tm Mössbauer spectroscopy is not sensitive to the superconducting properties.

4.3 Experimental details

Both polycrystalline samples of $\text{TmNi}_2\text{B}_2\text{C}$ which were studied by ^{169}Tm Mössbauer-technique, were prepared by arc melting from starting materials of at least 99.9% purity. The initial ratio between the starting materials was different for the two samples. Whereas for the sample from Amsterdam [51] a ratio of $\text{Tm:Ni:B:C} = 1.1:2:2:1$ was used, the sample from PSI [52] was prepared in a ratio of $1:2:2:1.1$. Extra Tm was added to the first mixture because Tm vaporizes more quickly than the other constituents in the melt. In this chapter we refer to these samples as sample A and sample B, respectively. X-ray diffraction on both samples showed the desired crystal structure combined with a second unknown phase. This second phase was different for the two samples and less than 10 %. Magnetization measurements showed the superconducting transition at $T_C = 10.3(3)$ K and $T_C = 10.8(3)$ K for the samples A and B, respectively.

The ^{169}Tm Mössbauer spectra were recorded on an acceleration-type spectrometer in sinusoidal mode, the measured spectra being plotted on a linear scale. An absolute velocity calibration was obtained with a laser Michelson interferometer. The ^{169}Tm Mössbauer effect was measured using 8.4 keV gamma rays emitted by ^{169}Er obtained after neutron irradiation of $^{168}\text{ErAl}_3$ grains in an Al matrix.

The Muon Relaxation Spectroscopy measurement was performed at the GPS beamline at PSI. Specific heat measurements were performed at the Leiden University.

4.4 Results

4.4.1 $\text{TmNi}_2\text{B}_2\text{C}$, sample A

The ^{169}Tm Mössbauer spectra of sample A (see sec. 4.3) were recorded at various temperatures between 0.3 K and 773 K. Because the Ni atoms partially absorb the 8.4 keV gamma rays (K absorption edge), the ^{169}Tm Mössbauer effect is rather small and therefore long measurement times were needed for reasonable spectra

statistics. All spectra showed a quadrupole doublet, including the spectra recorded at low temperatures, and were analysed on the basis of a single spectrum.

Two spectra, measured at $T = 0.45$ K and 8 K, are plotted in Fig. 4.2. At first sight there are no clear signs of magnetic ordering in the 0.45 K spectrum. However, a precise analysis of this low temperature spectrum shows that the left Mössbauer absorption line is slightly broadened (Fig. 4.2) which is most likely due to a small magnetic moment of the Tm atoms. In that case the hyperfine interaction is a small perturbation on the electric quadrupole splitting. We are able to deduce from the 0.45 K spectrum a Tm moment of approximately $0.1(1) \mu_B$. Fig. 4.3 shows the deduced quadrupole splitting ($QS \propto V_{zz}$) as a function of temperature. We observe a clear change in QS at $1.1(1)$ K. A transition from a paramagnetic phase to a magnetically ordered phase is usually accompanied by a change in QS because the exchange interaction influences the relative position of the energy levels of the crystal field split $2J+1$ manifold of the $4f$ shell. The clear change at 1.1 K is therefore indicative of magnetic ordering. Fig. 4.4 shows the specific heat measured in zero field and with an external field of 1 T. The transition to the superconducting state is observed at 9.75 K and a second transition is visible at 1.17 K. The shape of this transition peak is altered in an external field which confirms that the transition is of magnetic origin.

The Mössbauer spectra measured above the transition at 1.1 K show line broadening (Fig. 4.2) which decreases with increasing temperature and persists up to about 40 K. At present, its origin is not yet obvious. It might correspond to the phenomenon seen in μ^+ SR studies [45, 48, 49] where the μ^+ precession frequency persists up to high temperatures compared with T_N . Magnetic relaxation of the Tm moments above T_N could explain the Mössbauer spectra as well as the μ^+ SR data if the relaxation is sufficiently slow ($> 10^{-6}$ s). In that case the Tm moments appear to be static to the muon and a precession signal will be observed.

Using the high temperature approximation of eq. (2.6) we deduce $QS^{\text{latt}} = -22(4)$ mm/s from Fig. 4.3. With eq. (2.7) V_{zz}^{latt} is calculated to be equal to $10(2) \cdot 10^{21}$ V/m² which is in good agreement with $V_{zz}^{\text{latt}} = 11.9 \cdot 10^{21}$ V/m² obtained with ^{155}Gd Mössbauer spectroscopy on $\text{GdNi}_2\text{B}_2\text{C}$ [55] where $V_{zz}^{4f} = 0$ because the the Gd $4f$ shell is spherical. With the use of eq. (2.8) $B_2^0 = -2.8(5)$ K is calculated. The sign of B_2^0 corresponds to a c -axis anisotropy as is also observed by susceptibility and μ^+ SR measurements [43, 45, 48, 49]. Its strength, however, is twice as large as the value derived from the susceptibility measurements. The temperature dependence of $QS(T)$ of sample A indicates that B_2^0 is negative but smaller than $B_2^0 = -2.8(5)$ K. Most likely, the empirical relation eq. (2.8) with $c = 185$, is different in this compound due to the carbon atoms which are interstitially present in the crystal nearby the Tm atoms. Therefore, we believe that the empirical constant c equals approximately 400 in $\text{TmNi}_2\text{B}_2\text{C}$. A more precise value of c can be calculated if B_2^0 is determined.

The small magnetic moment of Tm along the c -axis as well as the maximum in the temperature dependence of QS at 140 K (Fig. 4.3) both indicate that crystal field effects play an important role in $\text{TmNi}_2\text{B}_2\text{C}$. Strong crystal field effects are also observed in $\text{ErNi}_2\text{B}_2\text{C}$, where they cause a change in magnetic anisotropy at

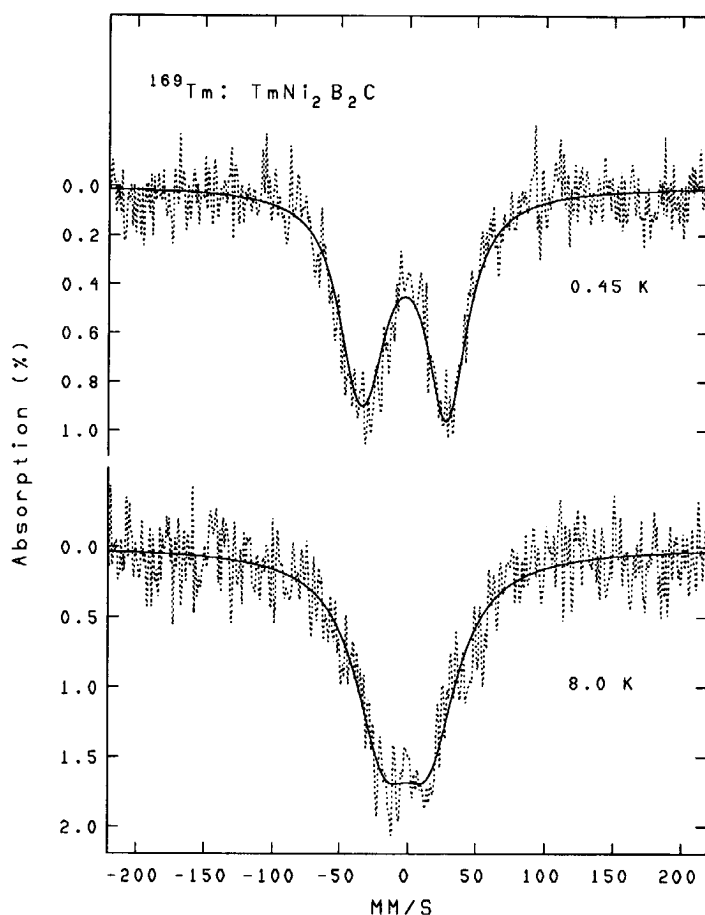


Figure 4.2: Two spectra recorded on sample A below (0.45 K) and above (8 K) the transition temperature of $\sim 1.1(1)$ K. The 0.45 K spectrum shows that the left Mössbauer peak is slightly broadened which is indicative of a small Tm moment in the order of $0.1(1) \mu_B$. Note that the QS at 0.45 K is clearly larger than at 8 K. Above 1.1 K a broadening of the quadrupole doublet lines is observed.

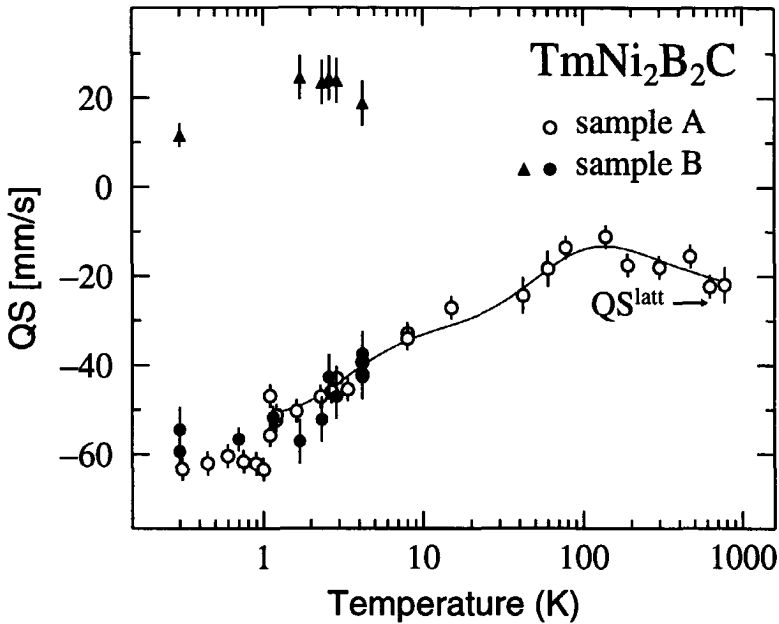


Figure 4.3: The quadrupole splitting QS as observed by ^{169}Tm Mössbauer spectroscopy in sample A (empty dots) and sample B (filled symbols). The filled triangles are deduced from the subspectrum which shows a moment of $4.3 \mu_B$ at 0.3 K and the filled dots are deduced from the other subspectrum. Note that the filled and empty dots are identical to each other within the experimental error. The solid curve is obtained from the crystal field parameters $B_2^0 = -1.16$ K, $B_4^0 = 4.61 \cdot 10^{-3}$ K, $B_4^4 = 0.173$ K, $B_6^0 = -1.44 \cdot 10^{-5}$ K and $B_6^4 = 1.11 \cdot 10^{-3}$ K but can be considered only as a guide to the eye (see text).

~ 150 K [54]. Although a negative B_2^0 is responsible for c -axis anisotropy at high temperature in $\text{ErNi}_2\text{B}_2\text{C}$, a basal plane anisotropy is observed at low temperature due to higher order crystal field parameters.

4.4.2 $\text{TmNi}_2\text{B}_2\text{C}$, sample B

The spectra of sample B were recorded between 0.3 K and 8 K. The spectrum recorded at 0.3 K as well as the spectrum of sample A at that temperature are plotted in Fig. 4.5. The spectra show that Tm magnetism is different in the two samples. Sample A shows a single quadrupole doublet at 0.3 K and in contrast to this, the spectrum of sample B measured at 0.3 K shows two different subspectra. The sextuplet corresponds to a magnetically ordered Tm $4f$ moment of $4.3(1) \mu_B$ and in the centre of the spectrum a doublet is observed. Since only a small amount of contamination is observed by X-rays we believe these two subspectra

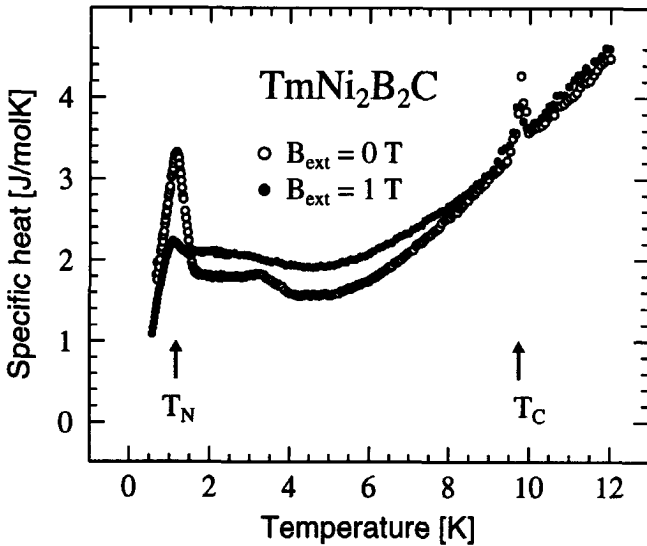


Figure 4.4: Specific heat of sample A measured in zero field and with an external field of 1 T. Note the superconducting transition at 9.75 K and the Néel temperature at ~ 1.2 K. The anomaly at 3 K is discussed in the text.

both originate from the same crystallographic structure, $\text{TmNi}_2\text{B}_2\text{C}$. Apparently, two types of Tm 4f magnetism coexist in sample B.

At 0.7 K the sextuplet shows strongly broadened absorption lines which may be a result of the sine modulated magnetic structure as measured by neutron diffraction [41, 44]. At 1.7 K the sextuplet is replaced by a second quadrupole doublet in the Mössbauer-spectrum, indicating the paramagnetic state. The quadrupole splitting of the two doublets above the magnetic ordering temperature differ substantially from each other, which made it possible to separate the two different contributions in the ^{169}Tm Mössbauer spectrum of sample B. This analysis showed that the QS of the first doublet subspectrum (present in sample B also below 1.7 K) is identical to the QS of sample A within the experimental error between 0.3 and 4 K (see Fig. 4.3). For higher temperatures it was not possible to separate the two contributions in sample B. Because the quadrupole splitting is sensitive to the crystal field levels of the Tm 4f shell this does suggest that the doublet subspectrum of sample B originates from the same type of Tm 4f magnetism as in sample A. Fig. 4.6b shows a spectrum of sample B measured at 0.3 K with a velocity scale of 200 mm/s. The sextuplet is subtracted from the spectrum in order to observe the central doublet in more detail. An asymmetric broadening is visible which resembles the spectrum of sample A (Fig. 4.6a) and confirms the hypothesis that the doublets in sample A and B have the same origin.

For the analysis of the sextuplet we used two different approaches. In Fig. 4.5b we used the moment modulation of the magnetic SDW as determined by Lynn [41] from neutron diffraction experiments at 0.65 K. To calculate the magnetic moment modulation the wave vectors q , $3q$ and $5q$ were used. Because this modulation was

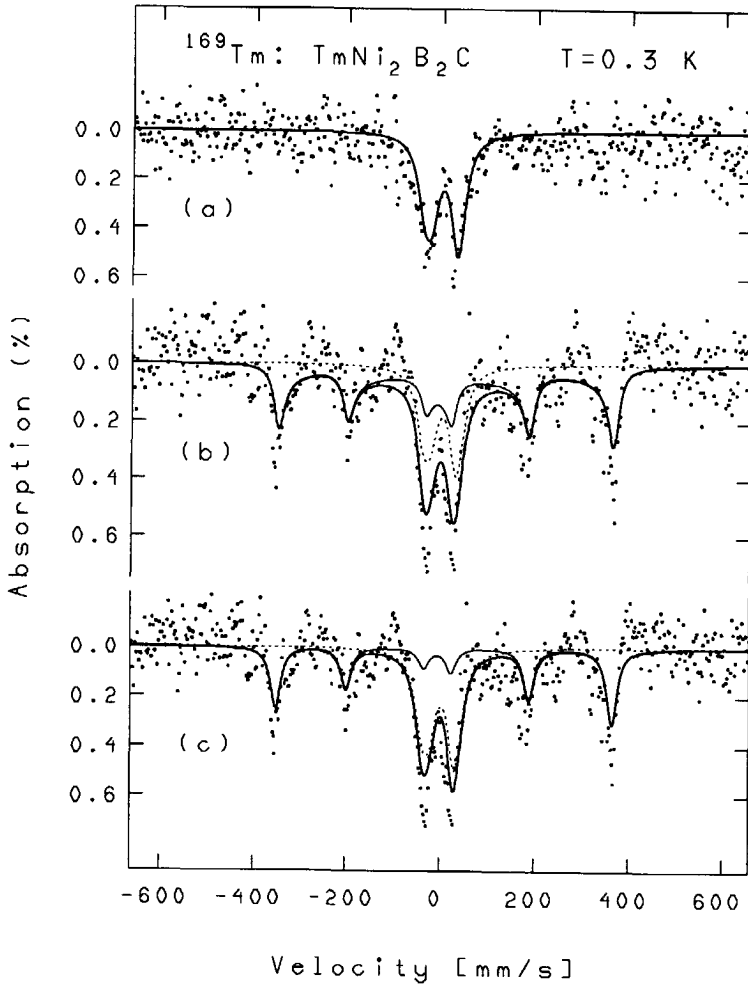


Figure 4.5: ^{169}Tm Mössbauer spectrum of sample A ($\text{Tm}_{1.1}\text{Ni}_2\text{B}_2\text{C}$, shown in (a)) and sample B ($\text{TmNi}_2\text{B}_2\text{C}_{1.1}$, shown in (b) as well as (c)) measured at 0.3 K. Whereas sample A shows a single quadrupole doublet, sample B shows two sub-spectra, a doublet and a sextuplet. Two spectra analysis of sample B are shown, (b) and (c). In (b) the sextuplet is analysed with the SDW modulation determined by Lynn ($q + 3q + 5q$) and a maximum Tm 4f moment of $4.3 \mu_B$. The sextuplet in (c) corresponds to a square shaped magnetic Tm moment modulation. Note that the unequal population of the nuclear ground state with Zeeman splitting is taken into account. The doublets are shown in more detail in Fig. 4.6.

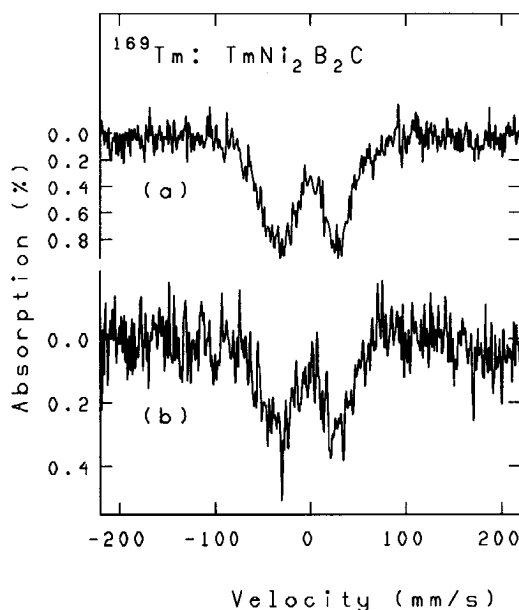


Figure 4.6: ^{169}Tm Mössbauer spectrum of sample A ($\text{Tm}_{1.1}\text{Ni}_2\text{B}_2\text{C}$) and sample B ($\text{TmNi}_2\text{B}_2\text{C}_{1.1}$) measured with a velocity scale of 200 mm/s at 0.3 K. These spectra contain the central part of the spectra presented in Fig. 4.5. The sextuplet is subtracted from the spectrum of sample B. Note that the asymmetric broadened doublet of sample A is also observed in sample B. Since the doublet of sample A is interpreted as a small Tm moment this suggests that small Tm moments of $0.1 \mu_B$ are also present in sample B.

measured at 0.65 K the possibility exists that the magnetic modulation is more square shaped at 0.3 K. Therefore we also calculated the Mössbauer spectrum corresponding to a square shaped Tm moment modulation. The sextuplet of sample B is equally well described by either one of these analyses. The percentage of Tm atoms which take part in the modulated magnetic structure varies from $\sim \frac{2}{3}$ in the first analysis to $\sim \frac{1}{2}$ in the last analysis.

A $\mu^+\text{SR}$ measurement has been performed at 0.3 K on the polycrystalline sample B and is plotted in Fig. 4.7. This spectrum is analysed with

$$A(t) = A \left[\frac{1}{3} \exp(-\lambda_1 t) + \frac{2}{3} \exp(-\lambda_2 t) \cos(2\pi\nu_\mu t) \right] \quad (4.2)$$

where A is the asymmetry, λ the relaxation rate and ν_μ the muon precession frequency. The first and second term correspond to the relaxation of the muon polarization parallel and perpendicular to the internal field. In the case of a polycrystalline sample the ratio of the amplitudes is 1:2. As is shown in Fig. 4.7 a single, strongly damped, muon precession signal of ~ 1.8 MHz is observed just

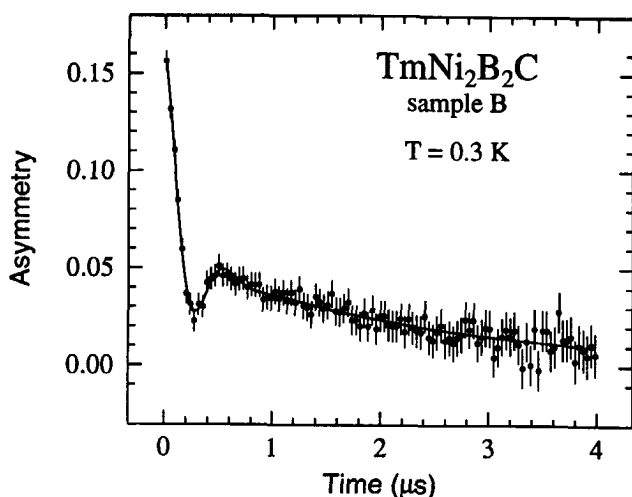


Figure 4.7: Zero field μ SR spectrum measured at 0.3 K in the polycrystalline sample B. A single, strongly damped, muon precession frequency is observed of 1.8 MHz which corresponds to a Tm moment of $\sim 0.1 \mu_B$.

as in previous μ^+ SR measurements performed on other samples of $\text{TmNi}_2\text{B}_2\text{C}$ [45, 48, 49].

4.5 Discussion

Since a different quantity of carbon was used for the preparation of the two samples, differences in the amount of C interstitials can be responsible for the difference in magnetic behaviour of the Tm 4f shell. Although carbon stabilizes the $\text{RNi}_2\text{B}_2\text{C}$ compounds, the exact amount of carbon necessary for a stable $\text{TmNi}_2\text{B}_2\text{C}_x$ is unknown. A study of $\text{DyNi}_2\text{B}_2\text{C}_x$ [56] shows that superconductivity is not influenced drastically for $0.9 < x < 1.1$. Since X-ray diffraction is not very sensitive to the amount of C in the sample, a deficiency in carbon ($x < 1$) is possible. Because a lower C : Tm ratio is used for the preparation of sample A there will be more carbon vacancies in this sample. We therefore believe that the $4.3 \mu_B$ moment of $\text{TmNi}_2\text{B}_2\text{C}$ corresponds to Tm atoms surrounded by four carbon atoms as is expected for the $\text{RNi}_2\text{B}_2\text{C}$ structure. The $0.1 \mu_B$ however, may correspond to Tm atoms situated near a C vacancy. This C vacancy reduces the symmetry at the Tm site and modifies the crystal field and therefore the Tm 4f magnetism. Also the hybridization of the Tm valence electron states with the C valence electrons will decrease when C vacancies are present. This reduction in hybridization is expected to decrease the absolute value of B_2^0 .

In μ^+ SR the muons localize interstitially in the lattice where they probe the magnetism of their host. It is shown that in CeRu_2Si_2 [57], a compound with the same tetragonal structure but without interstitial carbon, the muons localize

at the $(\frac{1}{2}, \frac{1}{2}, 0)$ site, i.e. the site of the carbon atoms in $\text{RNi}_2\text{B}_2\text{C}$. Therefore C vacancies may be an ideal cavity for muons to reside in. Assuming that all samples of $\text{TmNi}_2\text{B}_2\text{C}$ which were used for $\mu^+\text{SR}$ experiments contain some amount of C vacancies, this explains why $\mu^+\text{SR}$ spectroscopy only measures $\mu_{\text{Tm}} \sim 0.1 \mu_B$. Based on these arguments there is a fair chance that the muons localize in the C vacancies. For this reason they only probe Tm atoms which are situated in the modified crystal field of the $0.1 \mu_B$ magnetism. The exact muon location site can be verified by $\mu^+\text{SR}$ Knight Shift measurements (see sec. 6.2) on a single crystal of $\text{TmNi}_2\text{B}_2\text{C}$.

Since sample B is polycrystalline this experiment could not be done but another way to check this muon location hypothesis, is standard $\mu^+\text{SR}$ spectroscopy. Since the ^{169}Tm Mössbauer spectrum at 0.3 K of sample B established a magnetic moment of $4.3 \mu_B$ for approximately half of the Tm atoms, this moment should be observed by $\mu^+\text{SR}$ if the muons localize at the $(0,0,0.20)$ site as expected from Knight Shift measurements on $\text{HoNi}_2\text{B}_2\text{C}$ [58]. In that case about half of the muons localize near a $4.3 \mu_B$ Tm moment and half the muons are expected to show a muon precession signal which corresponds to this moment size. For the $(0,0,0.20)$ site near Tm atoms with moments of $4.3 \mu_B$, the corresponding muon frequency is equal to 64.5 MHz. In contrast to this, a single precession signal of 1.8 MHz is observed in sample B (Fig. 4.7). Although the internal field probed by $\mu^+\text{SR}$ depends on the muon site and on the magnetic size and structure of the rare earth atoms, it is remarkable that the observed muon frequency in $\text{TmNi}_2\text{B}_2\text{C}$ is about 40 times smaller than in Er- and $\text{HoNi}_2\text{B}_2\text{C}$ [45, 48, 49]. In fact, calculations based on dipole coupling show that the observed muon frequency of ~ 1.8 MHz is only compatible with muon site locations at $(0,0,0.20)$ or $(\frac{1}{2}, \frac{1}{2}, 0)$ near Tm moments of $\sim 0.1 \mu_B$. The localization of the muon near a small Tm moment is therefore a tempting explanation for the observed muon precession signal in Fig. 4.7. Except for ^{169}Tm Mössbauer spectroscopy there are no other experimental results to support this small moment. On the other hand, the amount of C vacancies will depend strongly on the sample preparation and small quantities of $\sim 0.1 \mu_B$ Tm moments magnetism are easily disregarded.

In a ^{166}Er Mössbauer spectroscopy study on $\text{ErNi}_2\text{B}_2\text{C}$ [47] a 'secondary phase' of $\sim 10\%$ is observed which the authors attribute to the $\text{ErNi}_2\text{B}_2\text{C}$ itself. This also could be due to the presence of vacancies in the sample. From the μSR point of view described above, this is possible because the Er moment of the 'secondary phase' is similar to the moment of the Kramers ion Er in the rest of the sample. Therefore it may pass unnoticed if the muons probe the Er magnetism at sites distorted by vacancies.

Analysis of Fig. 4.3 with eqs.(4.1) and (2.6) indicates the crystal field ground state level of the $0.1 \mu_B$ magnetism most likely equals the singlet $a| - 4 \rangle + b|0 \rangle + a| + 4 \rangle$. If this ground state is in energy only a few Kelvin separated from a magnetic crystal field level, say a doublet with the eigenfunctions $c| \pm 5 \rangle + d| \pm 1 \rangle + e| \mp 3 \rangle$, this explains the small magnetic moment of Tm in the magnetically ordered state, which is then induced by mixing some of the magnetic crystal field state into the non magnetic ground state. Furthermore, it

explains the μ^+ SR depolarization data of Le et al. [45], where an enhanced μ^+ SR depolarization rate is observed when a small external field (up to 0.7 T) is applied. The applied field will influence the relative position of the magnetic crystal field level(s) and will enlarge the Tm moment. This, in turn, will increase the muon depolarization rate.

In contrast to this, the $4.3 \mu_B$ phase shows the $c|\pm 5\rangle + d|\pm 1\rangle + e|\mp 3\rangle$ as crystal field ground state and the singlet as an excited state. The carbon vacancy alters the crystal field in such a way that the ground state is different for the two types of magnetism. Cho et al. [59] observe that $\text{TmNi}_2\text{B}_2\text{C}$ is as effective in magnetic pair breaking as $\text{GdNi}_2\text{B}_2\text{C}$ and they conclude that the crystal field levels in $\text{TmNi}_2\text{B}_2\text{C}$ are close together so they all contribute to the pair breaking process. This explains why a small change in crystal field can induce a different crystal field level to be the ground state.

Comparing the ^{169}Tm Mössbauer spectra of the two investigated samples of $\text{TmNi}_2\text{B}_2\text{C}$, a possible signature of the $4.3 \mu_B$ magnetism is visible in sample A. The spectrum measured at 8 K in Fig. 4.2 shows broadened absorption lines and is discussed in terms of relaxation in sec. 4.4.1. Another interpretation is, however, that the spectrum consists of two subspectra with different quadrupole splittings as it is seen in the spectra of sample B at that temperature. In this case the broad quadrupole doublet is related to the $4.3 \mu_B$ magnetism. In the magnetically ordered state the corresponding sextuplet is not visible, either because the abundance is not large enough or because the magnetic moment modulation is not square shaped but shows a more sinusoidal like form.

The specific heat measurement of sample A shows a Schottky like anomaly at 3 K. If this anomaly is indeed due to population of the crystal field levels of the $4f$ shell it cannot originate from the complete sample because its entropy is too low. Although the anomaly might also be related to the secondary phase observed with X-rays it might also be a possible signature of two different $\text{TmNi}_2\text{B}_2\text{C}$ types of magnetism.

Until now, attempts to describe our measurements with two sets of CFP were not successful. The search for these parameters is complicated by the unknown abundance of the two sets as well as by the change of symmetry at the $4f$ shell due to the missing carbon atoms in the lattice. This latter phenomena is expected to introduce extra terms in \mathcal{H}_{cf} (see eq. (4.1)).

A study of high quality samples, where the carbon content is systematically varied and measured by neutron diffraction, is suggested to find the key of the influence of the carbon site occupancy and a μ^+ SR Knight shift study on a single crystal of $\text{TmNi}_2\text{B}_2\text{C}$ is suggested to determine the muon location site.

4.6 Conclusion

Two samples of $\text{TmNi}_2\text{B}_2\text{C}$ are studied by ^{169}Tm Mössbauer spectroscopy and two magnetic moment sizes are observed, one of $\sim 0.1 \mu_B$, the other $\sim 4.3 \mu_B$. This difference is discussed in terms of carbon site occupancy and gives a plausible

explanation for the large difference in Tm $4f$ magnetic moment observed by neutron techniques ($\mu_{\text{Tm}} \sim 4.3 \mu_B$) and $\mu^+\text{SR}$ ($\mu_{\text{Tm}} \sim 0.1 \mu_B$). Carbon vacancies in $\text{TmNi}_2\text{B}_2\text{C}$ modify the crystal field at the Tm $4f$ shell near these vacancies and this results in a small magnetic Tm moment of $\sim 0.1 \mu_B$. Tm atoms surrounded by four C atoms as it is expected for $\text{TmNi}_2\text{B}_2\text{C}$ show a magnetic moment of $4.3(1) \mu_B$. Although ^{169}Tm Mössbauer spectra unambiguously show the coexistence of these two types of magnetism in the examined sample B, $\mu^+\text{SR}$ only probes the $\sim 0.1 \mu_B$ because the muons localize in the C vacancies.

* * *

PrRu₂Si₂: a giant anisotropic induced magnet with a singlet crystal field ground state[†]

Abstract

The magnetic properties of PrRu₂Si₂ have been investigated experimentally by specific heat, single crystal magnetization, ¹⁴¹Pr Mössbauer and muon spectroscopies, neutron powder diffraction and inelastic neutron scattering, leading to the determination of its zero-field phase diagram and its crystal electric field energy levels below 40 meV. PrRu₂Si₂ undergoes a magnetic phase transition at $T_N \simeq 16$ K to an axial incommensurate sine wave magnetic structure characterized by a wave vector $\tau = (0.133, 0.133, 0)$, followed by a first order phase transition at $T_C \simeq 14.0$ K to an axial ferromagnetic structure. The lowest crystal electric field states are the two singlets $|\Gamma_{t1}^{(1)}\rangle$ and $|\Gamma_{t2}\rangle$ separated by 2.25 meV. The low temperature properties are described by a Hamiltonian identical to that of an Ising system with a transverse magnetic field. Since the ratio of the exchange energy to the energy splitting between the singlets is sufficiently large, it exhibits spontaneous magnetization. The nature of the two singlet states explains the giant magnetic anisotropy. The random phase approximation predicts the value of the high field magnetization but yields a low field magnetization too small by $\sim 15\%$. Possible application of these results to uranium intermetallic compounds is pointed out.

[†] Published in a slightly modified form in Phys. Rev. B 56 (1997) 8752.

5.1 Introduction

Magnetic anisotropy is one of the most interesting and important subjects in magnetism. Ternary compounds RM_2X_2 (R = rare earth or actinide, M = $3d$, $4d$ or $5d$ transition metal and X = Si or Ge) with the tetragonal ThCr_2Si_2 -type structure exhibit large magnetic anisotropy. Among these compounds, large anisotropy has been reported in Pr compounds (see Table 1 of ref. [60] and ref. [61]). The largest measured anisotropy has been found for PrRu_2Si_2 : its anisotropy field is $\simeq 400$ T [60]. This giant anisotropy is unexplained. It has been suggested that hybridization-induced anisotropy and/or anisotropic exchange interaction play a significant role [60]. This compound was previously believed to present only a single magnetic phase transition to a ferromagnetic state [62] at $T_C = 14$ K. Only the Pr ions contribute to the magnetic properties of the compound.

Interestingly enough, Pr^{3+} has a $^3\text{H}_4$ Hund's rule ground multiplet as has U^{4+} . The latter is the usually assumed ionization state of uranium in intermetallics such as the well studied URu_2Si_2 heavy fermion compound [63, 64].

In this chapter a study of the static magnetic properties of PrRu_2Si_2 using macroscopic and microscopic experimental techniques is reported. The organization of this chapter is as follows. In sec. 5.2, experimental results are presented. Section 5.3 is devoted to the determination of the low energy crystal electric field (CEF) level scheme and to the analysis of the magnetic properties using either the molecular field or the random phase approximation. In the last section the results are discussed. In Appendix 5.A the eigenvalues and associated eigenstates of the CEF hamiltonian are listed.

5.2 Experimental results

The measurements have been performed on polycrystalline samples, except for the magnetization and muon spin relaxation measurements which were carried out on single crystals.

5.2.1 Specific heat

The temperature dependence of the magnetic specific heat of PrRu_2Si_2 , measured at temperatures ranging from 4.3 to 67 K, is presented in Fig. 5.1. The lattice and conduction electron contributions have been estimated from measurements on LaRu_2Si_2 and are subtracted from the raw PrRu_2Si_2 data. A well defined anomaly is observed at the ferromagnetic ordering temperature $T_C = 14.0$ K. In addition a weak anomaly is observed starting at ~ 16 K (see the insert of Fig. 5.1). As will be shown in section 5.2.4 and 5.2.5, this anomaly corresponds to a second magnetic phase transition. In Fig. 5.2 the temperature dependence of the entropy computed from the magnetic specific heat data is displayed. This entropy reaches $R \ln 2$ at ~ 30 K, indicating there are two levels of equal degeneracy populated below that temperature including the ground state.

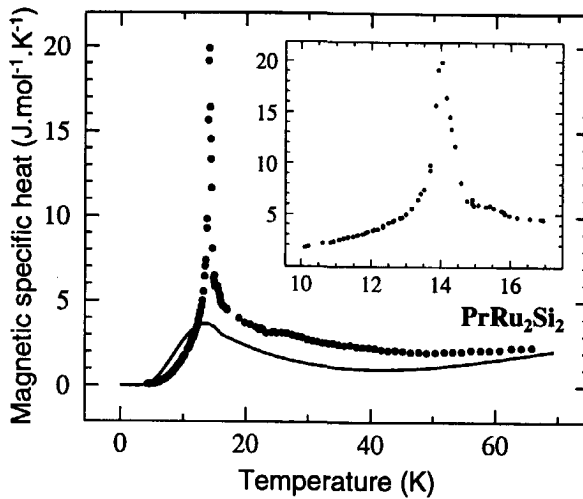


Figure 5.1: Temperature dependence of the magnetic specific heat of PrRu_2Si_2 . The lattice and conduction electron contribution has been estimated from measurements on LaRu_2Si_2 and subtracted from the raw PrRu_2Si_2 data. The solid line is the prediction of the molecular field approximation with the energy levels shown in Fig. 5.11. The contribution of the two phase transitions is not taken into account.

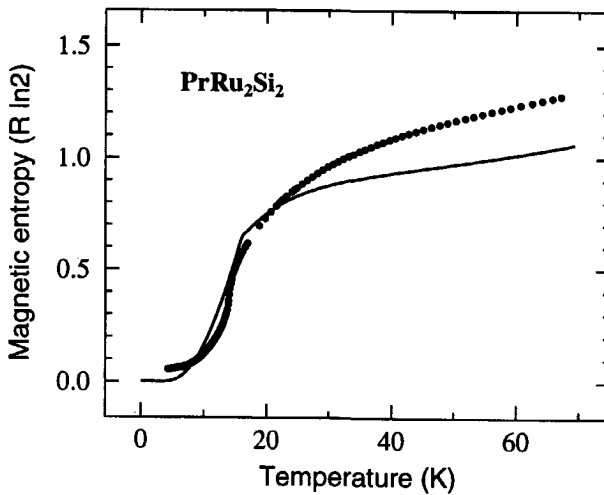


Figure 5.2: Temperature dependence of the entropy computed from the specific heat presented in Fig. 5.1. The solid line corresponds to the model used in that figure.

5.2.2 Single crystal magnetization

The magnetization measurements have been performed using a SQUID magnetometer. The data are shown in Fig. 5.3. They indicate that the bulk magnetic moment at 4.5 K is $2.69 \mu_B$, in agreement with the previously reported result of $2.7 \mu_B$ [60]. Even at a temperature twice the value of T_C the anisotropy is strong: whereas in an applied magnetic field of 5.5 T the magnetization at 28 K is $2.5 \mu_B$ when measured along the c axis, it is only $0.032 \mu_B$ for the field applied along the a axis.

High field magnetization measurements have been performed in fields up to 35 T. These measurements confirm the strong anisotropy of this compound. At 4.2 K, in an applied field of 35 T, the value of the magnetization measured along the c and a axes is $3.08 \mu_B$ and $0.39 \mu_B$, respectively.

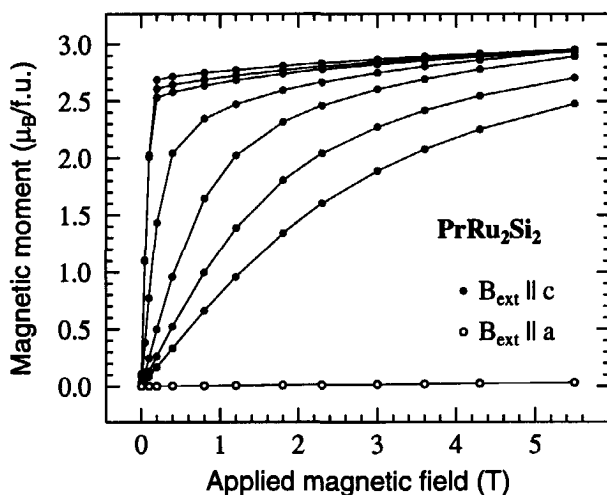


Figure 5.3: Field dependence of the magnetization recorded on a single crystal of PrRu_2Si_2 with the magnetic field, B_{ext} , parallel to the c axis for different temperatures: 4.5 K, 10.5 K, 12 K, 16 K, 20 K, 24 K and 28 K (filled circles). For a given field, the higher the temperature, the lower the magnetization. In addition data taken at 28 K with B_{ext} parallel to the a axis (empty circles) are presented. The solid lines are guides to the eyes.

5.2.3 ^{141}Pr Mössbauer spectroscopy

The ^{141}Pr Mössbauer measurements (145.4 keV nuclear transition) have been performed using a special counting technique. The current was directly integrated from the detector, instead of counting single events [65]. All the spectra were measured with a CeF_3 source (initially 750 mCi) kept at 4.2 K, working with an acceleration-type spectrometer in sinusoidal mode. The velocity was calibrated

with a $^{57}\text{Co}:\text{Rh}$ source and a $\alpha\text{-Fe}_2\text{O}_3$ absorber at room temperature.

The ^{141}Pr Mössbauer spectra were recorded at temperatures from 4.2 to 25 K. The spectrum measured at 4.2 K is shown in Fig. 5.4. From the splitting of the absorption lines, a hyperfine field at the nuclear site of 281 T is deduced. This corresponds to a Pr $4f$ magnetic moment of $2.76 \mu_B$ (see also Fig. 5.7). The small difference between this value and the value measured by magnetization is understood if one realizes that the $5d$ electrons of any rare-earth ion contribute to the bulk magnetization. This $5d$ moment equals $\sim 0.1 \mu_B$ and is oriented antiparallel to the $4f$ moment for a light rare-earth ion [66] as shown from X-ray magnetic circular dichroism measurements [67].

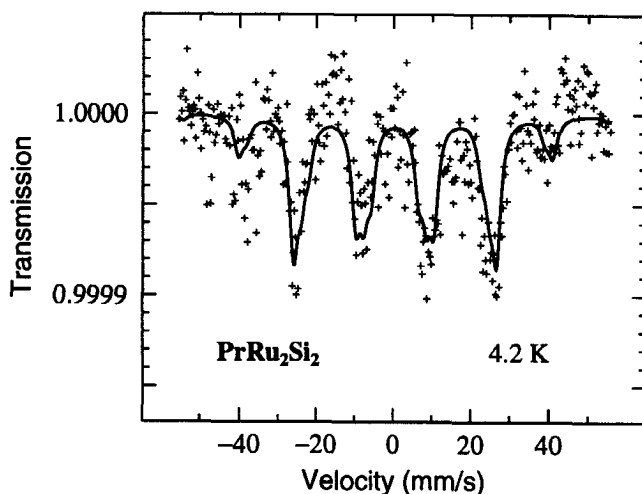


Figure 5.4: ^{141}Pr Mössbauer spectrum of PrRu_2Si_2 recorded at 4.2 K. The solid line is a fit with the isomer shift and the hyperfine field as free parameters of which a Pr $4f$ moment of $2.76 \mu_B$ is deduced.

5.2.4 Muon spectroscopy

The muon spin (μSR) spectroscopy has proven to be a very powerful tool for the investigation of magnetic phenomena. $\mu^+\text{SR}$ experiments have been carried out at the ISIS muon facility located at the Rutherford Appleton Laboratory (U.K.). Figure 5.5 shows $\lambda(T)$ recorded in an applied longitudinal field of 0.2 T. This field is necessary to suppress the depolarization due to the ^{141}Pr nuclear magnetic moments, the effect of which is enhanced by the large hyperfine coupling constant and Van-Vleck susceptibility [68].

The μSR results will not be discussed in details. Only those aspects giving information about the magnetic phase diagram will be analyzed.

$\lambda(T)$ presents two extrema, one at ~ 14 K and a second one at ~ 16 K. This shows that, in addition to the phase transition at T_C , there is a second magnetic

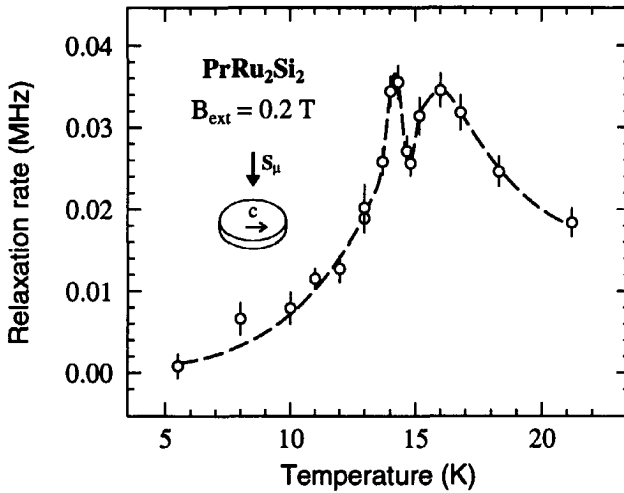


Figure 5.5: Temperature dependence of the μSR longitudinal exponential relaxation rate measured on PrRu_2Si_2 with $B_{\text{ext}} = 0.2$ T. The initial muon polarization is perpendicular to the c axis. The critical temperatures of the two magnetic phase transitions are located at temperatures for which the relaxation rate exhibits extrema. The dashed line is a guide to the eyes.

phase transition at $T_N \sim 16$ K. Although it is difficult to detect T_N in the magnetic specific heat data, muon spectroscopy clearly shows its signature.

5.2.5 Neutron powder diffraction

In order to further study the transition at T_N , we have performed neutron powder diffraction experiments in the temperature range 2 - 19 K. These experiments have been carried out in Grenoble at the Siloé reactor of the Commissariat à l'Energie Atomique on the DN5 linear multidetector diffractometer using an incident neutron wavelength of 2.487 Å. The data were refined using the MXD program [69]. The scattering lengths ($b_{\text{Si}} = 4.15$, $b_{\text{Pr}} = 4.58$ and $b_{\text{Ru}} = 7.03$ fm) were taken from ref. [70], and the magnetic form factor of Pr^{3+} from ref. [71]. Owing to a possible preferential orientation, the calculated intensities were corrected using the March formula [72]

$$M_{hkl} = \left[f_{\text{cor}} \cos^2 \alpha + \frac{\sin^2 \alpha}{f_{\text{cor}}} \right]^{-3/2} \quad (5.1)$$

where M_{hkl} is a corrective factor for the calculated intensity, f_{cor} the fitted coefficient which reflects the importance of preferential orientation and α the angle between the c axis and the hkl plane.

The indexation of the nuclear Bragg peaks in the paramagnetic state ($T = 19$ K) confirms unambiguously the ThCr_2Si_2 type structure for this compound

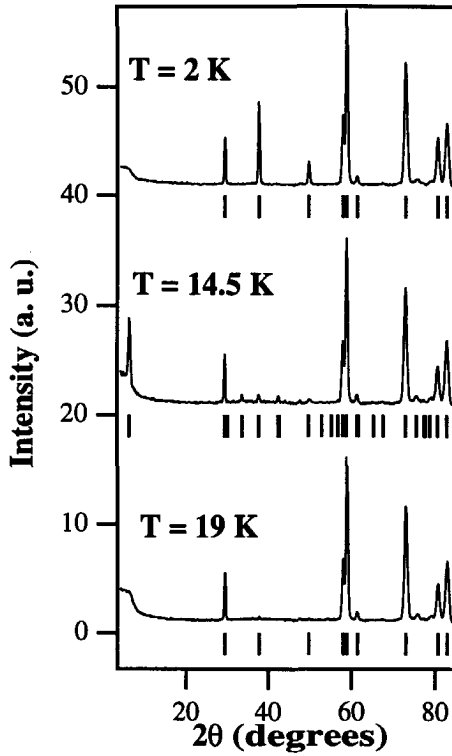


Figure 5.6: Neutron powder diffraction patterns from paramagnetic ($T = 19$ K), incommensurate plus ferromagnetic ($T = 14.5$ K) and ferromagnetic ($T = 2$ K) phases of PrRu_2Si_2 .

(space group $I4/mmm$): (i) one Pr atom in the $(0,0,0)$ site, (ii) two Ru atoms in the $(0, \frac{1}{2}, \frac{1}{4})$ and $(\frac{1}{2}, 0, \frac{1}{4})$ sites and (iii) two Si atoms in the $(0,0,z)$ and $(0,0,\bar{z})$ sites. The fit of the integrated intensities gives no evidence for any site interchange between the Ru and Si atoms. A quite good agreement (reliability factor equals 0.059) is obtained for $z_{\text{Si}} = 0.3634(24)$ and $f_{\text{cor}} = 1.114(20)$.

The values of the f_{cor} and z_{Si} factors are, within the experimental uncertainty, temperature independent. All the recorded spectra are well described because the reliability factors are never larger than $R = 0.063$. The lattice parameters a and c are temperature independent and equal $a = 4.1864(2)$ Å and $c = 9.755(15)$ Å.

Between $T_N \sim 16.0$ K and $T_C \sim 14.0$ K, additional reflections can be identified as seen in Fig. 5.6. Note the intense reflection at small diffraction angle which only exists in the incommensurate phase. The new reflections, due to the onset of the magnetic order, can be indexed with a wave vector $\tau = (0.133, 0.133, 0)$ which is temperature independent. The magnetic moments of this sine wave modulated structure are parallel to the c axis with an amplitude of $1.8(1) \mu_B$ at 14.5 K. Besides these reflections, additional intensities appear on the nuclear Bragg reflections

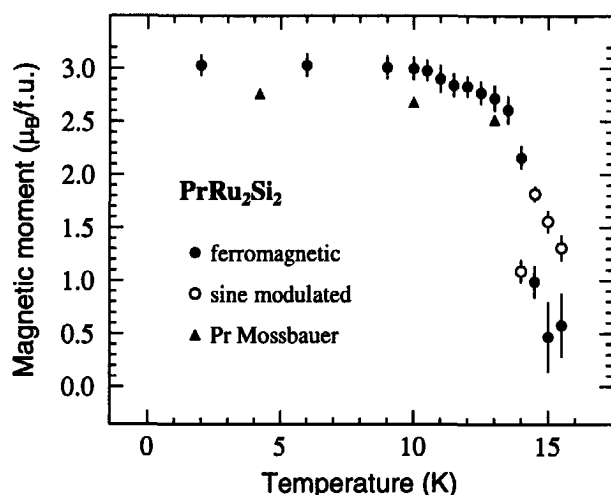


Figure 5.7: Temperature dependence of the $4f$ magnetic moment measured by neutron diffraction in PrRu_2Si_2 . Below 14 K an axial ferromagnetic structure is observed (filled circles). Between 14 and 16 K a second magnetic structure is observed characterised by an incommensurate sine wave modulation with $\tau = (0.133, 0.133, 0)$ (empty circles). In addition the $4f$ magnetic moment measured at three temperatures by $^{141}\text{Mössbauer}$ spectroscopy is presented (filled triangles).

that can be accounted for by a ferromagnetic contribution with the magnetic moments along the c axis. At 14.5 K the ferromagnetic moment is $1.0(1) \mu_B$. The temperature dependence of the ferromagnetic magnetic moment and of the amplitude of the incommensurate modulation are presented in Fig. 5.7. The ratio of the intensities of the two magnetic components depends on the experimental procedure, i.e., spectra recorded in cooling down or in warming up the sample. This is a characteristic for a first order transition at T_C . The values presented at Fig. 5.7 correspond to cooling down the sample from 19 K to 2 K.

Below T_C the sine wave phase has disappeared and only the ferromagnetic contribution remains with a Pr $4f$ moment of $3.0(1) \mu_B$ at 2 K. Although this value is slightly larger than the one deduced from magnetization and Mössbauer measurements ($\sim 2.8 \mu_B$), it is still reasonable taking into account the difficulty to measure precisely the intensity of the Bragg peaks in a textured powder sample. The temperature dependence of this moment as measured by neutron diffraction is plotted also in Fig. 5.7.

5.2.6 Inelastic neutron scattering

The inelastic neutron scattering (INS) method has been widely used to extract information on the energy level scheme of rare earth ions in intermetallic compounds. In favourable cases it allows to observe directly the dipolar transitions between the CEF energy levels of the rare earth ions. In order to simplify the ana-

lysis of the INS data the measurements are performed only in the paramagnetic phase. Since specific heat measurements [73] indicate that an excited CEF energy level is located at low energy, measurements on a sample with the Pr ions partly substituted by non magnetic La ions have been carried out. The substitution is expected to depress the magnetic ordering temperature but not too drastically modify the CEF acting on the Pr ions. We have chosen $\text{La}_{0.5}\text{Pr}_{0.5}\text{Ru}_2\text{Si}_2$ because magnetization measurements show that it is still paramagnetic at 2 K.

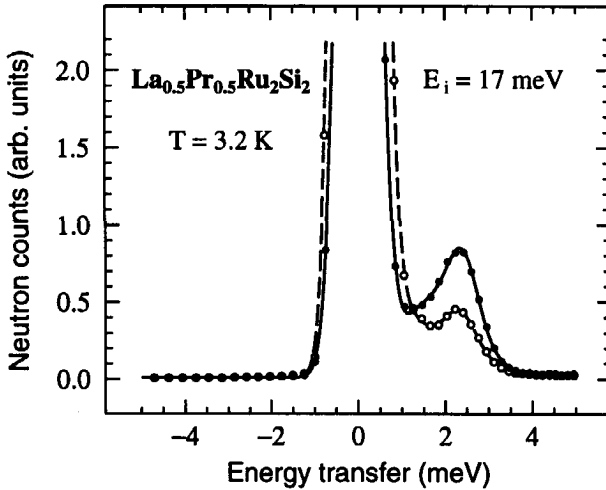


Figure 5.8: Spectral response of $\text{La}_{0.5}\text{Pr}_{0.5}\text{Ru}_2\text{Si}_2$ recorded at $T = 3.2$ K for an incident neutron energy $E_i = 17$ meV. The full and empty circles are for measurements performed at average scattering angles of 25.5° and 95° , respectively. The scattering at small angles is dominated by the CEF transition. The lines are guides to the eyes.

The INS measurements have been performed in Grenoble with the DN6 time of flight spectrometer located at the Siloé reactor. Thermal neutrons of incident energy $E_i = 17$ meV were used to record spectra at 3.2 K, 18.3 K, 52 K and 300 K. Additional scans at $E_i = 69$ meV were performed at temperatures 3.4 K and 52 K. The spectra were collected for scattering angles between 23° and 103° . The spectra are corrected for the background signal, yielding the total normalized response referenced to a vanadium standard. The angular dependence of the scattered intensity allowed to separate unambiguously the magnetic contribution to the scattering (proportional to the square of the magnetic form factor, which decreases when the wave vector q increases) from the phonon contribution (proportional to q^2). As shown in Fig. 5.8 and Fig. 5.9, in the energy range 1 meV - 40 meV only two inelastic peaks have been detected corresponding to crystal field excitations at 2.25(5) meV and 28.4(1) meV.

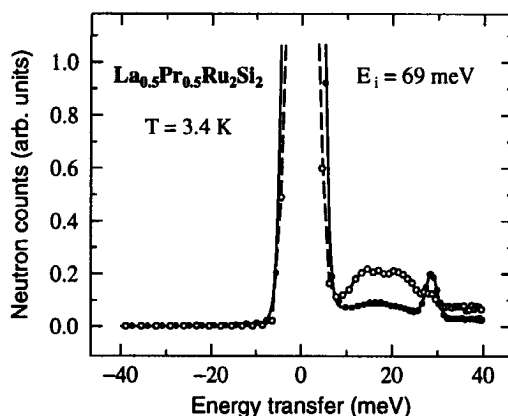


Figure 5.9: Spectral response of $\text{La}_{0.5}\text{Pr}_{0.5}\text{Ru}_2\text{Si}_2$ recorded at $T = 3.4$ K for an incident neutron energy $E_i = 69$ meV. The full and empty circles are for measurements performed at average scattering angles of 25.5° and 95° , respectively. The scattering at small angles is dominated by the CEF transition, whereas at 95° phonon excitations dominate the spectrum with a maximum intensity at ~ 17 meV. The lines are guides to the eyes.

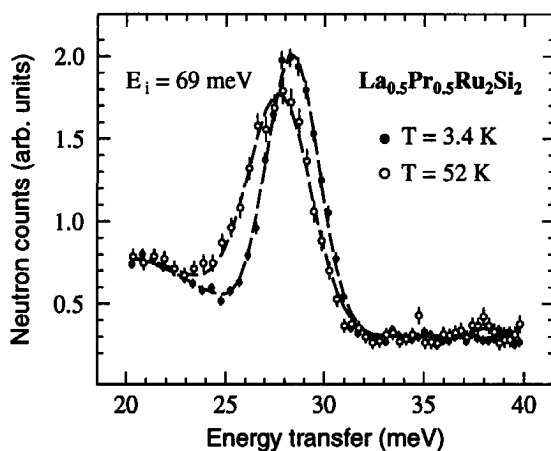


Figure 5.10: Comparison of the spectral response of $\text{La}_{0.5}\text{Pr}_{0.5}\text{Ru}_2\text{Si}_2$ recorded at 3.4 K and 52 K with an incident neutron energy $E_i = 69$ meV and at scattering angle of 25.5° . Only the data recorded in an energy transfer window centered around the high energy CEF transition are displayed. This comparison shows that both the energy and the full width at half maximum of the CEF transitions are temperature dependent. The dashed lines are guides to the eyes.

The high energy peak displays a clear temperature dependence as indicated in Fig. 5.10. While at 3.4 K the energy and the full width at half maximum are respectively 28.4(1) meV and 3.1(1) meV, at 52 K they are 27.7(1) meV and 3.8(1) meV respectively. The thermal behaviour of the high energy peak is consistent with the presence of the low energy CEF excitation (see 5.3.2).

5.3 Analysis of the experimental results

First the Hamiltonian is given which should account for the experimental results and describe some of the data with the CEF part of this Hamiltonian. Then, using the complete Hamiltonian, it will be attempted to analyse the magnetic data, first in the framework of the molecular field approximation, then in the random phase approximation. This latter analysis considers only the lowest two CEF levels.

5.3.1 Hamiltonian

The complete Hamiltonian used for describing the magnetic properties is written as the sum of three terms:

$$\mathcal{H} = \mathcal{H}_{cf} + \mathcal{H}_{\text{exch}} + \mathcal{H}_Z \quad (5.2)$$

Using the operator equivalent method and taking the z axis being parallel to the [001] direction, the CEF term \mathcal{H}_{cf} is written as

$$\mathcal{H}_{cf} = B_2^0 O_2^0 + B_4^0 O_4^0 + B_4^4 O_4^4 + B_6^0 O_6^0 + B_6^4 O_6^4 \quad (5.3)$$

where the O_l^m 's are the Stevens operator equivalents and B_l^m are CEF parameters [74].

$\mathcal{H}_{\text{exch}}$ describes the magnetic exchange interaction between the Pr^{3+} total angular momenta \mathbf{J} and \mathcal{H}_Z accounts for the Zeeman coupling.

5.3.2 Crystal field determination

First the CEF part of \mathcal{H} is considered. Its diagonalization provides the CEF eigenvalues and eigenstates, leading to lifting of the degeneracy of the $4f$ ground multiplet. For the Pr^{3+} ion ($J = 4$) in the tetragonal point group D_{4h} , the multiplet splits into five singlets ($\Gamma_{t1}^{(1)}, \Gamma_{t1}^{(2)}, \Gamma_{t2}, \Gamma_{t3}, \Gamma_{t4}$) and two doublets ($\Gamma_{t5}^{(1)}, \Gamma_{t5}^{(2)}$). The Γ_j 's are the irreducible representations of the point group. The eigenvalues and associated eigenstates can be expressed analytically in terms of the B_l^m parameters. They are given in Appendix 5.A.

The large magnetic moment observed at low temperature in combination with the specific heat and INS data allows to specify the nature and location of some of the CEF levels.

At $T \ll T_C$ the magnetic moment is so large that the CEF ground state must contain the $|\pm 4\rangle$ states, i.e. it is either $|\Gamma_{t1}^{(1)}\rangle, |\Gamma_{t1}^{(2)}\rangle$ or $|\Gamma_{t2}\rangle$ (see Appendix 5.A).

Of these, $|\Gamma_{t1}^{(1)}\rangle$ is the ground state of \mathcal{H}_{cf} because it has the lowest energy (the accidental case $b_1 = 0$ is discarded). This state is a non magnetic singlet. It is known that a large magnetic moment can be generated at low temperature from a magnetic singlet only if there is at least one CEF energy level located at an energy comparable to the exchange energy [75, 76, 77]. Since PrRu_2Si_2 is an axial ferromagnet, the exchange field is proportional to a J_z matrix element. Therefore the first excited CEF state, $|\text{first}\rangle$, must be such that $\langle\Gamma_{t1}^{(1)}|J_z|\text{first}\rangle$ is non zero. The only possible first excited state is $|\Gamma_{t2}\rangle$ since the $|\Gamma_{t1}^{(2)}\rangle$ state is located at higher energy (see Appendix 5.A).

The CEF dipolar transitions observed by INS are induced by the J_z , J_+ or J_- operators. The neutron cross section $I(i, f)$ between an initial state i and a final state f is given by:

$$I(i, f) = I_0 \left[\sin^2 \theta |\langle i | J_z | f \rangle|^2 + \frac{(2 - \sin^2 \theta)}{4} \times (|\langle i | J_+ | f \rangle|^2 + |\langle i | J_- | f \rangle|^2) \right] \quad (5.4)$$

where I_0 is a constant and θ the angle between the scattering vector and the quantization direction. Since $I(\Gamma_{t1}^{(1)}, \Gamma_{t2}) = 16I_0 \sin^2 \theta \sin^2 \beta_1$, this transition is intense only if $\sin^2 \beta_1$ is not too small. It corresponds to the peak seen at $\Delta = 2.25(5)$ meV. The only other possible neutron transitions from the ground state are to the $|\Gamma_{t5}^{(1)}\rangle$ and $|\Gamma_{t5}^{(2)}\rangle$ states (see appendix 5.A). The $|\Gamma_{t5}^{(1)}\rangle$ state being the lowest in energy, the peak observed at 28.4(1) meV is attributed to the transition from the ground state to this state. We have $I(\Gamma_{t1}^{(1)}, \Gamma_{t5}^{(1)}) = I_0(2 - \sin^2 \theta)(\sin \beta_1 \sin \beta_2 + \sqrt{5} \cos \beta_1 \cos \beta_2)^2$. Since probably $|\sin \beta_1| \approx 1$, (see sec. 5.3.3), $I(\Gamma_{t1}^{(1)}, \Gamma_{t5}^{(1)}) \simeq I_0(2 - \sin^2 \theta) \sin^2 \beta_2$. Because the high energy CEF excitation is intense, a substantial value for $\sin^2 \beta_2$ must exist.

Possible CEF levels below 28.4 meV which are invisible to the INS technique (i.e. $I(\Gamma_{t1}^{(1)}, f)$ small) are not likely because their presence would strongly enhance the Schottky anomaly even below 67 K (see sec. 5.3.3). The crystal field level scheme deduced from the analysis is drawn in Fig. 5.11.

It is observed that the high energy neutron peak (28.4 meV) has temperature dependent characteristics (see Fig. 5.10). This is easily understood because while at low temperature the observed peak is only produced by the neutron transition from the ground state $|\Gamma_{t1}^{(1)}\rangle$ to the $|\Gamma_{t5}^{(1)}\rangle$ state, at high temperature the ground and first excited state participate in the observed neutron transition. This explains the fact that at 52 K the observed peak is wider and located at lower energy than at low temperature.

In summary, the CEF ground state and first excitation state are singlet states well separated in energy from the other CEF states. Therefore the low temperature magnetic properties of PrRu_2Si_2 should be understood by considering the Pr^{3+} ions as two level systems interacting on a lattice. In the next section the level scheme of Fig. 5.11 is used to further analyse the data.

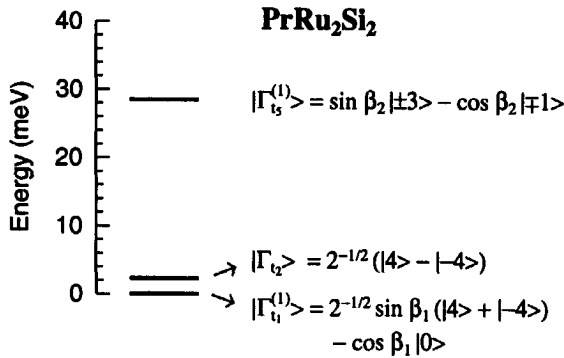


Figure 5.11: Crystal electric field energy level scheme of the Pr^{3+} ions in PrRu_2Si_2 deduced in this work. The inelastic neutron investigation did not detect any other states below 40 meV. The five states not mentioned in the figure are most likely located above 40 meV. They do not influence the magnetic properties at low temperature. The β_1 and β_2 values are near $\pi/2$.

5.3.3 Analysis of the data in the molecular field approximation

Both Trammell and Bleaney recognized a long time ago that exchange forces can induce magnetic ordering in a singlet CEF ground state if these forces are strong enough [75, 76]. An expression for the magnetization of the 4f electrons at $T = 0$ is obtained in the molecular field approximation [76]:

$$M_{4f}(T=0) = 4g_J\mu_B \sin \beta_1 \left[1 - \tanh^2 \left(\frac{\Delta}{2k_B T_C} \right) \right]^{\frac{1}{2}}, \quad (5.5)$$

where g_J is the Landé factor ($g_J = 4/5$ for Pr^{3+}), μ_B the Bohr magneton, k_B the Boltzmann constant and $\Delta = E_{t2} - E_{t1}^{(1)}$. The measurements give $\Delta = 2.25$ meV and $T_C = 14$ K. The observed INS peak intensity as well as the size of the magnetic moment indicate a value of $\sin^2 \beta_1$ close to 1. Using $\sin \beta_1 = 1$ and eq. (5.5), the maximum value that $M_{4f}(T=0)$ can reach is $2.18 \mu_B$. This is much lower than the experimental value of $2.8 \mu_B$.

To explain the observed moment value within the molecular field approximation, Δ should be reduced substantially or the magnetic ordering temperature should be drastically raised, i.e., one should have $\Delta/2k_B T_C = 0.53$ instead of 0.93. The first possibility is excluded since a INS transition is clearly observed at 2.25 meV and also the entropy shows no sign of a singlet below ~ 20 K. The second possibility is also excluded since specific heat, μSR and neutron diffraction indicate magnetic transitions at 14 and 16 K.

In addition, the shape of the magnetization curve as presented in Fig. 5.7 is more rectangular than a Brillouin curve. This is a signature of a first order

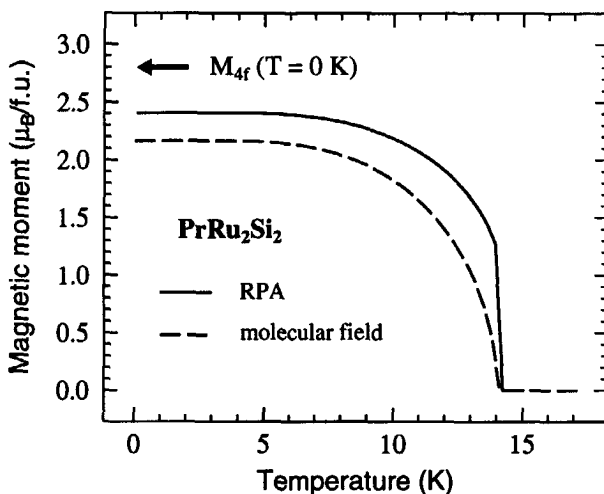


Figure 5.12: Calculated magnetization curve in the molecular field approximation (dashed line) and the random phase approximation (solid line). The arrow indicates the value of the magnetic moment of the 4f electrons as deduced from magnetization and Mössbauer measurements.

transition. In contrast to this, the molecular field approximation predicts that the ferromagnetic transition is second order (see Fig. 5.12).

Although the molecular field approximation does not provide a reasonable description of the low field magnetization measurements, it should be useful to understand the specific heat data since they should be dominated by the effect of the CEF levels, i.e. by the Schottky anomaly. It is not attempted to describe the specific heat related to the magnetic phase transitions. The solid line in Fig. 5.1 represents the calculated specific heat with a singlet at $E_{t2} = 2.25$ meV and a doublet at $E_{t5}^{(1)} = 28.4$ meV. Below T_C the effect of the molecular field is taken into account. The related entropy curve is shown in Fig. 5.2. The discrepancy between the model and the experimental data is small, taking into account the fact that the magnetic phase transitions are not described. Note that an extra singlet between 2.25 and 28.4 meV would yield a too large specific heat (and entropy). This is a strong indication that there is no other CEF levels below 40 meV, apart from the ones already identified (see Fig. 5.11).

The magnetic anisotropy measured at high field is controlled by the nature of the CEF energy levels and the Zeeman effect due to the field, i.e., the effect of the molecular field is small. Therefore the computation of the high field anisotropy should be reliable. At 5.5 T, $2.87 \mu_B$ and $0.03 \mu_B$ are computed for \mathbf{B}_{ext} parallel and perpendicular to c , respectively with the use of the crystal field levels presented in Fig. 5.11. At 35 T we have $3.14 \mu_B$ for \mathbf{B}_{ext} parallel to c , which is very closed to the experimental value ($3.08 \mu_B$) and $0.19 \mu_B$ for \mathbf{B}_{ext} perpendicular to c which

is twice as low as the experimental value, but this could be explained by a slight misalignment of the crystal which would have important consequences for a so strongly anisotropic crystal. These calculated values are then globally consistent with the data and previously published results [60].

5.3.4 Analysis of the magnetic properties in the random phase approximation

It is shown (in the previous section) that the molecular field approximation fails to provide a description of the low field magnetization. Referring to previous works on singlet magnets [78], this is not surprising.

Since the two singlets are close together collective excitations of the singlet ground state take place [79, 80, 81, 82]. These excitations are passed on from one atom to another, a process similar to that observed in spin waves. The most simple theory which attempts to account for these excitations is the Random Phase Approximation (RPA). In the paramagnetic state its Hamiltonian reduces to the Ising Hamiltonian in a transverse field. The energy spectrum of the excitations shows dispersion with a minimum energy gap at $\mathbf{k} = 0$ (zone center). The shape of the dispersion and the size of the energy gap depend on the exchange strength and the relative temperature $k_B T / \Delta$. Reaching T_C from either above or below, the energy gap decreases towards zero. This reduction of the energy gap is an effective channel to depopulate the singlet ground state and therefore, in the RPA, T_C is reduced compared with the molecular field approximation. Also the RPA magnetization curve is more rectangular due to this effect and the transition to the paramagnetic state becomes first order. Fig. 5.12 shows its predictions using the formalism of ref. [80]. It provides a better description than the molecular field approximation: it predicts that the transition is first order and yields a larger moment at low temperature. But this moment is still $\sim 15\%$ smaller than that observed.

5.4 Discussion and conclusion

Apparently, the RPA of ref. [79] gives a better description of the low temperature properties of PrRu_2Si_2 than the molecular field approximation. Note that $k_B T_C$ is of the same order as Δ and strong correlation effects are hence expected. However, these effects are not sufficiently taken into account in the RPA. Since the CEF parameters of PrRu_2Si_2 are now well defined, this compound provides a good system to test theoretical predictions for these correlation effects. In addition inelastic neutron scattering experiments on single crystals could reveal the nature of the dispersion.

To continue, the phase diagram of PrRu_2Si_2 will be discussed. It is noted that NdRu_2Si_2 exhibits the same magnetic structure below T_C and between T_C and T_N [83]. Only the values of T_C and T_N are different. This type of phase diagram, which has been found in many rare-earth-based intermetallics, has been

successfully explained by Gignoux and Schmitt with a periodic field model taking into account the crystal field anisotropy [84]. It appears that the exact boundaries of the magnetic phase diagram is determined by the real variation of the wave vector dependent exchange interaction and the crystal field.

In recent years the physics of uranium intermetallics has attracted much attention. The family of compounds with the ThCr_2Si_2 crystal structure is particularly interesting since it offers the possibility to study the effect of the hybridization of the f electrons with the $6d$ and p electrons in a systematic way [85]. Interestingly, the uranium $5f$ shell may have the same electronic structure as the Pr^{3+} $4f$ shell. The ground state and the first excited state may even be the same as in PrRu_2Si_2 [85]. Therefore the present results should help to understand the origin of the large magnetic anisotropy found in some uranium compounds. This work suggests that an effective crystal field Hamiltonian could be an efficient method for the description of the anisotropy.

In the ThCr_2Si_2 crystal structure family, URu_2Si_2 is being studied intensively since it is a heavy fermion superconductor. Its magnetic properties have been investigated with the Hamiltonian used for PrRu_2Si_2 , treated in the molecular field approximation [63, 64, 86]. Although URu_2Si_2 has a very small moment and PrRu_2Si_2 a large moment, this work indicates that the results of the molecular field approximation should be taken with caution. Recently Sikkema *et al.* have analysed the properties of URu_2Si_2 with a mean field like approximation [87]. Again we point out that this approximation may lead to erroneous results.

* * *

5.A Eigenvalues and eigenstates of the CEF hamiltonian

Here the eigenvalues and associated eigenstates of the CEF hamiltonian in terms of the B_i^m parameters are listed. First four intermediate parameters are defined; $a_1 = -15120B_6^0 + 120B_4^0 - 24B_2^0$, $b_1 = \sqrt{140}(12B_4^4 + 360B_6^4)$, $a_2 = 11340B_6^0 + 900B_4^0 - 12B_2^0$, $b_2 = \sqrt{7}(60B_4^4 - 180B_6^4)$. The eigenvalues are

$$E_{t1}^{(1)} = -10080B_6^0 + 960B_4^0 + 4B_2^0 - (a_1^2 + b_1^2)^{\frac{1}{2}}, \quad (5.A.1)$$

$$E_{t1}^{(2)} = -10080B_6^0 + 960B_4^0 + 4B_2^0 + (a_1^2 + b_1^2)^{\frac{1}{2}}, \quad (5.A.2)$$

$$E_{t2} = 5040B_6^0 + 840B_4^0 + 28B_2^0, \quad (5.A.3)$$

$$E_{t3} = 27720B_6^0 - 660B_4^0 - 8B_2^0 - 180B_4^4 + 2520B_6^4, \quad (5.A.4)$$

$$E_{t4} = 27720B_6^0 - 660B_4^0 - 8B_2^0 + 180B_4^4 - 2520B_6^4, \quad (5.A.5)$$

$$E_{t5}^{(1)} = -10080B_6^0 - 360B_4^0 - 5B_2^0 - (a_2^2 + b_2^2)^{\frac{1}{2}}, \quad (5.A.6)$$

$$E_{t5}^{(2)} = -10080B_6^0 - 360B_4^0 - 5B_2^0 + (a_2^2 + b_2^2)^{\frac{1}{2}}, \quad (5.A.7)$$

The following relations exist:

$$E_{t1}^{(1)} - E_{t2} = a_1 - (a_1^2 + b_1^2)^{\frac{1}{2}}, \quad (5.A.8)$$

and

$$E_{t1}^{(2)} - E_{t2} = a_1 + (a_1^2 + b_1^2)^{\frac{1}{2}}. \quad (5.A.9)$$

These relations mean that $E_{t1}^{(1)} \leq E_{t2} \leq E_{t1}^{(2)}$. In addition $E_{t5}^{(1)} \leq E_{t5}^{(2)}$.

The eigenstates are better written in terms of mixing angles because their normalization is then obvious. Other notations are not so transparent [63, 64]. For that purpose two angles β_1 and β_2 are defined through their tangent :

$$\tan \beta_i = \frac{(a_i + \sqrt{a_i^2 + b_i^2})}{b_i} \quad (5.A.10)$$

The eigenstate expressions are :

$$|\Gamma_{t1}^{(1)}\rangle = 2^{-\frac{1}{2}} \sin \beta_1 (|4\rangle + |-4\rangle) - \cos \beta_1 |0\rangle \quad (5.A.11)$$

$$|\Gamma_{t1}^{(2)}\rangle = 2^{-\frac{1}{2}} \cos \beta_1 (|4\rangle + |-4\rangle) + \sin \beta_1 |0\rangle \quad (5.A.12)$$

$$|\Gamma_{t2}\rangle = 2^{-\frac{1}{2}} (|4\rangle - |-4\rangle) \quad (5.A.13)$$

$$|\Gamma_{t3}\rangle = 2^{-\frac{1}{2}} (|2\rangle - |-2\rangle) \quad (5.A.14)$$

$$|\Gamma_{t4}\rangle = 2^{-\frac{1}{2}} (|2\rangle + |-2\rangle) \quad (5.A.15)$$

$$|\Gamma_{t5}^{(1)}\rangle = \sin \beta_2 |\pm 3\rangle - \cos \beta_2 |\mp 1\rangle \quad (5.A.16)$$

$$|\Gamma_{t5}^{(2)}\rangle = \cos \beta_2 |\pm 3\rangle + \sin \beta_2 |\mp 1\rangle \quad (5.A.17)$$

Notice that when analysing data it is more practical and physical to consider the energy difference between the CEF levels and the two mixing angles than the B_l^m parameters.

* * *

Muon site and muon dynamics in GdNi_5

Abstract

GdNi_5 is a ferrimagnet of which the magnetic properties are well understood. Here we report on the muon dynamics in this compound which shows new features and has consequences for the interpretation of the μ^+ SR data. In this respect GdNi_5 can be regarded as a model system to deepen our knowledge about the μ SR technique.

The muon localizes at the $3f$ interstitial site and below ~ 80 K a second muon site becomes populated, the $6m$ site. The $6m$ sites are located in a ring surrounding the $(0,0,\frac{1}{2})$ site and the muon occupies all sites within the sensitivity scale of the experiment. This $6m$ site is metastable and the muon hops, during the μ SR experiment, to the $3f$ site.

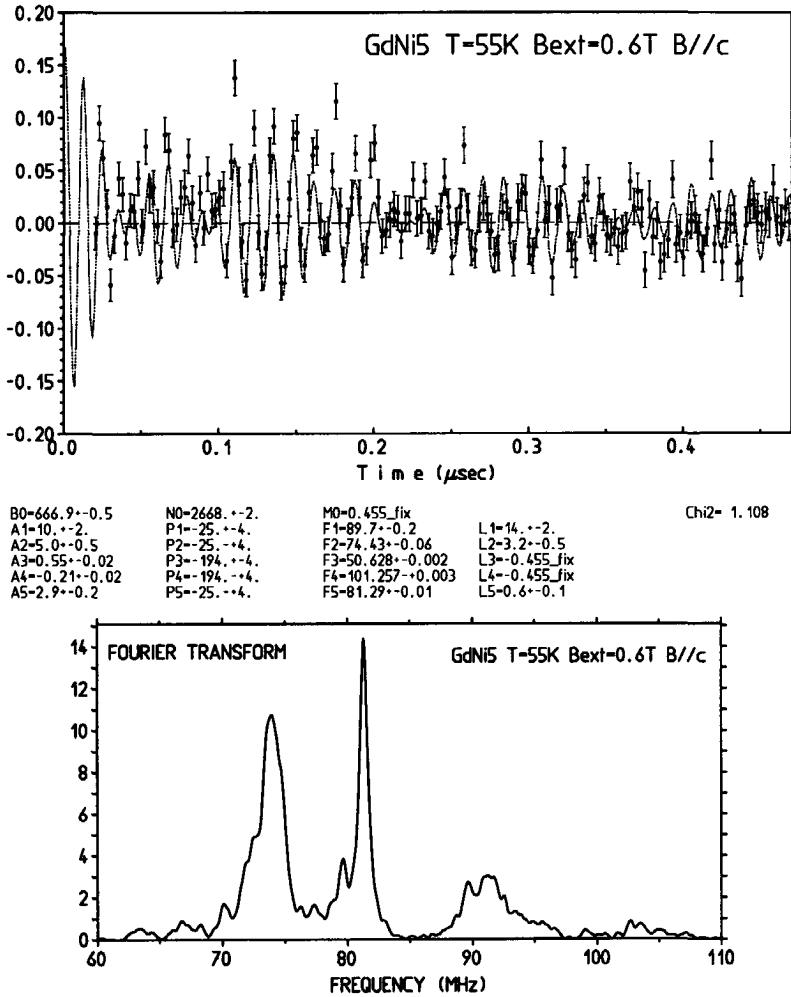


Figure 6.1: A typical muon spectrum measured on a single crystal of GdNi₅. The spectrum is analysed with five muon precession frequencies of which the last three are due to the muon beam pulsation (50.6 and 101.2 MHz) and the Cu background of the sample holder. Also the Fourier transform of this spectrum is shown.

6.1 Introduction

The magnetic properties of GdNi₅ have been studied intensively and are well understood [88]. The Gd 4*f* shell is spherical and therefore its magnetic moment is insensitive to crystal field effects. The magnetic interaction is strong compared

to other rare earth atoms (de Gennes scaling) and governs the Curie temperature $T_C = 30.85$ K. GdNi_5 is a ferrimagnet with a Gd moment of $7 \mu_B$ and an induced Ni moment of $0.16 \mu_B$. The moments are preferentially aligned along the c axis and this anisotropy is caused by the dipolar interaction [89].

This compound has been a subject of study for muon spin relaxation ($\mu^+\text{SR}$) since 1990. $\mu^+\text{SR}$ has proven to be a powerful tool in the study of spin dynamics. Several fundamental theories have been developed to describe the muon depolarization in GdNi_5 . At low temperature the depolarization of the muon is governed by two magnon processes (Raman scattering) [90]. In the critical regime the muon damping rate is related to the critical magnetic fluctuations of the Gd moments [89].

In general, the muon localizes interstitially inside its host and this leads to a distortion of its near neighbour environment. Because of the positive charge of the muon it acts as a light proton, that is, it can be considered as a hydrogen like particle. At elevated temperatures the muon will diffuse through the lattice of its host and motional narrowing is commonly observed.

Below T_C the spontaneous magnetic field in GdNi_5 causes the muon to precess. Two different muon precession frequencies are observed (Fig. 6.2) which implies two different muon location sites because the magnetic structure in GdNi_5 is a simple one. Here we report on muon Knight shift experiments in order to determine these muon location sites.

6.2 The muon Knight shift

The muon, which is a spin $\frac{1}{2}$ particle, localizes at an interstitial site of the host crystal lattice (sec. 2.3). The local magnetic field it experiences, B_μ , causes the muon to precess with an angular frequency $\omega_\mu = \gamma_\mu B_\mu$, where γ_μ is the gyromagnetic ratio of the muon, $\gamma_\mu = 2\pi \times 135.539 \text{ MHz T}^{-1}$. The origin of B_μ can be either the magnetic ordering of the host atoms or an external field. In the latter case, the relative frequency shift experienced by the muon with respect to the external field B_{ext} is called the Knight shift, K_μ :

$$K_\mu = \frac{|B_\mu| - |B_{\text{ext}}|}{|B_{\text{ext}}|} = \frac{\omega_\mu}{\omega_{\text{ext}}} - 1 \quad (6.1)$$

with $\omega_{\text{ext}} = \gamma_\mu B_{\text{ext}}$. The field at the muon site equals:

$$B_\mu = B_{\text{ext}} + B_{\text{con}} + B_{\text{dip}} + B_L + B_D \quad (6.2)$$

where B_{con} and B_{dip} are the fields due to the Fermi contact interaction and the dipolar interaction between the muon and the moments of the host. $B_L + B_D$ is the contribution from the Lorentz and demagnetisation field which equals zero if the sample is of spherical shape.

The dipolar field due to a single moment of the host equals:

$$B_{\text{dip}}^i = \mu_0 \left\{ \frac{-\vec{M}_i}{r_i^3} + \frac{3 (\vec{M}_i \cdot \vec{r}_i) \vec{r}_i}{r_i^5} \right\} \quad (6.3)$$

where r_i is the distance between the muon and the moment M_i of atom i in the crystal lattice (see also Fig. 1.3). To calculate B_{dip} the sum is taken over all atoms in a sphere surrounding the muon and we obtain $B_{\text{dip}}^j = A_{\text{dip}}^{jj} M^j$ where A_{dip}^{jj} is the 3x3 dipolar coupling tensor and j one of the three crystallographic directions. All the moments outside the Lorentz sphere contribute to B_L . After correction for the Lorentz and demagnetisation field the Knight shift equals:

$$K_{\mu}^j = K_0 + (A_{\text{dip}}^{jj} + A_{\text{con}}) \chi^j, \quad j = \{a, \bar{a}, c\} \quad (6.4)$$

where A_{con} is the Fermi contact coupling tensor which is assumed to be small and isotropic. K_0 is the Knight shift due to the Pauli susceptibility of the conduction electrons. It is assumed temperature independent and small. χ^j is the susceptibility of the localized $4f$ electrons along the j direction. Because the dipolar interaction shows a strong angular dependence (see eq. (6.3)) A_{dip} is a muon site characteristic. This makes it possible to determine the muon location site by comparing experimental results with calculated values of A_{dip} .

6.3 Experimental procedure

A single crystal of GdNi₅ was prepared by the Czochralski method in Amsterdam from starting materials of at least 99,99 % purity. The cylindrical sample was grown with its cylinder axis parallel to the a axis and cut into shape with spark erosion. The susceptibility is determined with a SQUID magnetometer [88] for the three crystallographic directions. μ^+ SR measurements in the magnetically ordered state of GdNi₅ were performed on a mosaic of single crystal plates with the c axis in the plane. The spectra were taken at the GPS beamline at PSI (Fig. 6.2).

The μ^+ SR Knight shift measurements were performed at the μE1 beamline at PSI. The cylindrical sample ($\varnothing 7.5 \times 10$ mm) was mounted on a thin copper plate with the a axis perpendicular to the external field. The sample could rotate around the a axis which made it possible to align the external field along all crystallographic directions in the $\bar{a}c$ plane. An example of a muon spectrum and its Fourier transform are given in Fig. 6.1. The continuation of the μ^+ SR transverse field measurements took place at the GPS beamline which allows small sample dimensions. Therefore the sample was shaped into a sphere ($\varnothing 5.5$ mm) in order to avoid demagnetisation corrections and data were taken with the \bar{a} axis perpendicular to the external field, i.e. with the external field aligned along directions in the ac plane. All spectra were taken with $B_{\text{ext}} = 0.6$ T at temperatures between 35 K and room temperature.

The alignment of the sample along its crystallographic directions is of great importance because of the strong angular dependence of the dipolar interaction.

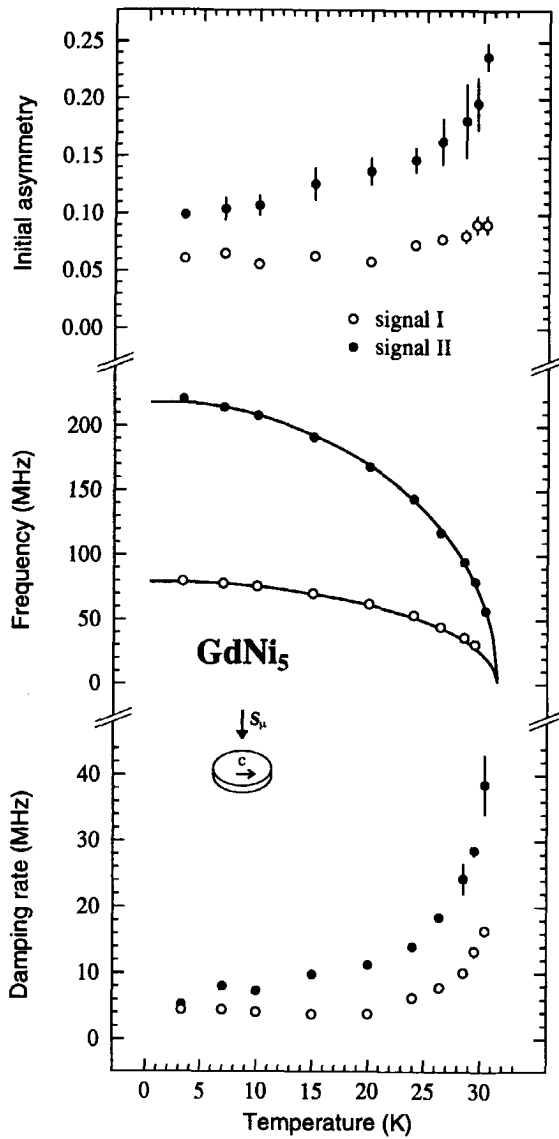


Figure 6.2: Initial asymmetries, precession frequencies and exponential damping rates observed in the magnetically ordered state of GdNi_5 . Two precession frequencies are observed, indicated as signal I and signal II. The initial muon polarization is perpendicular to the c axis.

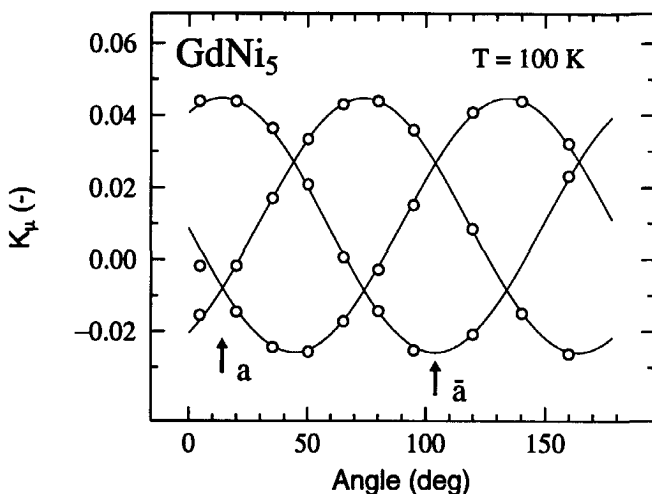


Figure 6.3: K_μ observed with B_{ext} aligned in the $a\bar{a}$ plane of the sample as function of φ . The orientation of the sample where the external field is parallel to the a and \bar{a} axis is indicated in the figure. The three signals show an equal asymmetry.

With X-ray Laue diffraction the sample is mounted with the a axis parallel to the rotation axis of the sample holder. Then the Knight shift measurements were performed with the external field along different orientations in the $a\bar{c}$ plane. Mounting the sample with its c axis parallel to the rotation axis of the sample holder allowed for measurements with $B_{\text{ext}} \parallel a\bar{a}$ plane.

Fig. 6.3 shows an angular scan measured at 100 K with B_{ext} parallel along different directions in the $a\bar{a}$ plane. For example, when the external field is applied along an arbitrary direction in the $a\bar{a}$ plane three muon precession signals are observed besides the signal which originated from the Cu sample holder. This background signal is included in the analysis of the spectra but is not plotted in the figures. Each of the precession signals are analysed with:

$$A(t) = A e^{-\lambda t} \cos(\omega_\mu t) \quad (6.5)$$

where A is the asymmetry, λ the damping rate and ω_μ the muon angular precession frequency.

When a change in orientation of the external field changes the direction of the Gd moments, the dipolar field at the muon site is modified as in eq. (6.3) and gives rise to the angular dependence of the Knight shift ($K_\mu \propto 3 \cos^2(\varphi - \varphi_0) - 1$) as it is drawn in Fig. 6.3. Here is $\varphi - \varphi_0$ the angle between the applied field and the a axis of the muons host and φ_0 is an offset angle. The signals of the three different sites are shifted 60 degrees with respect to each other. The period of the cosine modulation equals 180 degrees because the muon site resides on a two fold symmetry axis (along the c direction). If the external field is directed along the a or the \bar{a} axis, two of the three signals coincide. This makes it possible to align the

sample with the external field along the a or \bar{a} axis and measure the temperature dependence of the signals.

The results of the temperature scans with B_{ext} parallel to the a , \bar{a} and c axis are shown in Figs. 6.4, 6.5 and 6.6. The Knight shift is deduced from the observed muon precession frequencies with use of eq. (6.1).

6.4 Results

6.4.1 Determination of the muon sites

Figs. 6.4, 6.5 and 6.6 show that below ~ 80 K an extra precession signal is observed which has not been seen before in intermetallic compounds and is therefore an interesting feature. It suggests that two different muon location sites, observed in the magnetically ordered state, start to become populated below ~ 80 K. First the signals observed between ~ 80 K and 300 K will be discussed.

When $B_{\text{ext}} \parallel c$ a single signal is observed which indicates degeneracy of the three signals seen in Fig. 6.3. If $B_{\text{ext}} \parallel a, \bar{a}$ two precession signals are observed with an asymmetry ratio of 1:2 as it is also seen in Fig. 6.3. The increase of the Knight shift with decrease in temperature reflects the increase in susceptibility. Fig. 6.7 clearly demonstrates the linear relation between the Knight shift and the susceptibility of GdNi_5 . With use of eq. (6.4) the components of the coupling tensor $A_{\text{dip}} + A_{\text{con}}$ are deduced from the slopes of Fig. 6.7. For $B_{\text{ext}} \parallel \bar{a}$ and c the slopes are corrected for the demagnetisation field of the cylindrical sample. After these corrections the data are consistent with measurements on the spherical sample ($B_{\text{ext}} \parallel a, \bar{a}$). Care has to be taken since the three signals have a phase shift of 60 degrees with respect to each other in the $a\bar{a}$ plane. $\varphi - \varphi_0$ equals zero if the angle between the position vector of the muon site and the direction of the external field is zero. In that case the coupling tensor is diagonal. Else the Knight shift couples to χ^a as well as $\chi^{\bar{a}}$ and the related rotation of the coupling tensor gives rise to off diagonal terms.

Table 6.1 contains the coupling tensor deduced from experiment. The Fermi contact interaction is assumed to be isotropic and the trace of the dipolar interaction tensor equals zero. Therefore the two contributions are readily separated and the result is also listed in table 6.1. To establish the muon location site, the dipolar coupling tensor deduced from experiment is compared with calculated values for several interstitial sites. In PrNi_5 the muons localize at the $6i$ site ($\frac{1}{2}, 0, 0.21$) [91]. From table 6.1 we conclude however, that the $3f$ site is the most likely site for the muon localize in GdNi_5 in the temperature range between ~ 80 and 300 K (see Fig. 6.8). This $3f$ site is also suggested as the muon location site in LaNi_5 [92]. Note that the $3f$ site is consistent with the asymmetry ratio of the two signals observed with $B_{\text{ext}} \parallel a$ and $B_{\text{ext}} \parallel \bar{a}$. Note also that at 300 K (see Fig. 6.5) a single precession signal is observed. This is attributed to muon diffusion. The muon diffuses from site to site and experiences the average field of the two precession signals.

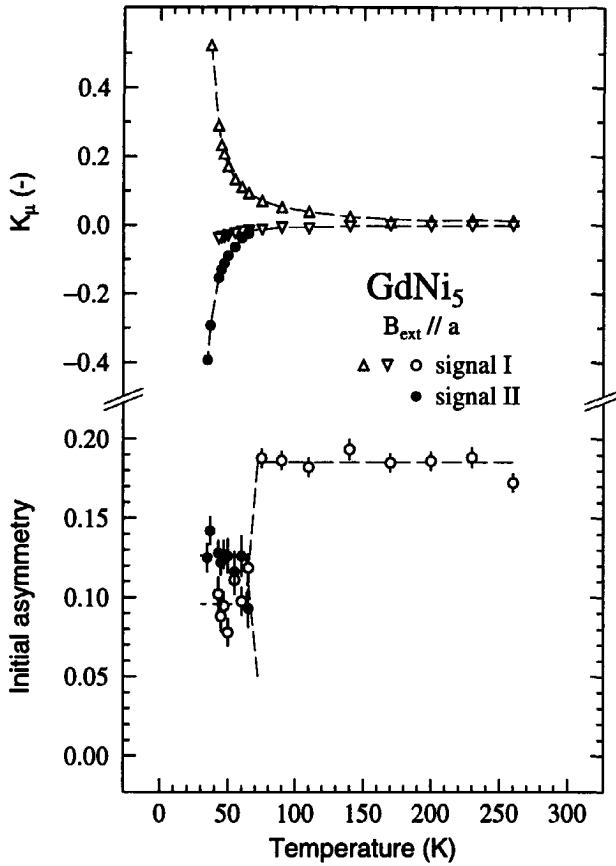


Figure 6.4: Knight shift and asymmetry of the muon precession frequencies observed in GdNi_5 as function of temperature with $B_{\text{ext}} \parallel a$. The empty symbols originate from one muon location site (signal I) and the asymmetry ratio of these two signals equals $\Delta: \nabla = 1:2$ (see Fig. 6.3). In the lower plot the total asymmetry of these signals is plotted because they originate from the same muon site. Below ~ 80 K an extra signal is observed (signal II) which corresponds to a second muon site.

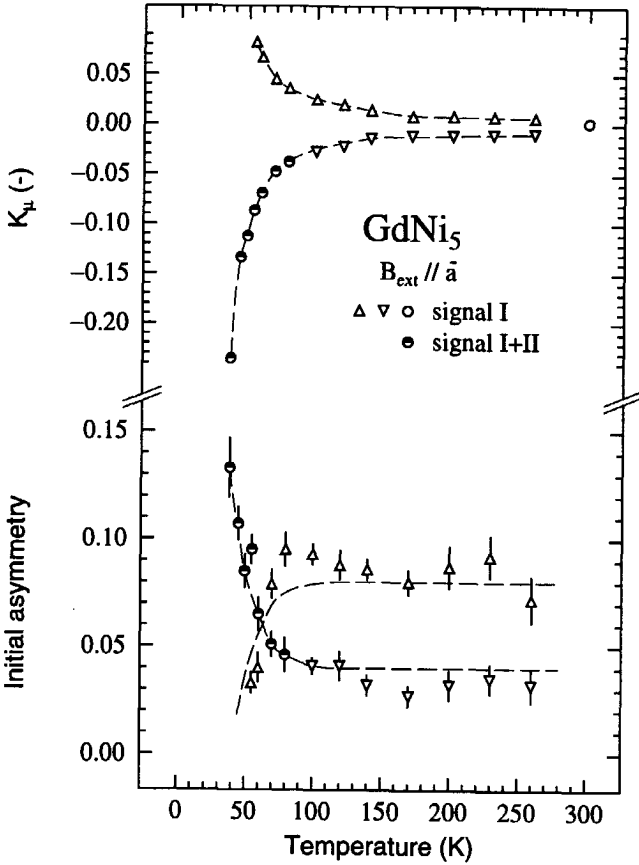


Figure 6.5: As in Fig. 6.4 but with $B_{\text{ext}} \parallel \bar{a}$. The two signals observed between 80 and 300 K originate from one muon site (signal I) and show an asymmetry ratio of $\Delta : \nabla = 2:1$. Note the muon diffusion starts at 300 K and causes the two signals to collapse (empty circle). Below ~ 80 K the asymmetry of the signal with the lowest K_μ increases. This is due to the fact that a second muon site becomes populated with a similar value of K_μ (signal II). The disappearance of the signal indicated with Δ is explained in the text.

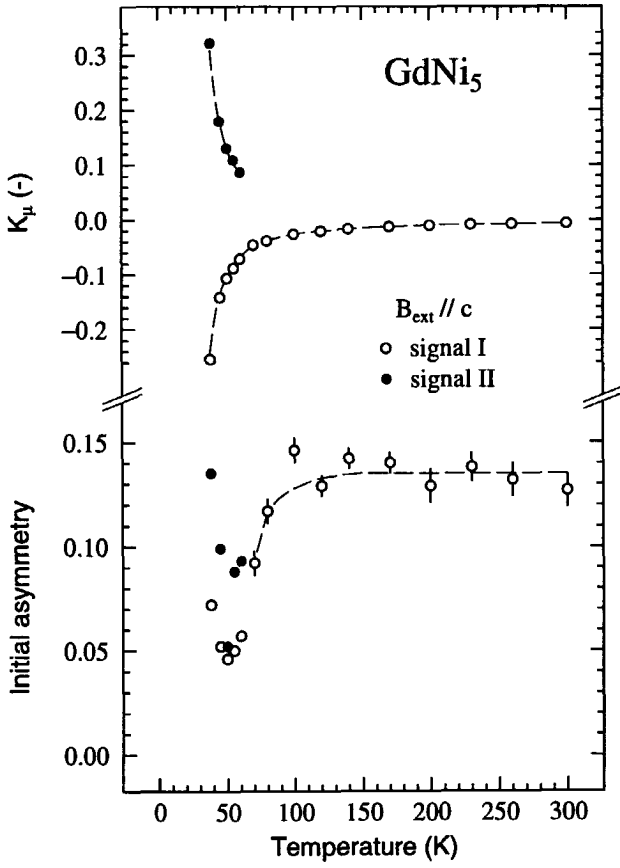


Figure 6.6: As in Fig. 6.4 but with $B_{\text{ext}} // c$. Below ~ 80 K a second muon site becomes populated (filled circles).

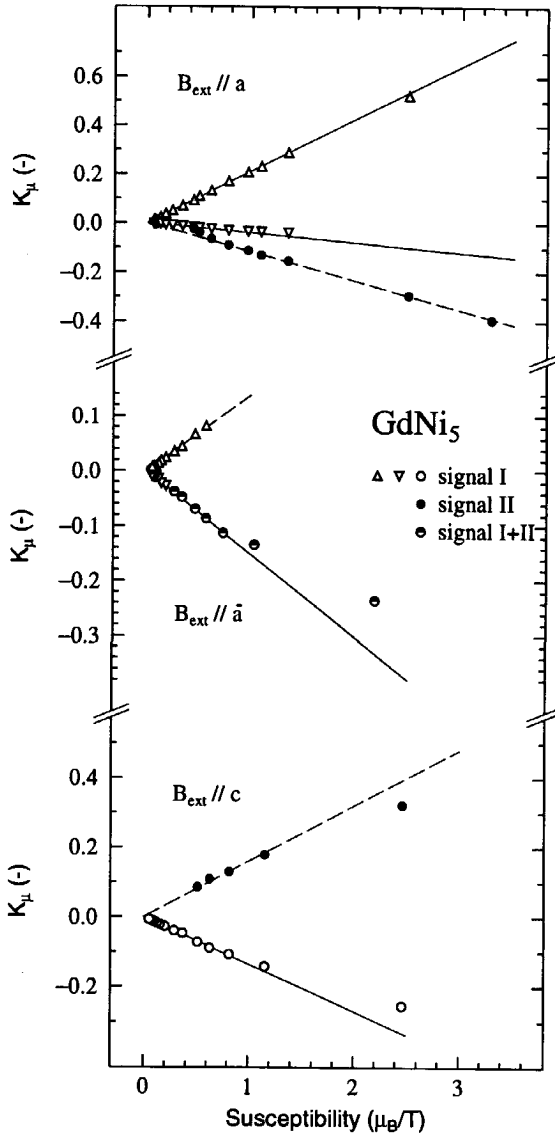


Figure 6.7: K_μ observed with $B_{\text{ext}} \parallel a, \parallel \bar{a}$ and $\parallel c$, plotted as function of the susceptibility of GdNi_5 [88]. After correction for demagnetisation, the slope of the curves determines $A_{\text{dip}} + A_{\text{con}}$. Signal I disappears in the plot, although the muon site is still occupied, for reasons mentioned in section 6.4.2.

Table 6.1: Calculated dipolar coupling parameters for several interstitial sites in GdNi₅ combined with the experimental values. The latter combine the dipolar A_{dip} (trace = 0) and Fermi contact interaction A_{con} (isotropic). Signal I is observed in the whole measured temperature range (4-300 K) and corresponds to the 3f site. Signal II appears below ~ 80 K and corresponds to $\langle A_{\text{dip}}^{6m} \rangle$ which implies the muon occupies all 6m sites within the sensitivity scale of the experiment (10^{-9} s).

Site	A^{aa} ($\text{T}\mu_B^{-1}$)	$A^{\bar{a}\bar{a}}$ ($\text{T}\mu_B^{-1}$)	A^{cc} ($\text{T}\mu_B^{-1}$)
Calculated			
3f ($\frac{1}{2}, 0, 0$)	0.219	-0.106	-0.113
6i ($\frac{1}{2}, 0, 0.1$)	0.202	-0.103	-0.099
6i ($\frac{1}{2}, 0, 0.21$)	0.154	-0.095	-0.059
6j ($0.4, 0, 0$)	0.287	-0.142	-0.145
1b ($0, 0, \frac{1}{2}$)	-0.230	-0.230	0.459
2c ($0, 0, 0.25$)	-0.985	-0.985	1.969
2d ($\frac{1}{3}, \frac{2}{3}, \frac{1}{2}$)	0.0015	0.0015	-0.0029
4h ($\frac{1}{3}, \frac{2}{3}, 0.2$)	0.030	0.030	-0.0605
6m ($0.13, 0.26, \frac{1}{2}$)	-0.037	-0.149	0.187
	$\langle A^{\text{plane}} \rangle = -0.093$		
Experimental			
signal I	0.215	-0.125	-0.124
A_{con}	-0.011	-0.011	-0.011
A_{dip}	0.226	-0.114	-0.113
signal II (T < 80 K)	-0.118	-0.118	0.165
A_{con}	-0.024	-0.024	-0.024
A_{dip}	-0.094	-0.094	0.188

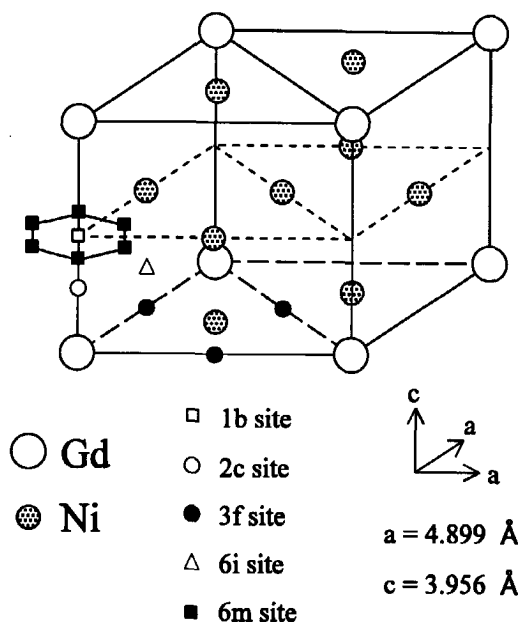


Figure 6.8: Hexagonal crystal structure of GdNi_5 (space group $P6/mmm$). Several interstitial sites are indicated. The muon localizes at the 3f site and below $\sim 80 \text{ K}$ also the 6m site becomes populated. The muons hop from 6m to 6m site within 10^{-9} s and a single degenerate muon precession frequency is observed in Fig. 6.9.

Below $\sim 80 \text{ K}$ we observe a new and interesting phenomenon as already mentioned before. An extra signal appears in the spectrum (black dots in Figs. 6.4, 6.5, 6.6 and 6.7). An angular scan in the aa plane at 47 K (see Fig. 6.9) shows the signature of this extra signal. If we compare this plot with Fig. 6.3 we note the following. Whereas the *three* 3f signals show a strong angular dependence, the extra signal is *single* and almost angular independent. Also with $B_{\text{ext}} \parallel c$ a *single* extra signal is observed (see Fig. 6.6). This suggests a second muon location site on a high symmetry axis as for example the 1b site or the 2c site (see Fig. 6.8).

From the slopes of the curves in Fig. 6.7 the coupling tensor has been deduced for this extra signal (table 6.1). Again the contribution from the dipolar interaction and the conduction electrons are separated. Table 6.1 shows the result and also the calculated values of the dipolar tensor for several interstitial sites with uniaxial symmetry. Note that the interstitial sites $(0,0,x)$ show a strong dipolar coupling with the Gd moments whereas the $(\frac{1}{3}, \frac{2}{3}, x)$ sites show a very weak coupling. The value of the dipolar coupling tensor deduced from experiment is between these values and does therefore not correspond to a muon site located on either one of

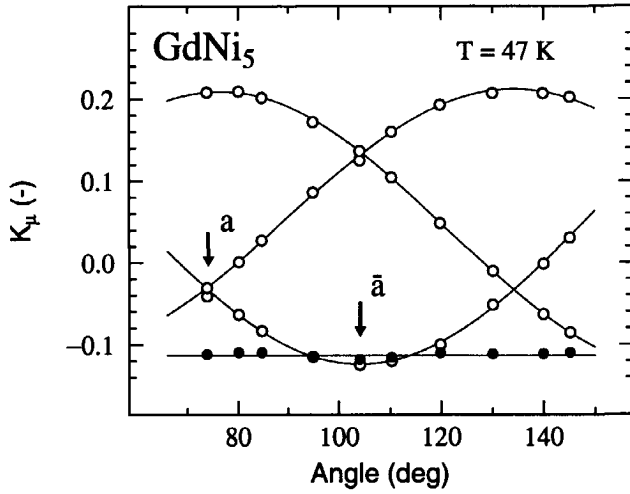


Figure 6.9: As in Fig. 6.3 but at $T = 47$ K. The signals originate from two muon location sites. The empty circles are also observed at 100 K and the filled circles correspond to a second muon site. Note that K_μ of this second signal is almost independent of the orientation of the external field.

these high symmetry axis.

Therefore we propose the extra signal is of different origin. The dipolar coupling tensor calculated for the $6m$ site, which is one of the five location sites of deuterium in LaNi_5D_x [93], shows an A^{cc} which corresponds to the experimental value. This A^{cc} is identical for all $6m$ sites. However, when B_{ext} is aligned in the $a\bar{a}$ plane the dipolar coupling is different for the different $6m$ sites and the degeneracy is lifted ($A^{aa} \neq A^{\bar{a}\bar{a}}$). This is in contrast with the observed signal. However, if the muon occupies all six $6m$ sites within the sensitivity scale of the experiment, it will experience an average dipolar field which is angular independent. The result of this calculation for the $6m$ site is shown in table 6.1 and corresponds to the experimental value. Therefore we conclude that each muon occupies all six sites within the time scale of the μSR experiment, $\sim 10^{-9}$ s. Without further experiments we cannot determine the mechanism for this observed behaviour. Processes such as muon tunneling, thermal diffusion or even a coherent quantum state are possible origins for this phenomenon.

With X-ray diffraction the crystallographic dimensions of GdNi_5 have been measured as a function of temperature (Fig. 6.10). In general the thermal expansion of the lattice can be described by the Grüneisenfunction [3, 94] which shows a linear expansion for $T/T_{\text{Debye}} > 0.5$ and a approximately constant unit cell volume below $T/T_{\text{Debye}} < 0.2$. For GdNi_5 this latter temperature is about 80 K (estimation $T_{\text{Debye}} \approx 400$ K) which is confirmed by the results presented in Fig. 6.10. Because the variation in unit cell volume below 100 K is not significant if compared with the experimental error, we cannot conclude if the occupation of the second muon site is related the open volume of the interstitial sites. We just

argue it is possible for the reasons mentioned above.

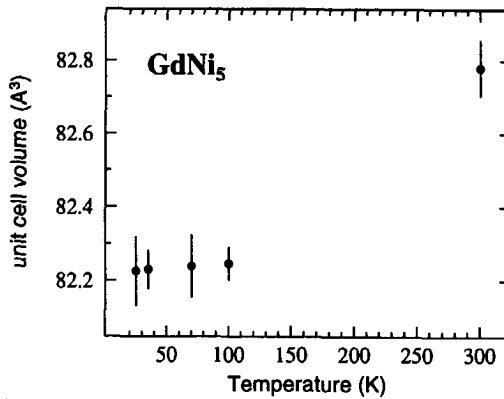


Figure 6.10: Unit cell volume of GdNi_5 as determined by X-ray diffraction. A small variation in unit cell volume is observed between 25 and 100 K but it is not significant if compared to the experimental error.

6.4.2 Muon hopping from the $6m$ to the $3f$ site

Below ~ 80 K the $6m$ site becomes populated with a surprisingly high damping rate (Fig. 6.11). This is most conveniently explained by a hopping muon. The muon resides for a while in the $6m$ site before it hops to the $3f$ site. As a consequence the population and therefore the asymmetry of the $6m$ signal decreases before the muon decays. Since the muon precession signal is analysed with eq. (6.5) this results in an enhanced damping rate although it reflects a decrease in asymmetry. The decrease in damping rate of the $6m$ signal between 70 K and 40 K is then due to an increase in muon residing time at this site before it hops on to the $3f$ site. Below 40 K the GdNi_5 spin dynamics cause the increase of the $6m$ damping rate.

Zero field μ^+ SR results on GdNi_5 [95] show that the damping rate is constant above 50 K which is in contrast with the results presented here. This confirms that the enhanced damping rate in Fig. 6.11 is due to muon hopping since the appliance of a magnetic field is not expected to induce a maximum in damping rate at 80 K when this feature is not visible in zero magnetic field.

The damping rate of the $3f$ signals are not strongly enhanced at 60 K (Fig. 6.11) indicating that the muon remains in the $3f$ site when it arrives there. In fact, there will be muons which initially localize at the $3f$ site and muons which localize there after they have resided at the $6m$ site. The local magnetic field at the $6m$ site is different from the local field the $3f$ site and therefore the muons precess with a different muon precession frequency. A muon which localizes first at the $6m$ site before it hops on will therefore have a phase shift with respect to a muon which localizes initially at the $3f$ site. As a consequence the observed

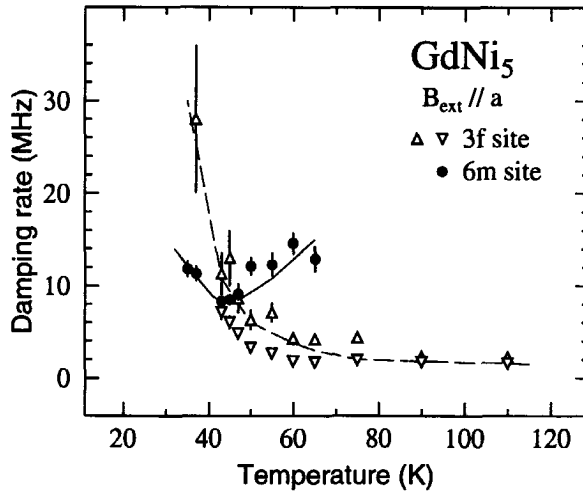


Figure 6.11: Damping rate from the muon precession signals plotted in Fig. 6.4. The lines are guides to the eye. Three remarkable features are observed. Firstly, the damping rates of the two signals originating from the 3f site (Δ and ∇) are not identical below 80 K. Secondly, the damping rate of the 6m site (\bullet) increases between 40 and 70 K. And thirdly the damping rates of the 3f and 6m site show a crossover at ~ 45 K. All these features are explained in the text.

damping rate of the 3f signal increases. In the extreme situation when there is a 180 degree phase shift between two muons, they do not contribute to the 3f asymmetry anymore.

The phase shift and consequently enhanced 3f damping rate, will be larger if the difference in magnetic field between the 3f and 6m site is larger (phase difference proportional to $\Delta\omega_\mu \cdot t$). This enhanced damping rate of the 3f signals is indeed observed. First, this explains the crossover in λ observed in Fig. 6.11. λ_{3f} increases when the temperature decreases because $\Delta\omega_\mu$ increases, while λ_{6m} decreases because of the increase in muon residence time at the 6m site. Second, it is difficult to observe the 3f precession signal if the frequency difference with the 6m site becomes large. This is clearly seen in Fig. 6.5 where one signal which originates from the 3f site disappears in the plot below ~ 50 K. μ^+ SR measurements in the magnetically ordered phase of GdNi_5 (Fig. 6.2) indicate two muon locations, which implies the 3f site is still occupied by muons below T_C . Hence, although the muons do localize at the 3f site, the signal is not observed because of the phase difference among these muons.

In Fig. 6.12 the 3f damping rate is plotted as function of the difference in precession frequency between the 3f and 6m site. The data were taken from Fig. 6.9 because all these data points were measured at the same temperature. This excludes the influence of the muon residing time at the 6m site on the 3f damping rate. Although there is a scattering in the data points, a clear increase in damping rate is observed with increasing frequency difference thereby confirming the muon

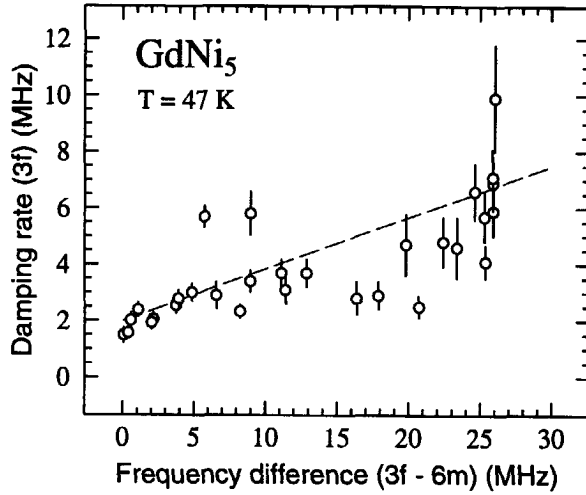


Figure 6.12: Damping rate of the precession signals originating from the 3f site as function of their frequency difference with the signal originating from the 6m site. An increase in damping rate is observed which is due to muons which hop from the 6m site to the 3f site within the time scale of the μ^+ SR experiment. Because the muons localized at the 6m site experience a different local field they have a phase shift when they arrive at the 3f site with respect to the muons already present at this site. This enlarges the observed 3f damping rate. The 3f damping rate is also influenced by the residing time of the muon at the 6m site. Therefore only the data points of Fig. 6.9 are shown in this figure because these spectra were taken at the same temperature.

hopping from 6m to 3f.

These features all suggest that muons localize at the 6m site below ~ 80 K from which they hop on to the 3f site. This implies that above ~ 80 K the muon has enough kinetic energy to find the 3f site. Below ~ 80 K however, the muon becomes trapped at the 6m site, i.e. in the local minimum of the potential energy. Because the 3f site is preferred, the muon hops on after a while.

6.4.3 Analysis of muon hopping

In general, the muon hopping from the 6m site to the 3f site can be described by a half life time τ_0 :

$$n_{6m}(t) = n_{6m}(0)e^{-t/\tau_0} \quad (6.6)$$

where $n_{6m}(t)$ equals the number of muons at the 6m site at time t [18]. The temperature dependence of τ_0 is a signature of the hopping process. When the muon localizes interstitially, the surrounding atoms are slightly displaced and the muon becomes self trapped. The potential energy of the muon is reduced on account of the elastic energy of the host atoms. For the muon to overcome the

energy barrier between the $6m$ and $3f$ site there are in principle two possible processes. The muon can use thermal energy to go to the $3f$ site or it can tunnel from one site to the other.

The first process, diffusion, is described by Arrhenius, i.e. $1/\tau_0 \propto e^{-E_a/k_B T}$ where E_a is the height of the energy barrier. In the second process phonons are involved. The phonons deform the potential profile around the muon and create identical energy levels in both potential wells. Then the muon can tunnel since its wavefunction becomes delocalized. The number of phonons involved determines the temperature dependence of τ_0 . For a single phonon process $1/\tau_0 \propto T$ is expected whereas for a double phonon process $1/\tau_0 \propto T^2$ is expected (sec. 3.2 of [18] and references therein).

Due to the muon hopping the performed analysis with eq. (6.5) is incorrect. The muons which initially localize at the $6m$ site and subsequently hop to the $3f$ site and become trapped there, introduce an extra term, $P_{6m \rightarrow 3f}(t)$, into the muon spectrum. We deduce for the total polarization function $A(t)$ (see for example refs. [18, 96]):

$$\begin{aligned}
 A(t) &= A_{6m}(t) + A_{3f}(t) + A_{6m \rightarrow 3f}(t) \\
 &= A_{6m}(t) + A_{3f}(t) + \\
 &\quad \text{Re} \left(\int_0^t A_{6m} e^{-\lambda_{6m} t'} e^{-i\omega_{6m} t'} e^{-\lambda_{3f}(t-t')} e^{-i\omega_{3f}(t-t')} \frac{1}{\tau_0} e^{-\frac{t-t'}{\tau_0}} dt' \right) \\
 &= A_{6m} e^{-\lambda'_{6m} t} \cos(\omega_{6m} t) + A_{3f} e^{-\lambda_{3f} t} \cos(\omega_{3f} t) + \\
 &\quad \frac{A_{6m}}{\tau_0 \sqrt{(\lambda'_{6m} - \lambda_{3f})^2 + \Delta\omega^2}} \left(e^{-\lambda_{3f} t} \cos(\omega_{3f} t + \phi) - \right. \\
 &\quad \left. e^{-\lambda'_{6m} t} \cos(\omega_{6m} t + \phi) \right) \quad (6.7)
 \end{aligned}$$

where

$$\lambda'_{6m} = \lambda_{6m} + \frac{1}{\tau_0}, \quad \Delta\omega = \omega_{6m} - \omega_{3f} \quad \text{and} \quad \tan \phi = \frac{\Delta\omega}{\lambda'_{6m} - \lambda_{3f}}.$$

λ_{6m} and λ_{3f} are the damping rates at the specific sites due to the spin dynamics of GdNi_5 . Eq. (6.7) is deduced for equal precession frequencies of all $3f$ sites as it is the case for $B_{\text{ext}} \parallel c$. When the degeneracy of ω_{3f} is removed (B_{ext} in any direction but not parallel to the c axis) eq. (6.7) is extended with an $P_{3f}(t) + P_{6m \rightarrow 3f}(t)$ term for each extra $3f$ precession frequency.

The data presented in this chapter are preliminary because the muon spectra are analysed with eq. (6.5) and not with eq. (6.7). It is recommended to include eq. (6.7) in the μ^+ SR analysis program in order to deduce τ_0 from the spectra. At the present time it is not possible to do such an analysis properly. Therefore only the preliminary results will be discussed in this chapter.

6.5 Discussion

6.5.1 Muon dynamics in GdNi_5

In this section the muon dynamics is discussed in the approximation of eq. (6.5). As mentioned in sec. 6.4.3 this approximation is not correct and only preliminary conclusions are presented here.

Fig. 6.2 shows that, in the magnetically ordered state, the damping rate of the two muon location sites is different. The damping related to the spin dynamics, as for example due to Raman scattering [90], is possibly different for the two sites since the symmetry and local electron density are different. However, at 4 K a small difference in damping rate is observed but above 5 K the damping rate of the $6m$ site increases and this continues up to T_C . Also the $6m$ asymmetry shows an abnormal behaviour. The increase of the $6m$ asymmetry confirms that the spectra analysis with two exponentially damped frequencies is not correct. An analysis with a Gaussian damping showed the same features. This suggests muon dynamics is still of importance below T_C .

The muon hopping from the $6m$ to the $3f$ site as well as in between $6m$ sites could be the origin. The first process shows signatures of slowing down below ~ 80 K but it is difficult to determine at which temperature the muons remain at the $6m$ site during the time scale of the experiment. No clear signatures are present of the slowing down of the second process but we can expect the muon to localize at a single $6m$ site at low temperature. Note that, because of the degeneracy of A^{cc} for the six $6m$ sites, this process will not be visible by means of a lifting of this degeneracy as it is the case for the $3f$ site below 300 K (see Fig. 6.5).

A $\mu^+\text{SR}$ experiment to determine the muon mobility at the $6m$ site can be done as follows. Because the magnetic anisotropy is small in GdNi_5 , the magnetic moments can be aligned in the $a\bar{a}$ plane by an external field in this direction. If the initial muon polarization is along the c axis muon precession frequencies are observed originating from the $3f$ and $6m$ site. If the muon at the $6m$ site is still occupying all $6m$ sites as it is observed in the paramagnetic state, a single precession signal originating from the $6m$ site is expected. However, if the muon is localized at a *single* $6m$ site the degeneracy will be lifted and two or three signals are expected, depending on the orientation of B_{ext} . The temperature dependence of the damping rate and the frequencies of the $6m$ site might elucidate the muon movement at this site and is therefore an interesting experiment.

6.5.2 Interaction of the muon with its host

Two significant deviations from the theory presented in sec. 6.2 are observed which deserve some attention.

1. Basal plane anisotropy

Fig. 6.13 shows that the $6m$ signal shows a small variation in precession frequency depending of the orientation of the external field in the $a\bar{a}$ plane. Because it is determined in secs. 6.4.1 and 6.4.2 that the muon occupies all

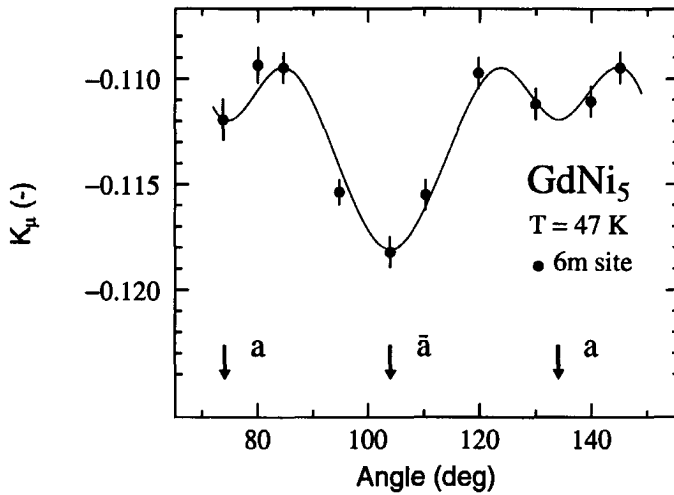


Figure 6.13: Weak angular dependence of the precession signal in the $a\bar{a}$ plane originating from the $6m$ site. This picture is a magnification of Fig. 6.3. The line is a guide to the eye.

$6m$ sites within the time scale of the experiment the dipolar field is averaged out. In fact, the dipolar field is constant in the $a\bar{a}$ plane and gives $K_\mu = \frac{1}{2} (A^{aa}\chi_{47K}^a + A^{\bar{a}\bar{a}}\chi_{47K}^{\bar{a}}) = -0.089$. Therefore, the small variation in Knight shift observed in Fig. 6.13 should be of a different origin.

A similar anisotropy is observed for the $3f$ site in Fig. 6.9. The difference in Knight shift, ΔK , between the precession signals is calculated taking into account the phase shift of 60° between the three signals and the corresponding rotation of D_{dip} :

$$\begin{aligned} \Delta K^a &= |0.75A^{aa}\chi^a - 0.75A^{\bar{a}\bar{a}}\chi^{\bar{a}}| \\ \Delta K^{\bar{a}} &= |-0.75A^{aa}\chi^a + 0.75A^{\bar{a}\bar{a}}\chi^{\bar{a}}| \end{aligned} \quad (6.8)$$

Clearly, ΔK is equal for $B_{\text{ext}} \parallel a$ and $B_{\text{ext}} \parallel \bar{a}$. However, from Fig. 6.9 we deduce $\Delta K^a = 0.239(3)$ and $\Delta K^{\bar{a}} = 0.255(3)$.

2. Hyperfine field below T_C

μ^+ SR shows two precession signals in the magnetically ordered state of GdNi₅ with $\omega_\mu^{6m} = 217$ MHz and $\omega_\mu^{3f} = 79$ MHz at $T = 0$ K (see Fig. 6.2). The frequency of both signals follows the Brillouin law with $J = \frac{7}{2}$. At $T = 0$ K a maximum Gd moment of $7 \mu_B$ is expected. Dipolar calculations have shown that the dipolar influence of the $0.16 \mu_B$ Ni moments is negligible.

Since the μ SR measurement was performed on a single crystal and all Gd magnetic moments are aligned along the c axis, the muon precession

frequency equals:

$$\omega_\mu = \gamma_\mu (A_{\text{dip}}^{\text{cc}} + A_{\text{con}} + A_L + A_D) \mu_{\text{Gd}} \quad (6.9)$$

$A_L + A_D$ are determined by comparing the results of Fig. 6.2 with the frequencies measured in a spherical sample of GdNi_5 . This indicates the demagnetisation field is close to the spherical value of $\frac{1}{3}$. $A_{\text{dip}}^{\text{cc}} + A_{\text{con}}$ are determined in sec. 6.4.1 and are assumed to be independent of the origin of the magnetic order, i.e. whether the Gd moments are spontaneous or induced by an external magnetic field [18]. Using eq. (6.9) we calculate for the two precession frequencies $\omega_\mu^{6m} = 157 \text{ MHz}$ and $\omega_\mu^{3f} = 117 \text{ MHz}$. These values do not correspond to the experimental ones. For the $6m$ and $3f$ site we deduce for this discrepancy $B_{\mu, \text{extra}}^{6m} = +0.44 \text{ T}$ and $B_{\mu, \text{extra}}^{3f} = +0.28 \text{ T}$, respectively.

The first item suggests an interaction between the muon and its host. In PrNi_5 [91] the muon induces an anisotropy in the local susceptibility below $\sim 50 \text{ K}$ because it changes the crystalline electric field at the Pr $4f$ shell. This change in crystal field influences the $4f$ eigenfunctions of the Pr atom and therefore its magnetism. In GdNi_5 the muon may cause a change in the magnetic density profile but, since the Gd $4f$ shell is spherical, a perturbation of the crystal field does not affect the Gd magnetism. However, the exchange interaction between the Gd magnetic moments could be changed by the presence of the muon and locally another magnetic ordering temperature is observed. This perturbation is expected to be anisotropic. In general the data can be corrected for this effect by fitting $K_\mu(T)$ to:

$$K_\mu = K_0 + \frac{(A_{\text{dip}}^{jj} + A_{\text{con}})C}{T - T_{C, \mu}} \quad (6.10)$$

where C is the Curie constant which follows from the GdNi_5 susceptibility (see eq. (1.8)). The dipolar coupling tensor A_{dip}^{jj} deduced with eq. (6.10) will be different from A_{dip}^{jj} deduced with eq. (6.4) because $T_{C, \mu} \neq T_C$. This correction could not be performed unambiguously (yet). The uncertainty in deduced Knight shift is too large, partly because the muon spectra are analysed with eq. (6.5) instead of eq. (6.7).

It is expected that this correction will modify the experimental values of $A_{\text{dip}}^{jj} + A_{\text{con}}$ listed in table 6.1. This correction might alter the position of the muon location sites although this is not expected. The asymmetry ratio between the two sites as well as the deuterium location site in LaNi_5D_x (see sec. 6.4.1) and the $3f$ location site observed in other LaNi_5 [92], all favour the $6m$ and the $3f$ interstitials as location sites of the muon in GdNi_5 .

The extra hyperfine field observed in the magnetically ordered state (item 2) seems larger than expected on behalf of the arguments mentioned above ($A_{\mu, 3f}^{\text{extra}} = 0.28 \text{ T}/7 \mu_B = 0.040 \text{ T}/\mu_B$). A possible origin of this can be the Ni atoms. Ni moments show an itinerant $3d$ magnetism for which the interaction with the conduction electrons is stronger than that for the localized Gd $4f$

shell. μ^+ SR measurements on metallic Ni [18] show a hyperfine field at the muon site due to the interaction via the conduction electrons of -0.071 T. Because of the high symmetry of the muon site in fcc-Ni, the dipolar field at the muon site vanishes and the local field is determined by the Fermi contact interaction. The Ni moments equal $1.1 \mu_B$ in metallic Ni and we calculate $A_{\text{con}}^{\text{Ni}} = -0.065 \text{ T } \mu_B^{-1}$.

In GdNi_5 there is an antiferromagnetic coupling between the Gd spin and the Ni moment. Therefore the Ni moments are directed along the negative c axis and in contrast with metallic Ni, the muon experiences a *positive* contribution to the hyperfine field via the Fermi contact interaction. For a small induced Ni moment of $0.16 \mu_B$ we calculate a hyperfine field of $+0.052$ T, which is a magnitude smaller than observed.

There is a third mechanism which could possibly be the origin of the extra hyperfine field. A hybridization between the Ni 3d electrons and the s-like wave function of the electrons surrounding the muon can occur [97]. Because such a hybridization realizes a direct interaction between the muon and the Ni magnetic density profile, the corresponding hyperfine field will be substantial.

At the present, we cannot distinguish between these suggested phenomena. Further analysis of the data with eq. (6.7) is therefore highly recommended.

6.5.3 Comparison with other RNi_5

Muon spin relaxation experiments on ErNi_5 [88, 98, 99] and DyNi_5 [100] have revealed an unusual temperature dependence of the damping rate. ErNi_5 ($T_C = 9.2$ K) shows a strong c axis anisotropy and when the muon spin is perpendicular to the c axis the damping rate is too high below 60 K to be observed. With the muon spin polarization parallel to the c axis it is possible to observe the muon depolarization. The damping rate is constant above ~ 40 K. Below this temperature it increases and shows a maximum at 12 K. Below 12 K it decreases again until it reaches its minimum at ~ 5 K. The bump is remarkable because the spin fluctuations of the Er moments are anisotropic and along the c axis. Therefore no muon depolarization is expected. It is suggested by Kayzel [88] that quasi-static magnetic fluctuations are the origin of the broad bump in the damping rate.

DyNi_5 shows an easy plane magnetization and $T_C = 12.2$ K. μ^+ SR experiments with the muon polarization parallel to the c axis [100] probe the spin fluctuations of the Dy moments. When T_C is approached from above the damping rate increases strongly and reflects the critical slowing down of the Dy moments. Between 30 K and room temperature a bump in the damping rate is observed. The maximum is at about 80 K and, remarkably, also half of the asymmetry disappears below this temperature.

The possibility exists that, since the compounds are closely related in their crystallographic properties, the bumps described above are also related to muon dynamics. When the muon becomes trapped in a second site, the damping rate becomes enhanced. When the muon remains at this second site, the damping rate is reduced again. In the case of DyNi_5 the second site is for some reason not observed (damping rate possibly too high) and the corresponding asymmetry

disappears from the spectrum. Knight shift experiments on both compounds can verify this hypothesis.

Zero field μ^+ SR measurements on GdNi_5 [95] revealed a temperature independent damping rate above 50 K which is in large contrast with the results obtained on ErNi_5 and DyNi_5 . Therefore, if the unusual temperature dependence of the damping rate in ErNi_5 and DyNi_5 is related to a similar muon dynamics as observed in GdNi_5 , the magnetic anisotropy of the R magnetic moment is expected to play an important role.

In TbNi_5 [92] zero field μ SR spectra show that, below 60 K, two exponential damping functions are needed to analyse the spectra whereas above 60 K a single muon signal was sufficient. The authors mention the possibility of two muon sites as the origin of this phenomena. Since Tb and Gd are neighbours in the periodic table we believe this is indeed the case.

PrNi_5 is studied intensively [91] between 4 and 300 K by μ SR Knight shift measurements and the muon localizes at the $6i$ site in the whole temperature range. The lanthanide contraction is responsible for an a axis ratio between the two compounds of 0.988 and a c axis ratio of 0.996. This is a difference of less than one percent, but as far as the muon is concerned, there is apparently a distinct difference in electronic structure between PrNi_5 and GdNi_5 .

6.6 Conclusions

In this paper we have reported on the muon dynamics in GdNi_5 . Usually the muon becomes self trapped at an interstitial site and remains there during the μ^+ SR experiment. However, in GdNi_5 we observed clear signatures of the quantum behaviour of the muon.

The muon localizes at the $3f$ interstitial site and at room temperature the muon starts to diffuse between the different $3f$ sites in the crystal. Below ~ 80 K a second muon site becomes populated by muons. This is the $6m$ site and the muon occupies different $6m$ sites, which are located in a ring surrounding the $(0,0,\frac{1}{2})$ site, within the time scale of the μ^+ SR experiment (10^{-9} s).

During the time of the experiment we observed that the muon hops from the $6m$ site to the $3f$ site. There are no indications that the opposite process takes place. Therefore we conclude that the potential energy at the $6m$ site has a local minimum and the $3f$ site is still preferred by the muon. The hopping process from $6m$ to $3f$, which is characterized by half life time τ_0 , slows down when the temperature decreases. Signatures of muon hopping, either due to $6m \rightarrow 3f$ or $6m \rightarrow 6m$, are still observed in the magnetically ordered state down to 5 K.

Bibliography

- [1] K.N.R. Taylor and M.I. Darby, *Physics of Rare Earth Solids*, Chapman and Hall Ltd., London, 1972.
- [2] D. Craik, *Magnetism, principles and applications*, John Wiley & Sons, 1995.
- [3] C. Kittel, *Introduction to Solid State Physics*, John Wiley & Sons Inc., 1986.
- [4] R.P. Feynman, R.B. Leighton and M. Sands, *The Feynman lectures on Physics*, Addison-Wesley Publishing Company (1965) Vol.2, sect.34-7
- [5] W.S.C. Williams, *Nuclear and Particle Physics*, Clarendon Press, Oxford, 1992.
- [6] R.P. Feynman, *QED, The Strange Theory of Light and Matter*, Princeton University Press, 1985.
- [7] R.P. Feynman, R.B. Leighton and M. Sands, *The Feynman lectures on Physics*, Addison-Wesley Publishing Company (1965) Vol.3, sect.4-7
- [8] K.W.H. Stevens, *Proc. Phys. Soc. London A* 65 (1952) 209.
- [9] M.T. Hutchings, *Solid State Phys.* 16 (1964) 227.
- [10] H.P. Meyers, *Introductory to Solid State Physics*, Taylor & Francis, London, 1991.
- [11] D.A. Porter and K.E. Easterling, *Phase Transformations in Metals and Alloys*, Chapman & Hall, London, 1992.
- [12] R.L. Mössbauer, *Z. Physik* 151 (1958) 124.
- [13] R.L. Mössbauer, *Z. Naturforsch.* 14 (1959) 211.
- [14] G.K. Wertheim, *Mössbauer Effect: Principles and Applications*, Academic Press, New York, 1964.
- [15] P.C.M. Gubbens, A.A. Moolenaar, G.A. Stewart, F.M. Mulder and K.H.J. Buschow, *J. Magn. Magn. Mat.* 140-144 (1995) 1011.

- [16] Muons and Pions in Material Research, eds. J. Chappert and R.I. Grynspan, Elsevier Science Publishers, 1984.
- [17] R.L. Garwin, L.M. Lederman and M. Weinrich, *Phys. Rev.* 105 (1957) 1415.
- [18] A. Schenck, *Muon Spin Rotation Spectroscopy: Principles and Applications in Solid State Physics*, Adam Hilger Ltd, Bristol and Boston, 1985.
- [19] M. Alonso and E.J. Finn, *Fundamental University Physics, Volume III: Quantum and statistical physics*, ch. 9, Addison-Wesley Publishing company, 1968.
- [20] P. Dalmás de Réotier and A. Yaouanc, *J. Phys.: Cond. Mat.* 9 (1997) 9113.
- [21] S.W. Lovesey, *Theory of Neutron Scattering from Condensed Matter*, Vol.1, Clarendon Press, Oxford, 1984.
- [22] S.W. Lovesey, *Theory of Neutron Scattering from Condensed Matter*, Vol.2, Clarendon Press, Oxford, 1984.
- [23] G.E. Bacon, *Neutron diffraction*, Clarendon Press, Oxford, 1962.
- [24] O. Halpern and T. Holstein, *Phys. Rev.* 59 (1941) 960.
- [25] M. Th. Rekveldt, *Textures and Microstructures* 11 (1989) 127.
- [26] C.G. Shull, W.A. Strauser and E.O. Wollan, *Phys. Rev.* 83 (1951) 333.
- [27] D. Jiles, *Introduction to Magnetism and Magnetic Materials*, Chapman & Hall, London, 1991.
- [28] K.J. Strnat, in *Ferromagnetic Materials*, Vol.4, eds. E.P. Wohlfarth and K.H.J. Buschow, North-Holland Amsterdam 1988, p. 131.
- [29] J.A. Mydosh and G.J. Nieuwenhuys, in *Ferromagnetic Materials*, Vol. 1, eds. E.P. Wohlfarth and K.H.J. Buschow, North-Holland Amsterdam, ch. 2.
- [30] H. Oesterreicher, *J. Less. Comm. Met.* 25 (1971) 341.
- [31] H. Oesterreicher, *Phys. Stat. Sol.(a)* 40 (1977) K139.
- [32] P.C.M. Gubbens, J.H.F. van Apeldoorn, A.M. van der Kraan and K.H.J. Buschow, *J. Phys. F* 4 (1974) 921.
- [33] G. Petrich, *Z. Physik* 221 (1969) 431.
- [34] A. Blech and B.L. Averbach, in *Physics*, Vol. 1, No. 1 Pergamon Press, New York 1964, p. 31-44.
- [35] A.K. Grover, S.K. Malik, C. Radhakrishnamurty and R. Vijayaraghavan, *Solid State Comm.* 32 (1979) 1323.

- [36] K.H.J. Buschow, in *Ferromagnetic Materials*, Vol.1, eds. E.P. Wohlfarth and K.H.J. Buschow, North-Holland, Amsterdam 1980, ch.4.
- [37] P.C.M. Gubbens, A.M. van der Kraan and K.H.J. Buschow, *J. Magn. Magn. Mat.* 29 (1982) 155.
- [38] P.C.M. Gubbens, PhD thesis, Delft University of Technology, Delft, The Netherlands (1977).
- [39] H. Zijlstra, in *Ferromagnetic Materials*, Vol. 3, ed. E.P. Wohlfarth, North-Holland, Amsterdam 1982, ch. 2.
- [40] H. Eisaki, H. Takagi, R.J. Cava, B. Batlogg, J.J. Krajewski, W.F. Peck Jr., K. Mizuhashi, J.O. Lee and S. Uchida, *Phys. Rev. B* 50 (1994) 647.
- [41] J.W. Lynn, S. Skanthakumar, Q. Huang, S.K. Sinha, Z. Hossain, L.C. Gupta, R. Nagarajan and C. Godart, *Phys. Rev. B* 55 (1997) 6584.
- [42] R. Movshovich, M.F. Hundley, J.D. Thompson, P.C. Canfield, B.K. Cho and A.V. Chubukov, *Physica C* 227 (1994) 381.
- [43] B.K. Cho, Ming Xu, P.C. Canfield, L.L. Miller and D.C. Johnston, *Phys. Rev. B* 52 (1995) 3676.
- [44] L.J. Chang, C.V. Tomy, D. McK. Paul and C. Ritter, *Phys. Rev. B* 54 (1996) 9031.
- [45] L.P. Le, R.H. Heffner, G.J. Nieuwenhuys, P.C. Canfield, B.K. Cho, A. Amato, R. Feyerherm, F.N. Gyax, D.E. MacLaughlin and A. Schenck, *Physica B* 206&207 (1995) 552-554.
- [46] A.I. Goldman, C. Stassis, P.C. Canfield, J. Zarestky, P. Dervenagas, B.K. Cho, D.C. Johnston and B. Sternlieb, *Phys. Rev. B* 50 (1994) 9668.
- [47] P. Bonville, J.A. Hodges, C. Vaast, E. Alleno, C. Godart, L.C. Gupta, Z. Hossain, R. Nagarajan, G. Hilscher and H. Michor, *Z. Phys. B* 101, 511-520 (1996).
- [48] D.W. Cooke, J.L. Smith, S.J. Blundell, K.H. Chow, P.A. Pattenden, F.L. Pratt, S.F.J. Cox, S.R. Brown, A. Morrobel-Sosa, R.L. Lichti, L.C. Gupta, R. Nagarajan, Z. Hossain, C. Mazumdar and C. Godart, *Phys. Rev. B* 52 (1995) R3864.
- [49] A. Amato, P.C. Canfield, B.K. Cho, R. Feyerherm, F.N. Gyax, R.H. Heffner, L.P. Le, D.E. MacLaughlin, G.J. Nieuwenhuys and A. Schenck, unpublished.
- [50] B.J. Suh, F. Borsa, D.R. Torgeson, B.K. Cho, P.C. Canfield, D.C. Johnston, J.Y. Rhee and B.N. Harmon, *Phys. Rev. B* 53 (1996) R6022.

- [51] A.M. Mulders, P.C.M. Gubbens and K.H.J. Buschow, *Phys. Rev. B* 54 (1996) 14963.
- [52] U. Gasser, P. Allenspach, F. Fauth, W. Henggeler, J. Mesot, A. Furrer, S. Rosenkranz, P. Vorderwisch and M. Buchgeister, *Z. Phys. B* 101 (1996) 345-352.
- [53] R.J. Cava, H. Takagi, H. Eisaki, H.W. Zandbergen, T. Siegrist, B. Batlogg, J.J. Krajewski, W.F. Peck Jr., S. Carter, K. Mizuhashi, J.O. Lee, S. Uchida, R. Felder and R.B. van Dover, *Physica C* 235-240 (1994) 154.
- [54] B.K. Cho, P.C. Canfield, L.L. Miller, D.C. Johnston, W.P. Beyermann and A. Yatskar *Phys. Rev. B* 52 (1995) 3684.
- [55] F.M. Mulder, J.V.V.J. Brabers, R.C. Thiel, K.H.J. Buschow and F.R. de Boer, *Journ. of Alloys and Compounds* 217 (1995) 118.
- [56] C.V. Tomy, G. Balakrishnan and D.McK. Paul, *Physica C* 248 (1995) 349-352.
- [57] A. Amato, R. Feyerherm, F.N. Gygax and A. Schenck, *Hyp. Int.* 104 (1997) 115.
- [58] L.P. Le, R.H. Heffner, J.D. Thompson, D.E. MacLaughlin, G.J. Nieuwenhuys, A. Amato, R. Feyerherm, F.N. Gygax, A. Schenck, P.C. Canfield and B.K. Cho, *Phys. Rev. B* 53 (1996) R510.
- [59] B.K. Cho, P.C. Canfield and D.C. Johnston, *Phys. Rev. Lett.* 77 (1996) 163.
- [60] T. Shigeoka, N. Iwata, and H. Fujii, *J. Mag. Mag. Mat.* 104-107 (1992) 1229.
- [61] A. Blaise, B. Fåk, J.P. Sanchez, G. Amoretti, P. Santini, R. Caciuffo, D. Schmitt, B. Malaman, and G. Venturini, *J. Phys.: Condens. Matter* 7 (1995) 8317.
- [62] M. Slaski, A. Szytula, J. Leciejewicz, and A. Zygmunt, *J. Magn. Mag. Mat.* 46 (1984) 114.
- [63] P. Santini and G. Amoretti, *Phys. Rev. Lett.* 73 (1994) 1027.
- [64] C. Broholm, H. Lin, P.T. Matthews, T.E. Mason, W.J.L. Buyers, M.F. Collins, A.A. Menovsky, J.A. Mydosh and J.K. Kjems, *Phys. Rev. B* 43 (1991) 12809.
- [65] A.A. Moolenaar, P.C.M. Gubbens, and J.J. van Loef, *Nucl. Instr. and Meth. B* 94 (1994) 555.
- [66] I.A. Campbell, *J. Phys. F* 2 (1972) L47.
- [67] F. Baudalet, PhD thesis, (1991) Paris-Orsay University, unpublished.

- [68] A. Yaouanc, P. Dalmas de Réotier, P.C.M. Gubbens, A.A. Moolenaar, A.A. Menovsky, and C.E. Snel, *Hyp. Int.* 85 (1994) 351.
- [69] P. Wolfers, *J. Appl. Cryst.* 23(1990) 554.
- [70] L. Koester, H. Rauch, and E. Seymann, *Atomic Data and Nuclear Data Tables* 49 (1991) 65.
- [71] A.J. Freeman, and J.P. Desclaux, *J. Mag. Mag. Mat.* 12 (1979) 11.
- [72] A. March, *Z. Kristallogr.* 81 (1932) 285.
- [73] and a preliminary INS experiment performed at the reactor of the Interfaculty Reactor Institute (Delft).
- [74] M.T. Hutchings, *Solid State Phys.* 16 (1964) 227.
- [75] G.T. Trammell, *Phys. Rev* 31, 3625 (1963).
- [76] B. Bleaney, *Proc. Roy. Soc. (London)* 276 A (1963) 19.
- [77] J. Jensen, and A.R. MacKintosh, *Rare Earth Magnetism, Structures and Excitations*, Clarendon Press, Oxford 1991.
- [78] see for example, E. Bucher, C.W. Chu, J.P. Maita, K. Andres, A.S. Cooper, E. Buehler, and K. Nassau, *Phys. Rev. Lett.* 22 (1969) 1260.
- [79] W.L. Wang, and B.R. Cooper, *Phys. Rev.* 172 (1968) 539.
- [80] W.L. Wang, and B.R. Cooper, *Phys. Rev.* 185 (1969) 696.
- [81] D.A. Pink, *J. Phys. C1* (1968) 1246.
- [82] B.R. Cooper, and O. Vogt, *J. Phys. C1* (1971) 958.
- [83] B. Chevalier, J. Etourneau, P. Hagenmuller, S. Quezel and J. Rossat-Mignod, *J. Less Common Metals.* 111 (1985) 161.
- [84] D. Gignoux, and D. Schmitt, *Phys. Rev. B* 48 (1993) 12682.
- [85] Z. Zolnierak, and J. Mulak, *J. Mag. Mag. Mat.* 140-144 (1995) 1393.
- [86] G.J. Nieuwenhuys, *Phys. Rev. B* 35 (1987) 5260.
- [87] A.E. Sikkema, W.J.L. Buyers, I. Affleck, and J. Gan, *Phys. Rev. B* 54 (1996) 9322.
- [88] F.E. Kayzel, 'Magnetic and thermodynamic properties of RNi_5 compounds', Thesis, University of Amsterdam (1996) p90-96 and references therein.
- [89] A. Yaouanc, P. Dalmas de Réotier, P.C.M. Gubbens, A.M. Mulders, F.E. Kayzel and J.J.M. Franse, *Phys. Rev. B* 53 (1996) 350.

- [90] A. Yaouanc and P. Dalmas de Réotier, *J. Phys.: Cond. Mat.* 3 (1991) 6195.
- [91] R. Feyerherm, A. Amato, A. Grayevsky, F.N. Gygax, N. Kaplan and A. Schenck, *Z. Phys. B* 99 (1995) 3.
- [92] P. Dalmas de Réotier, J.P. Sanchez, A. Yaouanc, S.W. Harris, O. Hartmann, E. Karlsson, R Wäppling, D. Gignoux, B. Gorges, D. Schmitt, Ph. L'Héritier, A. Weidinger and P.C.M. Gubbens, *Hyp. Int.* 64 (1990) 389.
- [93] A. Percheron-Guégan, C. Lartigue, J.C. Achard, P. Germin, and F. Tasset, *J. Less. Com. Met.* 74 (1980) 1.
- [94] T.H. Jacobs, PhD thesis, Leiden University, Leiden, The Netherlands (1992).
- [95] A. Yaouanc, P. Dalmas de Réotier, P.C.M. Gubbens, F. Kayzel, P. Bonville, J.J.M. Franse and A.M. Mulders, *Journ. Mag. Mat.* 140-144 (1995) 1949.
- [96] A. Möslang, H. Graf, G. Balzer, E. Recknagel, A. Weidinger, Th. Wichert and R.I. Grynszpan, *Phys. Rev. B* 27, (1983) 2674.
- [97] H. Katayama, K. Terakura and J. Kanamori, *Solid State Comm.* 29 (1979) 431.
- [98] P.C.M. Gubbens, P. Dalmas de Réotier, J.P. Sanchez, A. Yaouanc, C.E. Snel, R. Verhoef, F. Kayzel, J. Song-Quan and J.J.M. Franse, *Journ. Mag. Mat.* 104-107 (1992) 1269.
- [99] P.C.M. Gubbens, A.A. Moolenaar, P. Dalmas de Réotier, A. Yaouanc, F. Kayzel, J.J.M. Franse, K. Prokes, C.E. Snel, P. Bonville, J.A. Hodges, P. Imbert and P. Pari, *Hyp. Int.* 85 (1994) 239.
- [100] P.C.M. Gubbens, private comm. and Proceedings of XXVIII Zakopane School of Physics, July 1993, ed. E.A. Görlich and K. Tomala, p. 163-180.

Summary

Four different rare earth intermetallics, TmFeAl , $\text{TmNi}_2\text{B}_2\text{C}$, PrRu_2Si_2 and GdNi_5 , are the subject of this thesis. Each of these compounds show interesting and new magnetic phenomena of which the peculiarities are summarized below. In general, rare earth intermetallics are of scientific interest because not only do they make excellent permanent magnets, but they also realize model systems of which the macroscopic properties, such as magnetism or superconductivity, are conveniently studied in relation to their local electronic structure. Large diversities in material properties are realized by element substitution and the influence of the individual elements gives insight in how to manufacture materials with specific properties of interest.

TmFeAl is a unique material in the sense that it shows a magnetic domain structure with very small dimensions in the order of nanometres. This type of behaviour has never been observed before and is the result of the strong magnetocrystalline anisotropy of the Tm magnetic moment combined with the structural disorder of the Fe magnetic moments in the lattice. This disorder creates a distribution of magnetic ordering temperatures which causes local formation of magnetic islands in a non magnetic matrix. The magnetic anisotropy of the Tm magnetic moment aligns these clusters along either the positive or negative c axis and after the magnetization is realized the moments are unable to rotate from their initial orientation. As a result up and down clusters coexist in the magnetically ordered state.

TmNi₂B₂C is one of the recently discovered rare earth boron carbides. Some of these compounds show magnetic order combined with superconductivity and since magnetic moments cause electronic Cooper pair breaking and the two phenomena expel each other, the borocarbides have been intensively studied since their discovery in 1993. As the superconducting transition temperature as well as the magnetic ordering temperature vary throughout the rare earth-borocarbide series, the interplay between the two phenomena can be studied.

In this thesis one particular borocarbide is studied, $\text{TmNi}_2\text{B}_2\text{C}$. Unique in its magnetic anisotropy in this series, the Tm magnetic moment shows a preferential c axis alignment. Two samples were studied by ^{169}Tm Mössbauer spectroscopy and two sizes in magnetic Tm moment appear to exist in $\text{TmNi}_2\text{B}_2\text{C}$ of which the ratio depends on the specific preparation conditions of the sample. A relation between

the size of the Tm magnetic moment and the amount of carbon interstitials in the lattice is suggested. This idea provides a possible explanation for the discrepancy in magnetic Tm moments observed by other research groups. If a carbon atom is missing in the lattice and a vacancy is present, the modified local electronic structure reduces the magnetic Tm moment. Small amounts of carbon vacancies are easily disregarded by macroscopic techniques but a local interstitial probe such as the muon possibly localizes in the carbon vacancies and observes in this case only the reduced Tm moment.

PrRu₂Si₂ is a ferromagnet with a giant magnetic anisotropy. In fact, it shows the largest anisotropy observed in this class of materials. In this thesis this large anisotropy is conveniently explained in terms of crystal field interactions, i.e. the interaction of the magnetic Pr 4*f* electron shell with the electronic charge in the crystal lattice. Its large magnetic moment of 2.8 μ_B is induced in the singlet ground state of the 4*f* electrons and is enhanced due to dispersion of this ground state. An attempt is made to describe this dispersion in the random phase approximation. This results in a better description of the experimental data compared with molecular field theory.

GdNi₅ is a ferrimagnet which has been studied intensively. Its magnetic behaviour is well understood. This has resulted in a description of this magnet in terms of Muon Spin Relaxation experiments. For a detailed analysis of these data the interstitial location site of the muon inside the material is of importance. In an attempt to obtain experimental information about this location, some interesting muon dynamics are discovered.

In the temperature region between ~80 and 300 K the muon localizes at a single muon site and above room temperature the muon has enough kinetic energy to diffuse from site to site. This is believed to be the general behaviour of muons in (inter)metallics: at low temperature they are localized at a certain interstitial site (sometimes at two sites) and at elevated temperatures the muons diffuse through the lattice. In GdNi₅, the population of a second muon site becomes visible below 80 K. Moreover, muons which localize at this second site occupy a ring of six equivalent sites within the time scale of the experiment, 10^{-9} s, i.e. they hop from site to site. From this metastable second site the muons move to the first muon site. The dynamics of this muon hopping is visible in the μ^+ SR spectra and the consequences for the interpretation of the Muon Spin Relaxation data are discussed.

* * *

Samenvatting

Een viertal intermetallische verbindingen met zeldzame aardmetalen, TmFeAl , $\text{TmNi}_2\text{B}_2\text{C}$, PrRu_2Si_2 en GdNi_5 zijn het onderwerp van dit proefschrift. Elke verbinding vertoont nieuwe en interessante eigenschappen die hieronder samengevat zijn. In het algemeen zijn intermetallische zeldzame aard verbindingen van wetenschappelijk belang omdat zij zowel de basis vormen van uitstekende permanente magneten, als ideale model systemen zijn. De macroscopische eigenschappen, zoals magnetisme en supergeleiding, worden bestudeerd in relatie tot hun elektronenstructuur. Er kan een grote verscheidenheid in materiaaleigenschappen gerealiseerd worden door het toepassen van elementsubstitutie en de invloed van de individuele elementen maakt duidelijk hoe materialen met specifieke eigenschappen gefabriceerd kunnen worden.

TmFeAl is een uniek materiaal omdat het een magnetische domein structuur vertoont op nanometer schaal. Dit type domeinstructuur is nooit eerder waargenomen en wordt veroorzaakt door de sterke magnetische anisotropie van het Tm subrooster en door de structurele wanorde van de ijzeratomen in het kristalrooster. Deze wanorde veroorzaakt een distributie in de magnetische ordening temperatuur en dit resulteert in het ontstaan van magnetische eilanden in een paramagnetische omgeving. De hoge anisotropie van het Tm zorgt ervoor dat de magnetisatie in deze clusters parallel of anti-parallel aan de c -as is en dat de magnetische momenten zich niet meer kunnen heroriënteren. Hierdoor ontstaan clusters met de magnetisatie langs de positieve of negatieve c -as die slechts nanometers groot zijn.

$\text{TmNi}_2\text{B}_2\text{C}$ is een verbinding uit de recentelijk ontdekte klasse van zeldzame-aard-boriumcarbides. Enkele van deze verbindingen vertonen coëxistentie van magnetische ordering en supergeleiding. De magnetische momenten trachten de supergeleidende Cooper paren te verbreken door hun exchange interactie met de spins van de Cooper elektronen. Vanwege deze competitie worden deze boriumcarbide verbindingen intensief bestudeerd sinds hun ontdekking in 1993. De sterkte van de magnetische interactie tussen de zeldzame aard atomen is afhankelijk van het type atoom en op deze manier kan de interactie tussen magnetisme en supergeleiding in deze klasse van verbindingen bestudeerd worden.

Tijdens dit onderzoek is één specifieke verbinding bestudeerd, $\text{TmNi}_2\text{B}_2\text{C}$. Als enige in deze klasse van verbindingen vertoont het Tm moment een c -as oriëntatie.

Twee preparaten zijn bestudeerd met ^{169}Tm Mössbauer spectroscopie; met deze techniek zijn twee verschillende groottes in Tm moment aangetoond (0.1 en 4.3 μ_B). De verhouding tussen beide fracties hangt sterk af van de manier waarop het preparaat vervaardigd is en daarom wordt verondersteld dat de hoeveelheid interstitieel koolstof in het kristalrooster van cruciaal belang is in deze verbinding. Ieder Tm atoom hoort in deze verbinding omringd te worden door vier koolstof atomen. Als op een bepaalde positie een koolstof atoom ontbreekt dan verandert lokaal de ladingsverdeling in het kristal, het zogeheten kristalveld. Hierdoor kan de voorkeursoriëntatie van de 4f elektronen schil van het Tm atoom veranderen en daarmee ook de grootte van het magnetische 4f moment. Kleine hoeveelheden koolstof vacatures worden makkelijk over het hoofd gezien door macroscopische technieken maar een locale probe, zoals $\mu^+\text{SR}$, is er erg gevoelig voor. Het muon ziet de vacatures als een ideale rustplaats en hierdoor wordt alleen het, door koolstof vacatures gereduceerde Tm moment, waargenomen.

PrRu_2Si_2 is een ferromagnetische verbinding met een sterke magnetische anisotropie, de hoogste ooit waargenomen in deze klasse van verbindingen. Dit gedrag is in dit proefschrift verklaard door de interactie van de 4f elektronen van het Pr atoom met het kristalveld. Het relatief grote magnetische Pr moment van 2.8 μ_B is in de singlet grondtoestand van de 4f elektronen schil geïnduceerd en wordt versterkt door dispersie van deze grondtoestand. Deze dispersie is beschreven in de 'random phase' benadering en dit resulteert in een betere beschrijving van de experimentele gegevens in vergelijking tot de moleculaire veld theorie.

GdNi_5 is een ferrimagnetische verbinding die de afgelopen jaren intensief bestudeerd is en waarvan de magnetische eigenschappen goed gekarakteriseerd zijn. Dit heeft geleid tot een modelbeschrijving van $\mu^+\text{SR}$ experimenten aan deze verbinding. Voor een gedetailleerde analyse is de plaats waar het muon localiseerd in het kristalrooster van essentieel belang. Tijdens het bepalen van de muon plaats in GdNi_5 is een nieuwe muodynamica ontdekt. Tussen 80 en 300 K localiseert het muon op een enkele interstitiële plaats in het kristalrooster en boven 300 K diffundeert het muon van plaats tot plaats. Dit is in het algemeen het gedrag van muonen in intermetallische verbindingen: bij lage temperatuur localiseert het muon op een bepaalde plaats (soms op meerdere plaatsen) en bij hogere temperatuur diffundeert het muon door het kristal. Maar in GdNi_5 zien we dat muonen een tweede plaats bezetten beneden 80 K. Bovendien bezet het muon zes zulke plaatsen, die een ring vormen rond de $(0,0,\frac{1}{2})$ plaats, binnen de tijdschaal van het muon experiment, 10^{-9} s, d.w.z. de muonen springen van plaats naar plaats. Deze tweede plaats is metastabiel en daarom springen de muonen die hier localiseren door naar de eerst genoemde locatie. Dit springen is zichtbaar in de $\mu^+\text{SR}$ spectra en de consequenties voor de interpretatie van de muon spectra zijn beschreven in hoofdstuk 6.

Dankwoord & Thanks

Dit proefschrift had nooit in zijn huidige vorm tot stand kunnen komen zonder de hulp en bijdragen van vele personen. Deze wil ik hierbij dan ook, in willekeurige volgorde, hartelijk bedanken.

Paul, bedankt voor het vertrouwen dat je in me hebt gesteld, de vrijheid die je me gaf om mijn eigen onderzoekslijn uit te zetten en de regelmatige schouderklopjes. Verder zijn je experimentele hulp en je wetenschappelijke archief, dat voornamelijk in je hoofd zit, van onschatbare waarde geweest.

Pa en Ma, bedankt omdat jullie me het vertrouwen hebben meegegeven dat als ik iets wil, ik het ook kan en Pa, bedankt voor figuur 1.4.

Jeroen van de Kamer en ook Robbert Jan Westerduijn, bedankt voor de filosofisch, natuurkundige discussies die we hadden tijdens onze natuurkunde studie, deze discussies hebben mij mede geïnteresseerd gemaakt in het wetenschappelijk onderzoek.

Alle collega's die bijgedragen hebben tot de prettige werksfeer op het IRI en specifiek de mensen van de IRI-bar, bedankt voor jullie gezelligheid.

Jurgen, bedankt voor de sample preparatie en je hulp bij het leggen van contacten en het uitzetten van de onderzoekslijn en, ook Adri en Paul, bedankt voor het kritisch lezen van mijn manuscripten.

Henk, Hans en Leo van Oss, bedankt voor jullie hulp bij experimentele problemen en het vervoer van (gesleep met) He-vaten.

Michel en André, behalve het losdraaien van schroeven die jullie veel te vast hadden vastgedraaid om door mij te worden losgedraaid, ook bedankt voor jullie hulp bij het oplossen van de vele experimentele problemen.

Marian, bedankt voor je hulp bij administratieve taken, en Nel en Rob, bedankt voor het regelen van de vele reisdeclaraties.

Marc Brinkman, bedankt voor het ontwerpen van de kaft van dit proefschrift; deze driedimensionale tekening geeft de inhoud mooi weer.

Ekkes Brück, bedankt voor de samenwerking en de magnetisatie metingen aan $RFeAl$ in Amsterdam; zij zijn terug te vinden in figuur 3.9.

Wicher Kraan en Theo Rekvelde, bedankt voor de hulp bij de neutronen depolarisatie metingen aan $TmFeAl$ en $ErFeAl$. Deze zijn van essentieel belang bij de interpretatie van het gedrag van deze verbindingen.

Alle leden van de 'Heavy Fermion club' in Leiden en speciaal Gé Nieuwenhuys, bedankt voor de inspirerende wetenschappelijke discussies en de samenwerking aan

TmNi₂B₂C. Bernd Becker, jou soortelijke warmte metingen zijn onmisbaar bij een gedegen presentatie van mijn C vacature idee, dank je wel!

Bert Moleman, bedankt voor de röntgendiffractie metingen aan GdNi₅; je kunt ze terug vinden in figuur 6.10.

Roger Thiel en Bart van der Straat, bedankt de hulp bij ⁵⁷Fe Mössbauer metingen in jullie cryostaat met een magneet veld op het sample.

Hans Tichelaar, bedankt voor het maken van, en het discussieren over, elektronen transmissie foto's van TmFeAl en ErFeAl. Manfred van der Vlies, bedankt voor de karakterisatie van RFeAl met neutronen activerings analyse. Beide resultaten zijn beschreven in hoofdstuk 3.

En tot slot in het nederlands, Andrew, bedankt voor je engelse steun, het lol maken en je relativerend optimisme!

During my time at the IRI, I had the opportunity to visit scientific institutes in France, Switzerland, England and Germany. These visits were stimulating and prominent and I would like to thank the following scientists.

Alain Yaouanc and Pierre Dalmas de Réotier, thanks for scientific cooperation, the muon science you taught me and the nice scientific discussions we had. And also Frank Kayzel, Karl Prokes, Andrew Huxley and Carlo, thanks for the company during the long nights we performed μ SR measurements at ISIS and PSI.

Steven Cottrel, Sue Kilkoyn, Christopher Scott and Philip King, thanks for the help with the EMU and MuSR instrumentation at ISIS. To our surprise, we discovered a second magnetic phase transition (figuur 5.5).

Pierre Bonville, thanks for the scientific discussions and cooperation at ISIS, PSI and at your institute in Saclay.

Alex Schenk, thanks for the fruitful discussion about chapter 6 and also Alex Amato, Fred Gygax, Ralf Feyerherm and Markus Pinkpank, thanks for the help with the muon Knight Shift measurements we performed at PSI.

Chris Baines, thanks for performing the μ SR measurement on TmNi₂B₂C, it made sceptic scientists believe in the C vacancies model.

Norbert Stüßer and Michael Hofmann, thanks for performing neutron diffraction experiments on ErFeAl and more thanks for your help with neutron diffraction on TmFeAl.

Urs Gasser, thanks for our productive cooperation on the TmNi₂B₂C_z compounds. The measurements we performed on your sample gave a nice insight in the material!

To conclude this list of many thanks, thanks to all people who believe that PHYSICS IS FUN!

Curriculum Vitae

Annemieke Mulders werd geboren op 13 augustus 1970 te Maasland. Daar bezocht zij de kleuterschool en daarna de basisschool. Van 1982 tot 1988 doorliep zij het VWO op de Scholengemeenschap Westland-Zuid te Vlaardingen. Vervolgens ging zij naar Delft.

Na een jaar de studie Industrieel Ontwerpen te hebben gevolgd aan de TU veranderde zij van studierichting en ging natuurkunde studeren aan de TH Rijswijk. Hier behaalde zij met cum laude haar diploma in 1993. Gedurende vijf maanden studeerde zij vervolgens natuurkunde aan de RU Groningen. Vanaf februari 1994 was zij werkzaam als AIO bij het IRI. Een groot deel van het werk uit deze periode is beschreven in dit proefschrift. Vanaf mei 1998 is zij werkzaam bij ASM Lithography te Veldhoven.

List of publications

A. Yaouanc, P. Dalmas de Réotier, P.C.M. Gubbens, F. Kayzel, P. Bonville, J.J.M. Franse and A.M. Mulders, *Muon spin relaxation in uniaxial ferromagnets*, J. Magn. Magn. Mat. 140-144 (1995) 1949.

A.M. Mulders, P.C.M. Gubbens, Q.A. Li, F.R. de Boer and K.H.J. Buschow, *Investigation of the magnetic properties and ^{57}Fe Mössbauer effect in DyFe_4Ge_2* , J. of All. Comp. 221 (1995) 197.

P. Dalmas de Réotier, A. Huxley, A. Yaouanc, J. Flouquet, P. Bonville, P. Imbert, P. Pari, P.C.M. Gubbens and A.M. Mulders, *Absence of zero field muon spin relaxation induced by superconductivity in the B phase of UPt_3* , Phys. Lett. A 205 (1995) 239.

A. Yaouanc, P. Dalmas de Réotier, P.C.M. Gubbens, A.M. Mulders, F. Kayzel and J.J.M. Franse, *Muon-spin-relaxation study of the critical longitudinal spin dynamics in a dipolar Heisenberg ferromagnet*, Phys. Rev. B 53 (1996) 350.

A.M. Mulders, W.H. Kraan, A.R. Ball, E. Brück, K.H.J. Buschow and P.C.M. Gubbens, *Unique magnetic behaviour of TmFeAl*, Hyp. Int. 97/98 (1996) 109.

A.M. Mulders, P.C.M. Gubbens and K.H.J. Buschow, *A ^{169}Tm Mössbauer spectroscopy study of the magnetic superconductor $\text{TmNi}_2\text{B}_2\text{C}$* , Phys. Rev. B 54 (1996) 14963.

P. Bonville, P. Dalmas de Réotier, A. Yaouanc, G. Polatsek, P.C.M. Gubbens and A.M. Mulders, *The effect of the crystal electric field on the Kondo-type fluctuations in YbAuCu_4* , J. Phys: Cond. Mat. 8 (1996) 755.

A.D. Huxley, P. Dalmas de Réotier, A. Yaouanc, D. Caplan, M. Couach, P. Lejay, P.C.M. Gubbens and A.M. Mulders, *CeRu_2 : A magnetic superconductor with extremely small magnetic moments*, Phys. Rev. B 54 (1996) R9666.

P. Dalmas de Réotier, A. Yaouanc, R. Calemczuk, A.D. Huxley, C. Marcenat, P. Bonville, P. Lejay, P.C.M. Gubbens and A.M. Mulders, *CePt_2Si_2 : A Kondo lattice compound with no magnetic ordering down to 0.06 K*, Phys. Rev. B 55 (1997) 2737.

A. Yaouanc, P. Dalmas de Réotier, A.D. Huxley, P. Bonville, P.C.M. Gubbens, A.M. Mulders, P. Lejay and S. Kunii, *$\mu^+\text{SR}$ characterization of weak moment magnets*, Physica B 230-232 (1997) 269.

A.M. Mulders, A. Yaouanc, P. Dalmas de Réotier, P.C.M. Gubbens, A.A. Moolenaar, B. Fåk, E. Ressouche, K. Prokeš, A.A. Menovsky and K.H.J. Buschow, *PrRu_2Si_2 : A giant anisotropic induced magnet with a singlet crystal-field ground state*, Phys. Rev. B 56 (1997) 8752.

A.M. Mulders, P.C.M. Gubbens, U. Gasser, C. Baines and K.H.J. Buschow, *Two magnetic moments observed at the Tm site in the magnetic superconductor $\text{TmNi}_2\text{B}_2\text{C}$* , J. Magn. Magn. Mat. 177-181 (1998) 555.

A.M. Mulders, P.C.M. Gubbens, U. Gasser, C. Baines and K.H.J. Buschow, *Two types of magnetism in the magnetic superconductor $\text{TmNi}_2\text{B}_2\text{C}$ related to the degree of carbon site occupancy*, Phys. Rev. B. 57 (1998) 10320.

P.C.M. Gubbens and A.M. Mulders, *Magnetic behaviour of systems with a quasi-doublet ground state*, Australian Journ. of Phys., accepted for publication.

Index

- RNi_2B_2C , 48, 49
- 4*f* electron clouds, 10
- Boron carbides, 48
- Bragg's law, 24
- Carbon interstitials, 57
- Carbon vacancy, 57, 59
- CFP, 10
- $Co_{60}Ga_{40}$, 42
- Crystal field, 16
- Crystal field hamiltonian, 9
 - hexagonal, 29
 - tetragonal, 50, 71
- Crystal field level scheme, 73
- Crystal field parameters, 10
- Crystal field theory, 9
- Crystal structure
 - hexagonal, 91
 - hexagonal Laves phase, 29
 - tetragonal, 49
- Curie constant, 7
- Curie law, 7
- Curie temperature, 7
- Damping rate, 21
 - $GdNi_5$, 83, 94
 - $PrRu_2Si_2$, 66
- De Gennes scaling, 36, 48
- Dipolar field, 8, 82
- $DyNi_5$, 100
- Electric field gradient, 16, 17
- Entropy, 11, 26
 - $PrRu_2Si_2$, 62
- $ErNi_5$, 100
- Exchange interaction, 7, 48, 72
- Fermi contact interaction, 81, 82
- Gibbs free energy, 11
- Grüneisenfunction, 92
- Heisenberg exchange interaction, 7
- High field magnetization, 37, 64
- Hund's rules, 5, 62
- Hyperfine splitting, 17
- Isomer shift, 15
- Itinerant magnetism, 5, 28
- Jahn-Teller effect, 11
- Kramers theorem, 11
- $LaNi_5D_x$, 92, 99
- Lanthanide contraction, 4
- Lorentz sphere, 82
- Mössbauer
 - ^{141}Pr spectra, 65
 - ^{169}Tm spectra
 - $TmFeAl$, 31
 - $TmNi_2B_2C$, 52, 55, 56
 - ^{57}Fe spectra, 33, 35
 - spectroscopy, 14
- Magnetic anisotropy, 1, 4, 11, 25, 34,
62, 64
 - constant, 11
 - energy, 11
- Magnetic nanodomains, 44–46
- Magnetic phase transition, 11
 - first order, 11, 61, 68, 75
 - second order, 12
- Magnetic structures, 8, 24, 48, 61

- Magnetic susceptibility, 7
- March formula, 66
- Moiré pattern, 30
- Molecular field, 12, 29, 73
- Muon
 - decay, 20
 - depolarization, 21, 81
 - diffusion, 85, 96
 - hopping, 93, 95
 - precession frequency, 21
 - production, 20
 - properties, 18
 - self trapping, 95
 - tunneling, 96
- Muon Knight shift, 81
- Muon spectroscopy, 18, 19
- Muon spin relaxation, 21, 65
- Muon spin rotation, 19
 - GdNi₅, 80
 - TmNi₂B₂C, 57
- Néel temperature, 7
- Neutron scattering, 22
 - depolarization, 22, 39
 - ErFeAl, 40
 - TmFeAl, 40
 - diffraction, 24, 41
 - ErFeAl, 43
 - PrRu₂Si₂, 66, 67
 - TmFeAl, 42
 - elastic, 24
 - inelastic, 23, 68–70
 - magnetic, 23
- Ni (metallic), 100
- Orbital momentum, 5
 - quenched, 25
- Partition function, 26
- Pauli principle, 7
- Permanent magnets, 1, 4
- Point group, 71
- PrNi₅, 85, 99, 101
- Quadrupole moment, 15, 16
- Quadrupole splitting, 15
- Quantum Electro Dynamics, 5
- Raman scattering, 81
- Random Phase Approximation, 75
- Recoilless fraction, 14
- RKKY interaction, 8
- Russel-Saunders coupling, 5, 25
- Schottky anomaly, 26
 - PrRu₂Si₂, 72
 - TmNi₂B₂C, 59
- Space group, 10
- Specific heat, 25
 - PrRu₂Si₂, 62
 - TmNi₂B₂C, 51
- Spin, 5
- Spin glass, 28, 42
- Spin orbit interaction, 5
- Superconductivity, 48, 54
- TbNi₅, 101
- Zeeman interaction, 25, 71